STRUCTURAL STUDIES OF FUSION PEPTIDE FROM TICK-BORNE ENCEPHALITIS VIRUS AND NANOCRYSTALLINE CELLULOSE FILMS

by

JINHE PAN

B.Sc., Peking University, 2003

A THESIS SUBMITTED IN PARTIAL FULFILLMENT OF THE REQUIREMENTS FOR THE DEGREE OF

DOCTOR OF PHILOSOPHY

in

THE FACULTY OF GRADUATE STUDIES

(Chemistry)

THE UNIVERSITY OF BRITISH COLUMBIA

(Vancouver)

October 2009

Abstract

This thesis describes structural studies on two different systems, namely the fusion peptide (FP) from the tick-borne encephalitis virus (TBEV) and nanocrystalline cellulose (NCC). The first is a small biopolymer composed of 16 amino acid residues, which binds to the target cell membrane and plays a critical role in membrane fusion. The second is a biopolymer composed of a large number of glucose subunits, which has attracted recent interest with regards to the development of new materials.

In this thesis, I have established synthetic access to the model FP fragment from TBEV. To our knowledge, the studies in this thesis are the first investigation on the individual Class II FP. The synthetic peptide can induce membrane fusion at acidic pH. Mutational studies showed that replacement of Leu 107 with Thr strongly impaired fusogenic activity, whereas a Phe mutant still retained a significant degree of activity. These results were consistent with activity found in mutant TBE viruses, indicating that the synthetic TBEV FP obtained here can serve as a model fusion system.

Previous literature studies have shown that a disulfide bond stabilizes the peptide fold and the full length fusion protein functions as a trimer. I therefore tested the hypothesis that these are also necessary conditions for the FP. The studies on the modified FPs suggest that the lipid-binding portion in the synthetic peptides adopts a

similar conformation. However, the disulfide bond promotes β-strand formation in the peptide. Finally, the formation of an artificial trimer enhances the fusogenic activity.

In the second part of this thesis, the chiral nematic structure and crystallinity of the NCC films were investigated. The chiral nematic pitch of the NCC films was affected by all of the parameters listed here, namely the hydrolysis conditions, ionic strength, suspension concentration, drying temperature and magnetic field. The crystallinity of the NCC films was influenced by the drying temperature, ionic strength and magnetic field were small. These results suggest that these sample conditions affect the chiral nematic structure and the crystallinity of the NCC films, a finding which will be important in the development of novel cellulosic materials.

Table of Contents

List of Tables

List of Figures

List of Abbreviations

Boc	butoxycarbonyl
CD	circular dichroism
Chol	cholesterol
CODEX	centerband-only detection of exchange
CP/MAS	cross-polarization magic-angle spinning
CPL	circularly polarized light
CSA	chemical shift anisotropy
DCM	dichloromethane
DIEA	*N*,*N*-diiopropylethylamine
DMF	*N*,*N*-Dimethylformamide
DTNB	5, 5'-dithiobis (2-nitrobenzoate)
DTT	dithiothreitol
EDT	ethane dithiol
EPR	electron paramagnetic resonane
Fmoc	9H-fluoren-9-ylmethoxycarbonyl
FP	fusion peptide
FRET	fluorescence resonance energy transfer
FTIR	fourier transform infrared spectroscopy
HA	hemagglutinin
HBTU	2-(1*H*-benzotriazol-1-yl)-1,1,3,3-tetramethyluronium hexafluorophosphate
HEPES	4-(2-hydroxyethyl)-1-piperazineethanesulfonic acid
HIV	human immunodeficiency virus
HOBT	*N*-Hydroxybenzotriazole
HPLC	high-performance liquid chromatography
ICD	induced circular dichroism
LUV	large unilamellar vesicle
MALDI	matrix-assisted laser desorption/ionization
Mtt	4-methyltrityl
NBD-PE	*N*-(7-nitro-2,1,3-benzoxadiazol-4-yl)phosphatidylethanolamine
NCC	nanocrystalline cellulose
NMR	nuclear magnetic resonance
NOESY	nuclear Overhauser enhancement spectroscopy
OtBu	tert-butyl ester
PE	phosphoethanolamine
PC	posphatidylcholine

Ph-PE	*N*-(lissamine Rhodamine B sulfonyl)phosphatidylethanolamine
Pmc	2,2,5,7,8-pentamethylchroman-6-sulfonyl
POPC	1-palmitoyl-2-oleoyl-*sn*-glycero-3-phosphocholine
POPE	1-palmitoyl-2-oleoyl-*sn*-glycero-3-phosphoethanolamine
RECOR	rotational-echo double-resonance
rf	radiofrequency
SFV	Semliki Forest virus
SIN	Sindbis virus
SPPS	solid-phase peptide synthesis
SSNMR	solid-state nuclear magnetic resonance
SUV	small unilamellar vesicle
TBEV	tick-borne encephalitis virus
tBu	tert-butyl
TES	triethylsilane
TFA	trifluoroacetic aicd
T_H	hexagonal phase transition temperature
TNB	2-nitro-5-thiobenzoate
TOCSY	total correlation spectroscopy
Trt	trityl

Acknowledgments

This thesis would never have been written without the generous help and support that I received from numerous people along the way. I would now like to take this opportunity to express my sincerest thanks to these individuals.

First and foremost, I would like to thank my supervisor, Dr. Suzana K. Straus. Suzana has always been kind, patient and supportive. She has provided me with guidance and an environment conducive to learning and quality research. I also thank Suzana for giving me important advice on my graduate studies. I believe I will benefit substantially as a result of her suggestions in the future.

I would be remiss if I did not thank Dr. Wadood Hamad. I spent the last year of my graduate studies under Wadood's co-supervision. During this time, Wadood was very supportive of my research. He has heightened my interests in cellulose and shared his extensive knowledge on NCC structure with me.

Next, I would like to express my gratitude to Dr. Colin A. Fyfe. I thank Colin for his invaluable advice on my research and thesis writing.

I am also grateful for all the help received from the current and past members of the Straus group. We have shared many unforgettable moments both in and outside of the lab. A special thank you goes to Erica Tiong, Anthony Lin, and Benjamin Lai for their initial work on the TBEV FP project. I would also like to acknowledge Yeang-Ling Pan and

John T.J. Cheng for our collaboration on the aurein peptide project.

I would like to express my gratitude to Dr. Siham Atifi for the help with NCC sample preparation and polarized microscopy. I would also like to thank Dr. John Sherman for the use of peptide synthesizer, Dr. Robert R.E. Hancock for the use of extruder, and all of the other service departments at UBC who have helped me along the way.

Finally, I would like to thank my family and friends, especially my parents for their unconditional love, support, and dedication to me. I thank my wife Di Xu for her love and encouragement.

Chapter 1: Introduction

1.0 Structural studies of the fusion peptide from TBEV and NCC

This thesis describes structural studies on two different systems, namely the fusion peptide (FP) from the tick-borne encephalitis virus (TBEV) and nanocrystalline cellulose (NCC). The first is a small biopolymer composed of 16 amino acid residues, while the second is a biopolymer composed of a large number of glucose subunits. Despite their different properties, which will be described in detail in subsequent sections, both biomolecules play important functional roles at the cellular level.

Infection of cells by enveloped viruses such as TBEV and dengue virus requires a step in which the viral membrane fuses with a cellular membrane. Fusion is mediated by envelope proteins in the viral membrane which contain a special segment, called 'the fusion peptide' (FP), as shown in Figure 1.1.a. The FPs interact with the target cell membrane and play a key role in membrane fusion[1]. Detailed information about FPs and membrane fusion will be presented in Section 1.3.

Cellulose, on the other hand, is a structural biopolymer. It is the primary structural component of plant cell walls (Figure 1.1.b). In the plant cell walls, the cellulose microfibrils are linked via hemicellulosic tethers to form a cellulose-hemicellulose

network, which is embedded in the pectin matrix. As the major element in plant cell walls, cellulose is considered to contribute to over half of the carbon in the biosphere[2].

Figure 1.1 (a) Molecular structure of dengue virus determined by electron microscopy[3]. The FPs are colored in light red. (b) Illustration showing a section of the cell wall in the plant cell[4].

(a)

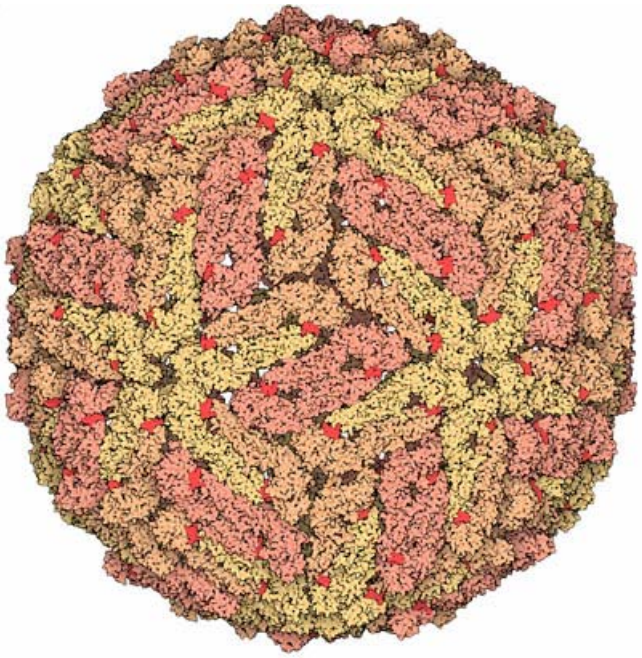

(b)

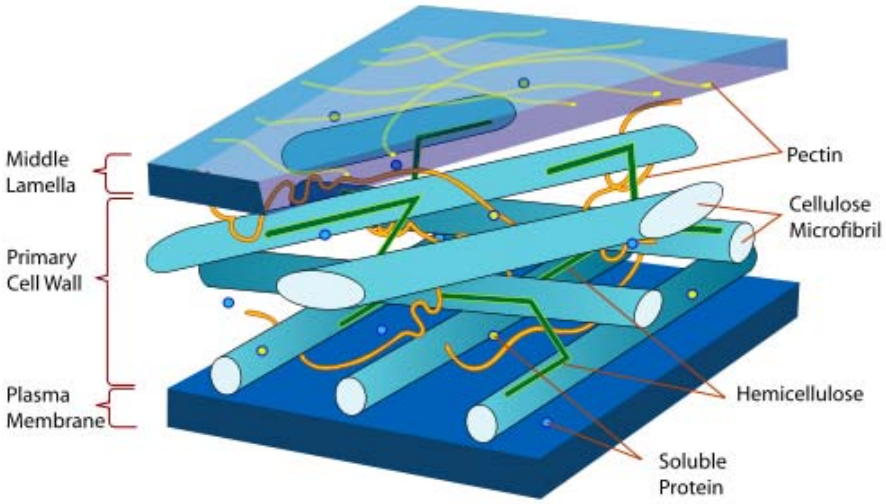

1.1 Structure-function studies

The unifying theme of this thesis is our aim to understand how both the FP of TBEV and NCC function. In order to understand the mechanism of the action of these biopolymers, it is important to understand their three-dimensional arrangement, in a biologically relevant environment.

1.1.1 Thesis goals

FPs play a central role in facilitating membrane fusion induced by fusion proteins of enveloped viruses such as TBEV. The FPs are highly conserved and quite hydrophobic. These peptides usually become exposed during a conformational change and are believed to be the only segment of the fusion protein to insert into the target membrane[5]. Therefore, the study of FPs could help us understand the mechanism of membrane fusion. This thesis will explore the function of the FP from TBEV, which is a segment of the full fusion membrane protein from TBEV, through the design, synthesis, and characterization of its fusogenic activity and structure. A challenge in this area of research is the ability to create native-like peptides. The design and characterization of a native-like peptide will be approached by first attempting to make and study the monomer of the FP of TBEV. Subsequently, the synthesis of the trimer of the FP of TBEV will be discussed. With the more active and native-like peptide trimers, the molecular mechanisms underlying FP

activity in the whole protein may be obtained.

The other goal which will be discussed in this thesis is the structural study of NCC films. Cellulose crystallites form ordered chiral nematic suspensions above a critical concentration[6]. By simply casting films from suspensions of cellulose crystallites, cellulose films can be prepared with specific optical properties which result from its chiral nematic structure[7]. The chiral nematic structure, whose pitch is on the order of the wavelength of visible light, reflects circularly polarized light of the same handedness[8]. By changing the chiral nematic pitch of the films, different colors of reflected light can be achieved. This technique can be used to produce optically variable films and ink pigments for security papers, as the optical properties cannot be reproduced by printing or photocopying[9]. In addition, the crystallinity of cellulose crystallites is thought to be a very important property which needs to be taken into account when considering the manufacturing and applications of cellulose and cellulosic materials, since cellulose crystallinity strongly influences the biophysical behavior of such a polymer. For instance, it directly affects the ease with which cellulose can be derivatized, as well as swelling and water-binding properties. To our knowledge, the question of whether there is a direct relationship between crystallinity and the structure of the chiral nematic phase has not been answered yet. Therefore, studying the structure of cellulose would help us not only optimize the production of novel materials, but also understand the correlation between the micro- and macrostructure of NCC.

1.1.2 Thesis overview

The following sections in Chapter 1 will introduce the methods of structural determination. Furthermore, it will present the interaction of FPs with membranes, give some examples of structural studies of FPs from other viruses in model systems, and present the proposed fusion mechanism of the envelope protein E of TBEV, based on literature reports of X-ray crystallographic and other biophysical data. In addition, the basics of cellulose structure will be introduced in this chapter. Chapter 2 will focus on the study of the FP of TBEV and two mutants through the design, synthesis, and characterization of fusogenic activities and structure of the monomeric form of the FP. We will demonstrate that the synthetic FP of TBEV can serve as a good model fusion system. Chapter 3 will present the synthesis of a FP with a disulfide bond and a trimeric form of the FP, denoted TFPSS and TFPtr, respectively. Amongst the different peptides designed, TFPSS adopts the most similar structure to the analogous segment in the intact protein and TFPtr which is the FP trimer without any additional polar peptide sequences has the highest fusogenic activity. Chapter 4 will focus on investigating the effect of a range of sample conditions (e.g. ionic strength in the NCC suspension, the suspension concentration, the drying temperature, and magnetic alignment) on the chiral nematic structure and the crystallinity of NCC films. Finally, Chapter 5 will provide a thesis summary, a review of the experimental data, followed by overall conclusions, and lastly an outline of future research directions.

1.2 Methods for structural determination

As already mentioned, the determination of the structure of FPs and NCC films is very important and may provide insight into important biophysical properties. Methods used to determine structures at different levels are: X-ray crystallography and nuclear magnetic resonance (NMR) at the atomic level; circular dichroism (CD) to give secondary structure; electron microscopy and electron cryomicroscopy (cryo-EM) to study morphology. The systems under study here have a certain degree of inherent disorder (e.g. amorphous cellulose, fused membranes), precluding the use of methods such as X-ray crystallography. One can, however, apply methods such as solid-state NMR and CD, which will be described in Section 1.2.1 and 1.2.2, respectively.

1.2.1 Nuclear magnetic resonance spectroscopy

NMR spectroscopy is a powerful method to determine the structure of biomolecules. Unlike X-ray crystallography, NMR spectroscopy can be used to elucidate the structures of proteins and other macromolecules that fail to yield suitable crystals. Structural determination by NMR spectroscopy is usually comprised of several phases: sample preparation, data collection, resonance assignment, restraint generation, and structure calculation. Depending on the state of the sample, NMR spectroscopy can be classified as either solution-state NMR or solid-state NMR. With a sample in hand, a specific pulse

sequence is applied, in which the magnetization is transferred between selected nuclei using radiofrequency (rf) fields. These pulse sequences make it possible to investigate and select specific types of connectivities between nuclei. In order to analyze the NMR data, it is important to find out which chemical shift corresponds to which atom. After resonance assignment, the distance, angle and orientation restraints are generated for the structure calculations. Furthermore, α-helical and β-strand conformations have characteristic ^{13}C and ^{15}N chemical shifts[10]. The assignment of these nuclei in a protein can also help to determine the local conformation of assigned amino acid residues.

In this thesis, NMR spectroscopy is applied to study the structure of the FP of TBEV and determine the crystallinity of NCC films as a function of sample conditions. The determination of the tertiary structure of TBEV FP in the presence of lipids is very important, because the conformation of the peptides surrounded by lipids can provide crucial clues about how the FP performs its function in the native environment. Unfortunately the presence of lipids often precludes the use of methods such as solution-state NMR or X-ray crystallography. By contrast, solid-state NMR is able to provide atomic resolution structural constraints for membrane proteins in the presence of lipids by using uniformly[11-13] or site-specifically[14-16] isotopically labeled samples. The determination of cellulose crystallinity also makes use of solid-state NMR methodology, because the NCC samples consist of dried films.

We have applied ^{13}C Cross-Polarization Magic-Angle Spinning (CP/MAS) to assign the labeled residues in the membrane associated peptides and determine the crystallinity

of NCC films. In MAS NMR, the sample is set spinning about an axis with an angle of 54.74^{o}, the magic angle, with respect to the static magnetic field. The rotation of the sample introduces time dependence to the anisotropic spin interactions, such as the chemical shift anisotropy (CSA), the quadrupolar interaction, and the dipolar interaction. All of these interactions are averaged out more efficiently as the sample spinning frequency increases, leading to a decrease in the sideband intensities and an increase in the center band intensity[17]. Cross-Polarization (CP) is the method to transfer polarization via heteronuclear dipolar couplings in order to enhance the sensitivity of rare nuclei with low magnetogyric ratio, γ, such as ^{13}C and ^{15}N, the S spins[18]. Usually, the magnetization is transferred from abundant nuclei with high γ, such as ^{1}H, the I spins. CP occurs when two rf fields B_I and B_S are simultaneously applied to both I and S spins. When the strengths of the two applied fields match the Hartmann-Hahn condition $|\gamma_I B_I| = |\gamma_S B_S|$, the magnetization can transfer between the two spins[19]. The enhancement of the S spin magnetization is roughly proportional to the ratio of the two magnetogyric ratios $|\gamma_I| / |\gamma_S|$. Therefore, CP/MAS is a useful method to increase the sensitivity of the rare nuclei, the ^{13}C nuclei in this thesis.

1.2.2 Circular dichroism spectroscopy

CD spectroscopy is a method used to quantify the extent of secondary structure present in proteins[20-22]. This method is based on differential absorption of left- and

right-handed circularly polarized light. Different types of protein secondary structures give rise to characteristic CD spectra (Figure 1.2). Therefore, CD spectra can be readily used to determine the approximate fraction of an α-helix conformation, a β-sheet conformation or some other conformation in a molecule. However, CD cannot indicate where the specific detected secondary structure is located within the protein. Despite this, CD is a powerful tool, especially for monitoring changes in secondary structure. Since CD is a quick method that does not require large amounts of sample or extensive data processing, it is possible to apply CD to survey a number of conditions, e.g. temperature, pH, salinity and concentration of denaturing agents.

In addition, CD is also a powerful method to characterize chiral nematic order in liquid crystals. Chiral nematic liquid crystals can selectively reflect polarized light: left-handed liquid crystals reflect left-handed circularly polarized light, whereas right-handed liquid crystals reflect right-handed circularly polarized light[23]. The reflection of circularly polarized light appears as an absorption of the incident light. CD can therefore be used to measure the difference in the apparent absorption of right- and left-handed circularly polarized light for chiral nematic liquid crystals.

1.3 Fusion peptides and TBEV membrane fusion

This section will introduce the basics of the FP and membrane fusion induced by the fusion protein of TBEV. Section 1.3.1 will outline the mechanism of membrane fusion

Figure 1.2 Illustration showing the CD spectra of poly-L-lysine in an α-helix conformation, a β-sheet conformation, and a random coil conformation[24].

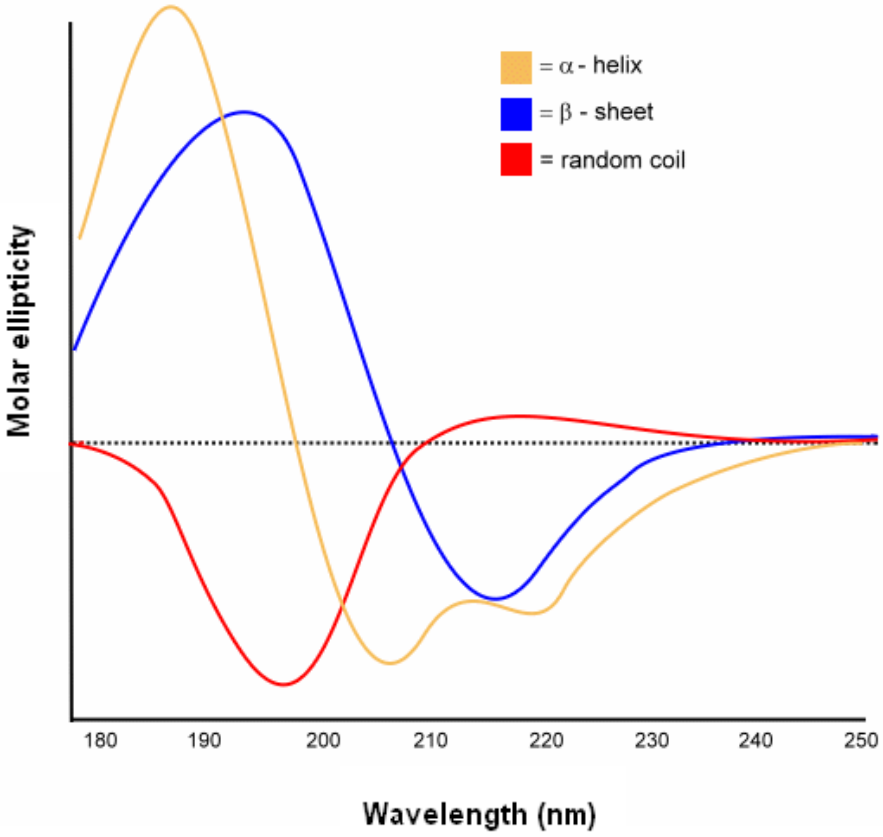

for fusion proteins. Section 1.3.2 will introduce the role of the FPs in membrane fusion and their biophysical and structural properties. Finally, Section 1.3.3 will focus on TBEV membrane fusion and some factors that are important for the activity.

1.3.1 Membrane fusion

Controlled fusion between different membrane compartments at the right time and space is central to the organization of all living organisms. This process is tightly controlled by specific proteins that interact with each other and with lipids to form a

complex at the site of fusion[25]. Many viruses important in diseases, such as the influenza virus, human immunodeficiency virus (HIV), West Nile virus, and so on, are enveloped by a membrane. The mechanism of fusion between the viral and host cell membrane induced by the envelope protein is shown in Figure 1.3. Firstly, the enveloped viruses infect host cells and undergo a process called endocytosis, the end result of which is that the entire virus particle is encapsulated in a liposome inside the cytoplasm of the host cell. Endocytosis is one of the first steps in the replication cycle of the virus in question. In order for replication to continue, the viral genetic material must be released. In other words, the viral RNA must somehow find its way out of two membranes: the viral membrane and the liposome acquired during endocytosis. Since simple diffusion through a membrane is too slow a process, nature devised fusion proteins to ensure rapid release of the viral RNA. Fusion proteins or envelope proteins reside in the viral membrane which forms the outer shell of a virus. After endocytosis, they are therefore located between two membranes. In this environment, the pH is low (about 5). This induces a change in conformation of the envelope protein, the final result of which is membrane rupture and release of the viral gene into the host cell cytoplasm for replication. For all the fusion proteins, the basic principle underlying their capacity to induce membrane fusion is similar in several aspects: the triggered conformational changes that drive membrane fusion; the involvement of a FP which is buried in the neutral conformation but becomes exposed through these conformational changes; and the conversion of the fusion protein into a hairpin-like postfusion structure in which the FP and the

transmembrane domain are juxtaposed[26, 27].

Figure 1.3 Mechanism of pH-controlled envelope protein-mediated fusion[28]. FPs are the only segments that insert into the host cell membrane during the fusion process, and are colored in blue. Viral entry occurs by endocytosis, and the acidic pH in the endosome induces structural alterations in the fusion protein that lead to the FP being exposed and inserting into the host cell membrane. This results in membrane fusion and the release of the nucleocapsid into the cytoplasm.

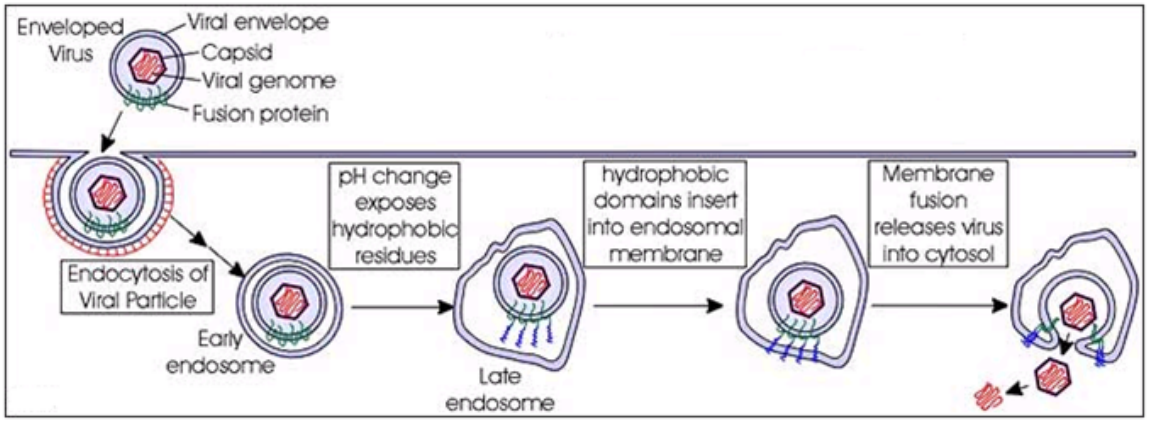

1.3.2 Fusion peptides

As described in the mechanism above, the presence of a FP within the ectodomain lying outside the virus is a common feature of viral envelope proteins[1, 29-33]. The FP becomes exposed during the conformational change of the protein and inserts into the target (host cell) membrane. This segment is usually found to be hydrophobic, with a high degree of residue conservation[29] and enriched in Gly and, in some cases, Ala residues[1, 31, 33]. According to the relative position of the FP in the envelope protein, the FPs can be classified into two categories: Class I FPs are located at the N-terminal end of

the fusogenic transmembrane subunit, or close to it, such as the FPs in the influenza HA2 protein and HIV type-1 gp41 protein; Class II FPs are internal sequences of the polypeptide chain[30], including TBEV FPs, Japanese encephalitis virus FPs, yellow fever FPs, and dengue FPs, which have highly homologous sequences (Figure 1.4)[34-37]. Both the Class I intact fusion proteins and individual FPs have been well studied with regards to their structures and activities, whereas the Class II FPs are much less well characterized.

Figure 1.4 Alignment of amino acid sequences of FPs (residues 98-113) in flavivirus envelope proteins. One representative of the four major human pathogenic serotypes is shown: (TBEV) tick-borne encephalitis virus, strain Neudörfl; (JEV) Japanese encephalitis virus, strain JaOArS982; (YFV) yellow fever virus, stain 17D-204; (DV2) dengue virus type 2.

TBEV	D^{98}RGWGNHCGLFGKGSI^{113}
JEV	D^{98}RGWGNGCGLFGKGSI^{113}
YFV	D^{98}RGWGNGCGLFGKGSI^{113}
DV2	D^{98}RGWGNGCGLFGKGSI^{113}

1.3.2.1 The role of FPs in viral fusion

As briefly mentioned above, FPs are involved in driving the initial penetration of the fusion protein into the target membrane. During the viral fusion process, these peptides have been proven to be exposed and to insert into the lipid leaflet of the target cell,

followed by the aggregation of the viral membrane and host cell membrane[38-42]. Since the short segment corresponding to FP in the envelope protein is important in the fusion process, understanding the role of FPs in viral fusion will have practical consequences in biology, drug development, and pharmacy.

1.3.2.1.1 Hypotheses of the role played by FPs

Though a number of studies have been done on Class I FPs, their exact role in the viral fusion mechanism is still not fully understood. One hypothesis states that these sequences only function as inert anchors. According to this hypothesis, FPs and transmembrane domains in the fusion proteins would tightly tether target and viral membranes, respectively. Fusion would be a direct consequence of the conformational change of the fusion protein that follows formation of the low energy structure in which the FP and the transmembrane domain are juxtaposed[43-46]. However, other studies suggest that the FPs may function as the "active center" of the fusion protein, directly mediating fusion of the viral membrane with a host cell membrane[38, 47]. Furthermore, a direct role of FPs in assisting fusion pore formation has been proposed. This hypothesis suggests the existence of functional membrane-bound structures of these segments[48-50].

1.3.2.2 Interactions of FPs with membranes

In order to verify which hypothesis is valid, it is important to characterize how FPs interact with membranes. Molecular interactions of FPs with model membranes can be studied at several levels. First of all, the ease with which the peptide partitions from an aqueous environment into a membrane affects peptide-membrane association. Once peptide-membrane association is achieved, the sequences retain characteristic locations, conformations and degrees of oligomerization, which are considered important for inducing subsequent membrane perturbations.

This section will begin with a short discussion on the choice of model membranes, and will then expand on the functions of FPs on the membranes, such as peptide penetration, curvature modulation, and bilayer perturbation induced by FPs.

1.3.2.2.1 Model membrane systems

FPs have been studied for their capacity to perturb natural membranes. A good correlation has been found between the capacity of the FPs in the native protein and the capacity of synthetic FPs to induce fusion[51-53]. There are two choices of membrane to study the peptide-lipid interactions: natural membranes and model membrane systems. The advantage of natural membranes is that their composition and asymmetry are similar to those present in the host cell membrane. However, this system is often very complex.

In contrast, lipid model systems (Figure 1.5) with defined structure and composition have been widely used for the analysis of specific effects of the lipid environment on FP activity. Bilayer systems that are represented by large unilamellar vesicles (LUVs) closely resemble the lipid packing density and curvature corresponding to many biological membranes. In addition, the conditions of stressed bilayers, as occurring under certain physiological conditions, have been mimicked by highly curved small unilamellar vesicles (SUVs) produced by sonication. Finally, phospholipid monolayer systems mimic defined packing density conditions. These models allow one to control lateral pressure in the monolayer, a parameter which affects the ability of peptides to penetrate the membranes. Since FP-lipid interactions are initially restricted to the external monolayer of the host cell membrane[54-56], this system is also a good model.

1.3.2.2.2 Insertion of FPs into membranes

Many studies have established that FPs partition from water into membranes because of their highly interfacial hydrophobicity[32, 57-59]. However, the hydrophobic character of FPs could also in principle induce aggregation when they are concentrated in water. The formation of peptide aggregation in solution would prohibit the experimental characterization of the water-membrane peptide partitioning equilibrium. Fortunately, under most experimental conditions, aggregation in solution progresses more slowly than membrane binding, allowing therefore effective insertion of the peptide into target

membranes[57, 60, 61].

Figure 1.5 Structures of multilamellar vesicle (MLV), large unilamellar vesicle (LUV), and small unilamellar vesicle (SUV). The diameters of LUV and SUV are 50 nm – 1 μm and 15 – 50 nm, respectively. Both of them are produced from MLVs.

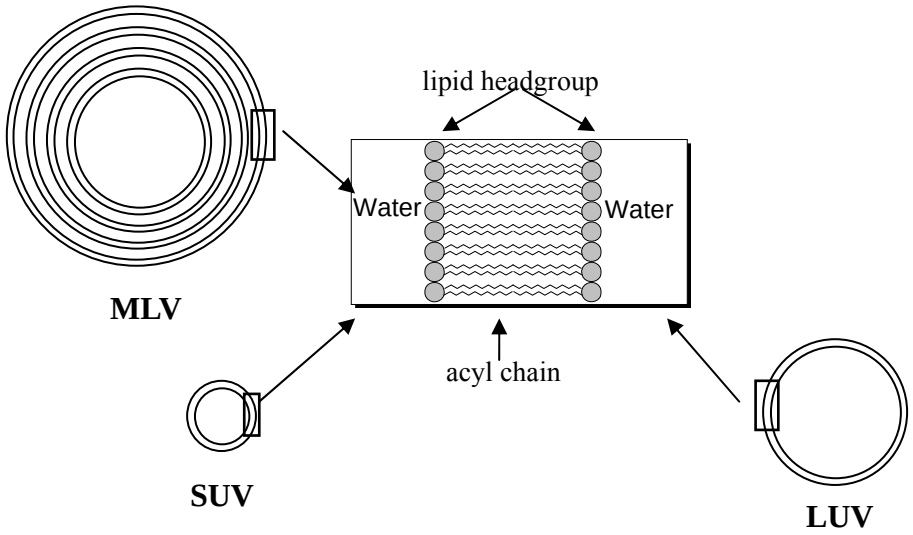

1.3.2.2.3 Curvature modulation by FPs

A common characteristic of many FPs is that they lower the hexagonal phase transition temperature (T_H) of lipid bilayers. This indicates that FPs function by promoting negative curvature[62] (i.e. as seen in Figure 1.10.d), conditions required for membrane fusion via formation of the hemifusion intermediate[63, 64]. For example, FP from influenza virus does not lower T_H at neutral pH where the rate of fusion is slow, but it does at acidic pH where the native protein is fusogenic[65]. Furthermore, a correlation

has been suggested between the fusion activities of viral mutants and the capacity of their FPs to lower T_H, both with the FP of Influenza virus[66] as well as with the FP of Simian Immunodeficiency virus in the intact proteins[67, 68].

1.3.2.2.4 Membrane rupture tension

In order to merge two bilayers into one, each membrane must rupture and reform. The membrane rupture tension determines the energy required to break the bilayers. It has been shown that the influenza FP lowers the rupture tension of membranes, even at low concentrations[69]. This proposed role for FPs to lower the rupture tension is independent of membrane curvature. But it is possible that both the lowering of membrane rupture tension and the promotion of negative curvature are important for accelerating the rate of membrane fusion at different steps of the mechanism.

1.3.2.2.5 Bilayer perturbations induced by FPs

FP binding to either SUVs or LUVs could cause the vesicle suspension to undergo a mixing of lipid vesicles, an activity that may be important for virus-induced membrane fusion. Examples of the lipid vesicle perturbations induced by the HIV-1 FP include leakage of vesicular contents, vesicle aggregation and inter-vesicle mixing of lipids[5]. In general, the synthetic FPs have less activity in accelerating membrane fusion than the

native fusion protein. It is most likely due to the fact that many features of complex viral systems are not present in isolated peptide-vesicle model systems[70]. At least two factors are likely to contribute to this difference between native and model fusion systems. One is that the fusogenic activity might be promoted through oligomerization of protein complexes and/or by the high local concentrations already present in the viral envelope proteins, since viral fusion proteins form stable multimers that self-associate in membranes to form higher order complexes[71]. Furthermore, in the context of the full-length envelope protein, FPs are linked to other regions that may promote structure formation and can therefore participate in accelerating fusion. Evidence for a role of the transmembrane domain and the cytoplasmic tail of the fusion protein has been summarized by Schroth-Diez et al[72].

1.3.2.3 Structures of FPs in membranes

As already mentioned, FPs are generally rich in Gly and, in some cases, Ala[1, 31, 33]. These residues give the FPs an unusual structural flexibility, which is a hallmark of FPs and may be important for their properties. The fact that there are different conformations for FPs to adopt is probably also the reason for many conflicting results that can be found in the relevant literature. Exact experimental conditions and environment could markedly affect the observed structures.

1.3.2.3.1 Structures of Class I model FPs

In general, the secondary structure of a FP can be assessed by the techniques based on the properties of the amide chromophores, such as infrared spectroscopy or CD. More detailed structure could be obtained by the use of X-ray crystallography and NMR. The structures of Class I FPs, such as influenza FP (Section 1.3.2.3.1.1) and HIV-1 FP (Section 1.3.2.3.1.2), have been widely studied. Helical structures have been found in many Class I viral FPs when inserted into a membrane. There is also evidence that the FP can form a β-structure at the amino terminus[73, 74]. In addition to FPs being α-helix or β-strand, there are internal FPs which do not adopt these two common secondary structures[75-77]. There is much less structural information about Class II FPs than Class I FPs.

1.3.2.3.1.1 Structure of influenza Hemagglutinin FP

The fusion protein of influenza viruses is known to be the Hemagglutinin (HA) protein (Figure 1.6), the crystal structure of which was solved more than 20 years ago[78]. There are two polypeptide chains in each subunit of the HA trimer, HA1 and HA2. The HA1 chains contain the receptor binding sites for the attachment of the virus to the host cell surface. The HA2 chains located at the extreme N-terminus of HA are thought to be primarily responsible for promoting fusion. The HA2 consists of a FP segment with 20-24 residues as defined by the residue boundary of nine polar residues[79]. Because this

polar boundary adopts a disordered structure, the FP in HA2 is therefore likely to serve as an independently folded domain when it inserts into the lipid bilayer. Its structure is defined and stabilized by interactions with the membrane.

Figure 1.6 Molecular structure of HA determined by X-ray crystallography[80]. The subunits of HA1 and HA2, and FP in HA2 are colored in blue, red, and green, respectively. Coordinates were obtained from PDB accession no. 2VIU.

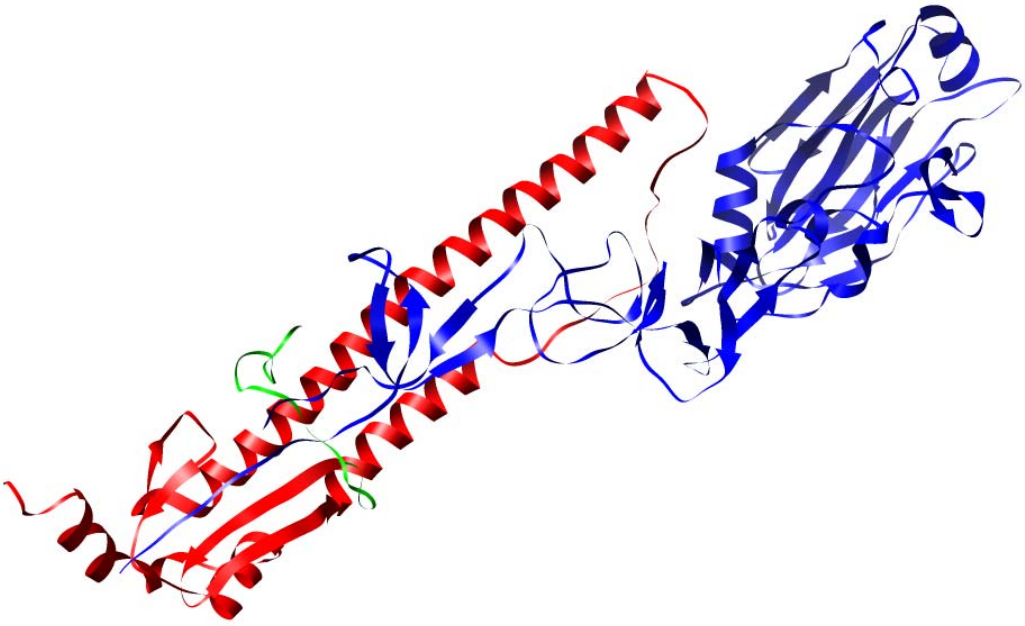

The secondary structure of the influenza FP, consisting of the first 20 residues of HA2, was determined by CD experiments which show that the peptide is approximately 50% helical in liposomes or other apolar enviromens[81-83]. When the peptide length is increased to 23 residues, a small amount (20-30%) of β-structure is adopted, in addition to the predominantly α-helical conformation[84].

Because the isolated influenza FP is not or only sparingly soluble in water, it is usually mixed with lipids in organic solvents and rehydrated after solvent removal, or added from organic solvent to performed liposomes before spectroscopic analysis. The conformation of these hydrophobic peptides is often dependent on the solvent used in the reconstitution procedure[85]. Furthermore, this procedure does not always result in equilibrium structures of conformationally flexible peptides in membranes[85]. In order to alleviate these potential sources of error, a host-guest peptide system has been designed, which consists of the FP sequence and a polar carrier peptide via a flexible linker linked at the C-terminus of FP segment[60]. For example, the mimic host-guest peptide of HA FP, P20H7, contains the sequence of the 20-residue wild-type FP and the linked polar carrier with the sequence of GCGKKKK. CD spectroscopy indicates that this peptide adopts ~ 90% random coil structure in solution and is ~ 48% helical in lipid bilayers[60].

The structures of HA2 FP bound to detergent micelles in solution were determined by ^{1}H-NMR at pH 7 (Figure 1.7.a) and pH 5 (Figure 1.7.b)[56]. In this investigation, the chemical shifts of protons have been assigned using total correlation spectroscopy (TOCSY), and the distance constraints were obtained from nuclear Overhauser enhancement spectroscopy (NOESY). With these data, the structures of the HA FP have been calculated. A well-defined N-terminal α-helix extending from residue 2 to residue 10 is found in both structures. A turn is formed by residues 11, 12, and 13 and redirects the polypeptide chain by approximately 60^{o}, thus forming a "V" with an opening angle of ~ 120^{o}. The C-terminal arm forms a short 3_{10}-helix consisting of residues 14-18 at pH 5,

Figure 1.7 Structures of wild-type HA2 FP and its mutants determined by solution-state NMR in DPC micelles[56, 86-88]. (a) Structure of wild-type FP at pH 7 (PDB accession no. 1IBO). (b) Structure of wild-type FP at pH 5 (PDB accession no. 1IBN). (c) Structure of G1S at pH 5 (PDB accession no. 1XOO). (d) Structure of G1V at pH 5 (PDB accession no. 1XOP). (e) Structure of W14A at pH 5 (PDB accession no. 2DCI). (f) Structure of F9A at pH 5 (PDB accession no. 2JRD)

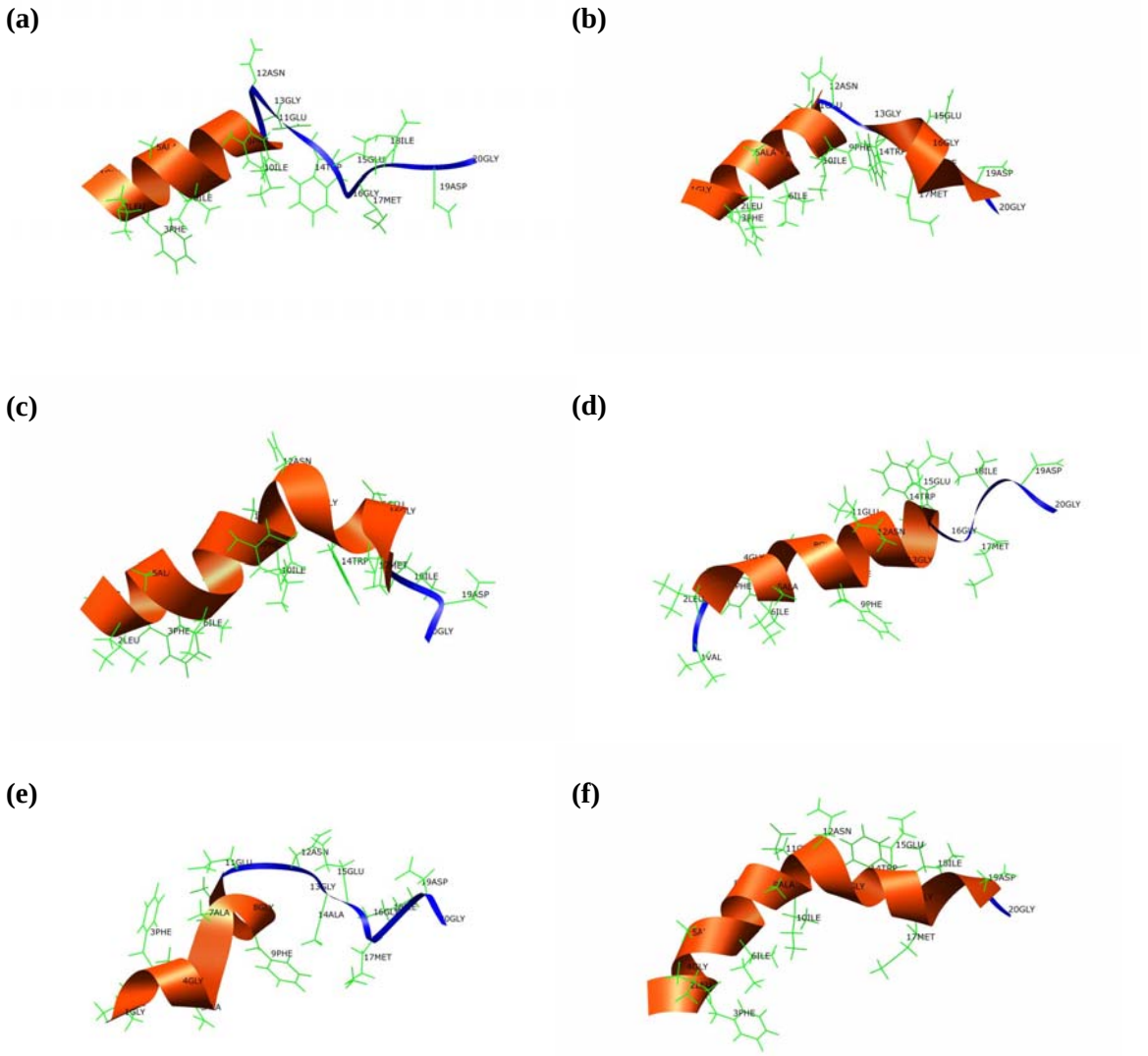

but does not form any regular secondary structure at pH 7. In the N-terminal helical segment, all bulky hydrophobic residues are on the inner side and a ridge of conserved Gly is on the outer side of the angled structure. The C-terminal 3_{10}-helix of the pH 5

structure is amphiphilic with many bulky aromatic residues in the cavity of the "V", thus creating a completely hydrophobic pocket. However, the open structure of the C-terminal arm at pH 7 does not possess this amphiphilic area.

The structures of some functionally important FP mutants have also been determined by solution-state NMR in detergent micelles. The G1S mutant leads the full-length HA to display hemifusion activity [50], which is defined by a state in which fluorescent lipid dyes exchange between two closely apposed membranes, but do not communicate across a fusion pore. The overall shape of G1S (Figure 1.7.c) is very similar to that of the wild-type peptide[86]. Both molecules form an angled amphiphilic structure with all bulky apolar residues lining the hydrophobic pocket of the "V". Only the smooth glycine ridge at the top of the N-terminal helical arm is disrupted by the Ser 1 residue. The G1V mutant displays impaired fusion activity, so that it does not even proceed to hemifusion[50]. The NMR structure of this peptide (Figure 1.7.d) is quite different from the others. G1V adopts a very irregular, approximately linear amphiphilic helical structure that is oriented about 10^{o} from the membrane surface[86]. All the structures underline the functional importance of the kink in the HA FP and indicate a structural role for the glycine ridge in viral membrane fusion. This observation is further supported by mutations which stabilize the kink structure. For instance, the mutation of W14A has hemifusion activity but does not induce fusion[87]. The structure of this mutant (Figure 1.7.e) contains a flexible kink pointing out of the membrane[87]. In contrast, the mutation of F9A on the other side of the kink has no significant effect on the fusion activity of the FP.

Furthermore, a similar kinked structure as wild-type FP is adopted by this mutant (Figure 1.7.f)[88]. Therefore, the membrane fusion induced by influenza FP requires a certain fixed angle boomerang structure pointing into the membrane.

Recently, solid-state NMR has been applied to study the structure of HA FP bound to PC/PG LUVs. Two-dimensional $^{13}C/^{13}C$ and $^{15}N/^{13}C$ correlation spectra were reported for the membrane-bound FP. The ^{13}C chemical shift assignments are those characteristic of helical shifts rather than β-strand ^{13}C shifts[89]. This chemical shift-based conformation is consistent with previous work[56]. However, the spectra contained additional peaks whose shifts were not consistent with a helical conformation, indicating that there were multiple conformations in the HA FP, which is consistent with the infrared spectra showing populations of helical and β-strand structures in HA FP bound to a PC/PG lipid mixture[61].

1.3.2.3.2.2 Structures of HIV-1 FP

The envelope protein from HIV mediates the specific attachment of viral particles (virions) to host cell surface receptors and promotes membrane fusion[25]. Upon attachment, the envelope protein is cleaved to yield two noncovalently associated subunits, gp120 and gp41[90]. The surface subunit gp120 contains the binding sites of the primary cellular receptor CD4 for viral tropism[91]. The transmembrane domain gp41 is thought to be primarily responsible for the fusion activity. The ectodomain of gp41, with

about 170 residues lying outside the virus, has a trimeric bundle structure[41, 92, 93]. The HIV FP consists of about 20 residues at the N-terminus of gp41. A synthetic peptide with this sequence can induce fusion between unilamellar lipid vesicles and therefore serves as a model fusion system by itself.

Solution NMR and CD have been used to determine the structure of monomeric FP of HIV in detergent micelles[94]. The FP of HIV inserts into the micelles and adopts a structure which is about 50% helical (Figure 1.8). The helical segment of the peptide penetrates deeply into the hydrophobic core of the micelles, while the turn structure, which is extended between residue 16 and 23, lies on the surface. Recent studies indicate that the α-helical segment may extend from Ile 4 to Met 19[95, 96], with Ile 4 to Ala 15 being fully shielded from solvent, and Gly 3 and Gly 16 being found at the micelle-water interface[97].

The conformation of membrane-associated HIV FP has been investigated using biophysical techniques including FTIR, CD and solid-state NMR[58, 98, 99]. In contrast to the structures of HIV FP in detergent micelles, distinct populations of HIV FP bound to lipid LUVs are observed. At low peptide-to-lipid ratios of about 1:200, the peptide adopts an α-helical structure when bound to negatively charged vesicles. At higher peptide-to-lipid ratios of about 1:30, a β-strand conformation is observed for the FP[98]. In addition, the structure of HIV FP is dependent on the concentration of ions. When bound to POPG LUVs at peptide-to-lipid ratios of 1:65, the peptide adopts mainly an α-helical conformation in the absence of Ca^{2+}. In contrast, the presence of Ca^{2+} promotes the

Figure 1.8 Solution ^{1}H-NMR structure of HIV FP in SDS micelles (30 conformers; PDB accession no. 2ARI)[100].

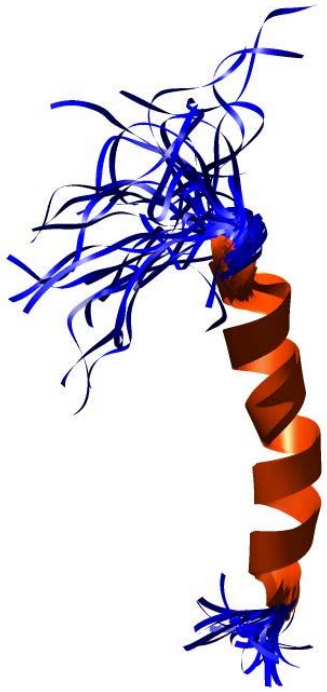

formation of an extended antiparallel β-strand conformation[99]. In the absence of Ca^{2+}, the peptide can also adopt a β-strand structure when associated with neutral liposomes[58]. β-strand conformation is also favored in the host-cell-like membranes containing cholesterol[101-103]. Furthermore, the FP trimer of HIV has been synthesized and the conformation of associated strands has been investigated using solid-state NMR with the synthesized HIV FP trimer. In the membrane without cholesterol, predominant helical conformation was observed between Leu 7 and Phe 11, while in the host-cell-like membranes containing cholesterol, β-strand conformation was observed at Leu 7 and Leu 8[15, 104, 105].

1.3.3 TBEV membrane fusion

TBEV is a typical flavivirus. It exhibits one of the fastest and most efficient fusion machineries, probably due to its peculiar, smooth-surfaced envelope structure. This is in contrast to the spiky surface of most other enveloped viruses (a detailed comparison of the structures will be described in Section 1.3.3.5). The structures of both the prefusion and postfusion conformations of TBEV fusion protein, E protein, have been determined by X-ray crystallography. Therefore, it is possible to understand some of the mechanistic details of the TBEV fusion process at a structural level.

1.3.3.1 Structure of the E protein

The atomic structure of the E protein from TBEV (Figure 1.9.a) has been determined by X-ray crystallography in its prefusion conformation[106] (the second stage in Figure 1.3), by using a soluble truncated form of the E protein which lacks the insoluble transmembrane anchor, namely the 50 residues between the viral membrane and the crystallizable ectodomain. This form of the E protein represents the metastable and neutral pH structure of the protein. The native protein forms a homodimer in a perpendicular orientation to the membrane normal of mature virions. Each monomeric subunit of E protein is oriented antiparallel to the other monomer in the dimer. Each of the E protein monomer is comprised of three distinct domains: DI, DII, and DIII. DI, a

Figure 1.9 Molecular structures of TBEV E protein determined by X-ray crystallography[106, 107]. DI, DII, DIII and FP are colored in red, yellow, blue, and magenta, respectively. (a) Prefusion structure of TBEV E protein (PDB accession no. 1SVB); only one of the molecules in the dimer is shown. (b) Postfusion structure of TBEV E protein trimer, in which two of the monomeric subunits are colored in gray (PDB accession no. 1URZ).

(a)

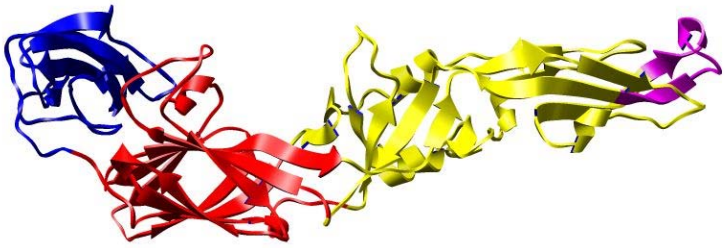

(b)

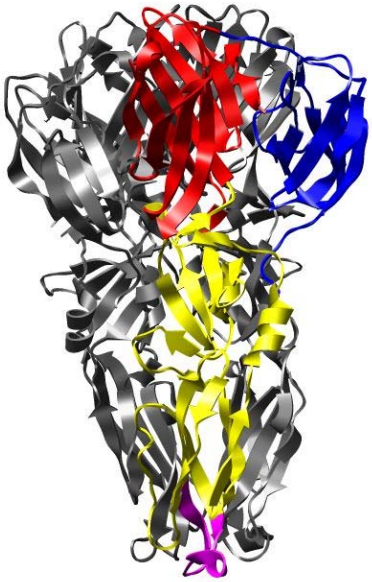

central β-barrel domain, contains the amino terminus. It interacts with DII via two long, disulfide-stabilized loops. DII is an elongated dimerization region. A loop located at the tip of DII is almost completely conserved and functions as an internal FP, which is buried at the dimer interface, thus shielded from interacting with membranes in its prefusion configuration[108]. A C-terminal, immunoglobulin-like module, DIII is flanked by DI on the opposite side[106].

1.3.3.2 Fusion properties

TBEV membrane fusion occurs at the relatively high pH threshold of around 6.6, so that early endosomes can induce fusion[109-111]. The analysis of pyrene-labeled virus with model liposomes suggests that the condition where fusion occurs has a broad optimum range below pH 6.2[110]. Fusion induced by the E protein occurs over a temperature range 15-37 ℃, and under these conditions, the initial rate of fusion was 30% per s without the appearance of any detectable lag phase preceding the onset of the actual fusion reaction. It apparently does not require binding to specific receptors[110]. The specific features of the organization of the E protein on the surface of the TBEV virions may result in the extraordinary efficiency of fusion. The fusion protein of TBEV has an orientation which is perpendicular to both the host-cell and viral membrane normal, allowing close proximity of the two membranes at the initial stage of fusion. Other aspects that affect fusion will be introduced in following sections.

1.3.3.3 Effect of lipids in fusion

The lipid composition of target membranes plays an important role in TBEV-mediated fusion[111]. The presence of cholesterol promotes fusion, even at the early steps in the mechanism, such as membrane attachment and subsequent structural rearrangement of the E protein, which might be dependent on interactions with the 3β-hydroxyl group of cholesterol[111]. However, the precise nature of these interactions has not been elucidated yet.

1.3.3.4 Fusion driven by structure transitions

Experiments have shown that slightly acidic pH, as it occurs in endosomes, leads to a complete rearrangement that converts the E dimer into a postfusion trimer[112], which is significantly more thermostable than the E dimer[113].

The structure of the full-length E trimer has not yet been determined. However, structural data on a single monomer of the TBEV E protein in this low-pH form were obtained by X-ray crystallography (Figure 1.9.b)[107]. Comparison with its prefusion conformation suggests that there are conformational changes during the conversion of dimers to trimers. The conversion involves the rearrangement of the E proteins from a dimer aligned perpendicular to the viral membrane normal, in which the monomeric subunits are arranged antiparallel, into a parallel trimer that is oriented parallel to the

membrane normal. Even though no significant refolding of the polypeptide chain is involved in the transitions and the structural integrity of the three domains does not change, there is reorientation of the domains relative to each other. The junction between DI and DII rotates by about 20^{o}. On the other hand, DIII relocates from the end of the E protein to the side of DI. This must involve the reduction of the strength of the interactions at the interface between DI and DIII of the E protein dimer, including a number of salt bridges, hydrogen bonds and van der Waals contacts.

Based on this and other structures of Class II fusion proteins, a mechanism of TBEV membrane fusion has been proposed (Figure 1.10). Firstly, the low pH in the endosomes induces the dissociation of the E dimers into monomers, which results in the exposure of the FP loop at the tip of DII. The FP is buried in the neutral dimer conformation. The exposure of the FP makes it possible for the FP to insert into the target membrane, thereby triggering the fusion process[112, 114, 115]. The FP can only insert into the outer leaflet of the target membrane due to the presence of charged residues and exposed carbonyl groups on the outer rim of the peptide[77]. Then the cage-like structure of the E proteins is disintegrated by the relocation of DIII, which leads to hairpin formation and trimerization. At this stage, an intermediate is formed during the fusion process, in which only the contacting membrane leaflets are fused, generating a so-called lipid stalk[116]. Finally, the fusion pore forms and in the fused membrane, the conformation of postfusion E protein has the FPs and the transmembrane domains at juxtaposed positions.

Figure 1.10 Schematic of the proposed stages of the TBEV membrane-fusion process. Color codes: viral membrane, blue; target membrane, grey; Domain I, red; Domain II, yellow; Domain III, dark blue; FP, magenta; transmembrane domain, green. (a) Metastable E dimer at the surface of a mature virion. (b) Low pH-induced dissociation of E dimer and interaction of E monomers with the target membrane via FPs. (c) Initiation of hairpin formation and E trimerization through the relocation of Domain III. (d) Hemifusion intermediate in which only the outer leaflets of the two membranes have mixed. (e) Generation of the final postfusion structure and opening of the fusion pore.

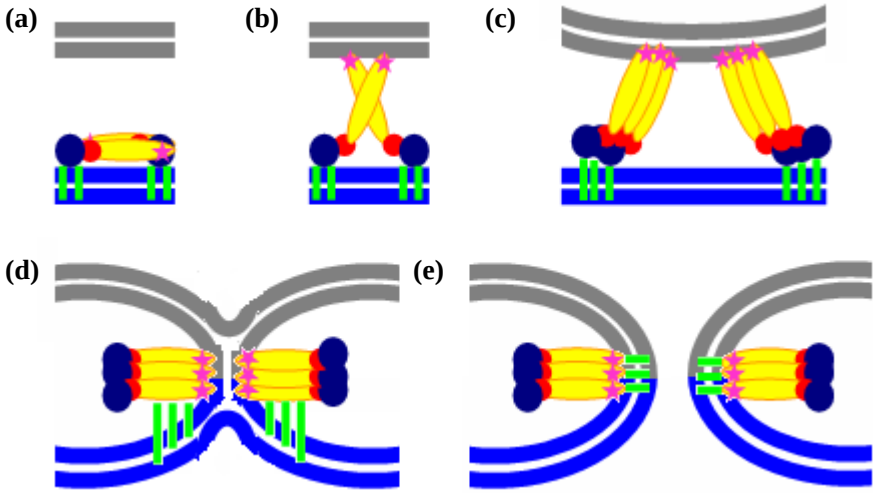

1.3.3.5 Comparative aspects of viral membrane fusion

Since the membrane fusion induced by TBEV and other flaviviruses is almost same, this section will compare the characteristic features of membrane fusion induced by flavivirus and other kinds of enveloped viruses, in order to further understand the mechanism of this faster and more efficient fusion process.

1.3.3.5.1 Comparison of flavi- and alphaviruses

Flaviviruses and alphaviruses both belong to the Class II enveloped viruses. Although the fusion proteins of these two kinds of viruses (E and E1, respectively) do not exhibit an apparent sequence homology, they have strikingly similar structures[117]. Most importantly, the E1 monomer displays the same overall domain organization as the flavivirus E monomer and the internal FP loop is located at the same relative position in DII in both cases[106, 117-121]. Further similarities between E and E1 proteins include: strict dependence on acidic pH for fusion; putative involvement of conserved His residues at the DI-DIII interfaces acting as proton acceptors for the low-pH trigger[107, 121]; conversion into a trimer at acidic pH, with a similar overall configuration in both cases[77, 107, 122]; and finally, the presence of soluble forms of neutral E and E1 that can be converted into the trimeric postfusion conformation at acidic pH through their interactions with lipid membranes[114, 123-125]. Based on these similarities, the overall fusion processes of flavi- and alphaviruses are believed to follow very similar pathways[27].

Despite these striking similarities, there are also a number of important differences between these two kinds of Class II fusion proteins. The most significant difference is the fact that in the alphaviruses, a second protein (E2) forms a heterodimeric complex with E1 at the surface of infectious virions[107]. Eighty trimeric E2-E1 complexes form spikes at the surface of mature alphaviruses[126, 127], in contrast to the smooth surface of flaviviruses. It is likely that the somewhat slower fusion rate of alphaviruses compared with

flaviviruses[128] is a consequence of the more complex nature of the alphavirus surface, with the E2 protein residing on top of the membrane-proximal fusion protein E1 in the heterotrimeric spikes. Indeed, many more structural rearrangements (e.g. E2 must move out of the way before E1 can rearrange and mediate fusion) are need in alphaviruses. Finally, in contrast to flaviviruses, alphavirus fusion is absolutely cholesterol-dependent[111, 129, 130]. The absence of cholesterol in the target membrane would prohibit the fusion induced by alphaviruses[129, 131-134]. However, the structural details of the underlying mechanism are not yet known.

1.3.3.5.2 Comparison of flavivirus and Class I viral fusion mechanisms

The comparative structural analysis of the E proteins of flaviviruses and Class I fusion proteins indicates that the only similarity between them is that both of the fusion proteins undergo triggered conformational changes and adopt a more stable, hairpin-like structure in the postfusion stage in the membrane fusion mechanism[26, 27]. The end result is the same but the steps of the fusion mechanism are different because of their completely different molecular architectures as described in Section 1.3.2, Furthermore, the two kinds of fusion proteins display significant differences with respect to the fusion triggers. With certain Class I viruses, it has been shown that fusion could be induced not only by the physiological trigger, such as an acidic pH[135], but also by alternative experimental triggers, such as elevated temperature or slightly denaturing

conditions[136-139]. The same treatment, however, did not induce fusion in the case of Semliki Forest virus (SFV)[140], which is a kind of alphavirus, or TBEV[113]. In fact, the elevated temperature led to denaturation of the E protein and loss of activity. At least in the case of influenza HA, it is likely that these different properties are related to the proposed capacity of HA2 to adopt its stable, postfusion, hairpin-like conformation spontaneously upon the release of the external HA1 clamp[141]. Hairpin formation in Class II fusion proteins, however, requires the relocation of DIII and thus the release of FP from an intramolecular clamp held by DI-DIII interactions in the prefusion conformation. The dissociation of this domain interface apparently does not occur spontaneously at elevated temperature or upon slight denaturation, but is dependent on the specific protonation of certain, still unidentified amino acid residues.

1.4 Cellulose structure

As mentioned above, the second type of biomolecules studied in this thesis is nanocrystalline cellulose (NCC). Cellulose is the high-molecular-weight polysaccharide composed of β-(1-4)-D-glycan subunits with a general formula $(C_6H_{10}O_5)_n$, where "*n*" is the degree of polymerization. Depending on the species, the value of *n* ranges from several hundred to over ten thousand[142, 143]. Cellulose is the primary structural component of cell walls, where the molecular chain of cellulose consists of 60 to 70 cellulose threads, forming supermolecular structures, called microfibrils, as shown in Figure 1.1.b.

In this section, the following levels of cellulose structure will be discussed separately: constitution, configuration, and conformation.

1.4.1 Constitution of cellulose

The constitution of cellulose is defined as the nature and sequence of the linkages in cellulose, i.e. the architecture of the main chain[144]. The constitution of cellulose has been studied rather comprehensively by applying common methods of carbohydrate chemistry, such as hydrolysis, methylation, and periodate oxidation. The results of acid hydrolysis of cellulose show that pure cellulose consists only of D-glucose[145]. The stepwise degradation of the cellulose chain indicates that the cellulose is an unbranched linear polymer of 1-4 bonded D-glucose (Figure 1.11). As already mentioned, the degree of polymerization of natural cellulose is species-dependent. For instance, cellulose from wood pulp has typical chain lengths ranging from 300 to 1,700 units; cotton and other plant fibers, as well as bacterial celluloses, have chain lengths between 800 and 10,000 units[146].

1.4.2 Cellulose configuration

The configuration of cellulose is the spatial arrangement of atoms or groups of atoms without consideration of possible rotation around one or several single covalent bonds[144].

Figure 1.11 Constitution of the cellulose macromolecule.

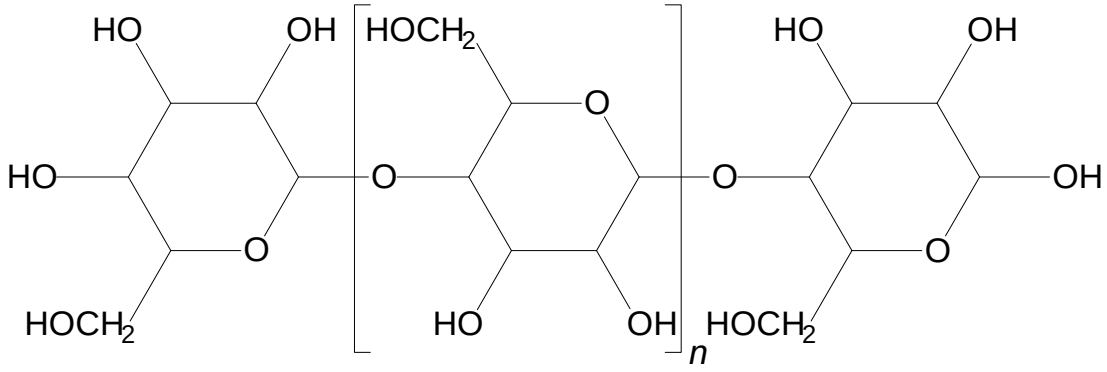

Thus the configuration is the basic static stereochemistry and is represented by a three dimensional model, or a three dimensional or projection formula. In solution, glucose is comprised of an equilibrium mixture of α- and β-anomeric forms (Figure 1.12.a)[147]. Optical rotation of glucose in solution ranges from $[\alpha]_d^{20}$ + 111° (α-form) to $[\alpha]_d^{20}$ + 19.2° (β-form). The difference between α- and β-anomers of glucose is the position of the hydroxyl group at the anomeric carbon atom (C_1) in relation to the plane of the ring. The α-form has the hydroxyl group in the axial position, whereas the β-form has it in the equatorial position[148]. The alteration of configuration of the OH-group at C_1 results in substantial changes in the IR- and Raman spectra[149, 150]. Signatures in the IR-spectra of cellulose indicate that cellulose consists of glucoside linkages with β-configuration (Figure 1.12.b)[151, 152]. The chair structure of cellulose is stabilized by the fully equatorial configuration of β-linked glucopyranose residues, minimizing its flexibility.

Figure 1.12 (a) Configuration scheme of an equilibrium mixture of glucose in solution. (b) Configuration of the cellulose macromolecule, with the carbon atom position indicated.

(a)

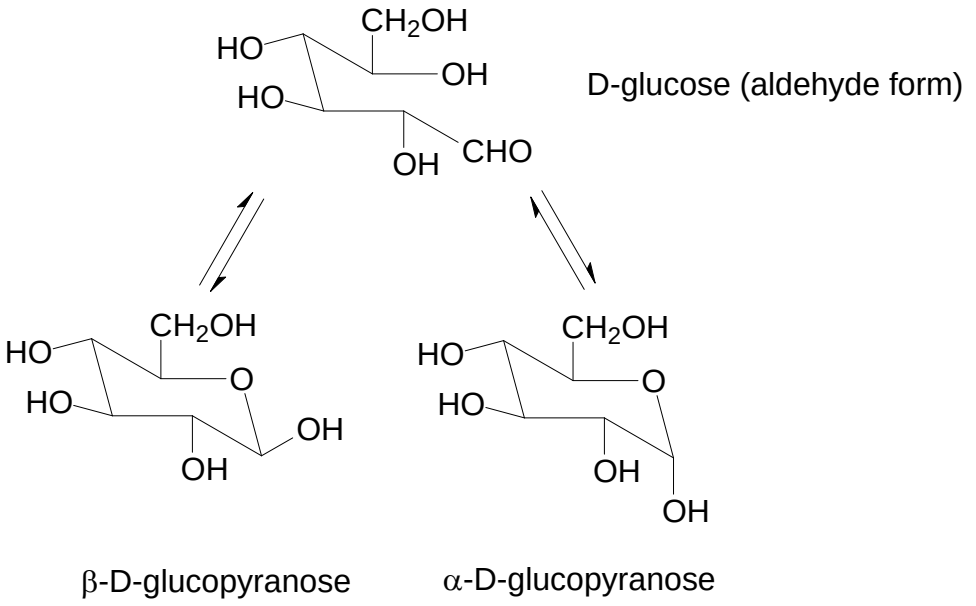

(b)

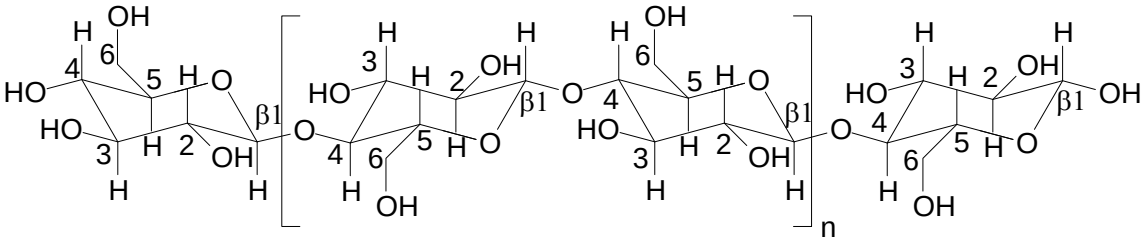

1.4.3 Cellulose conformation

The conformation of native cellulose is governed by intra- and inter-molecular hydrogen bonds[153]. The presence of intra-molecular (O3-H→O5' and O6→H-O2') and intra-strand (O6-H→O3') hydrogen bonds results in a flat the network of cellulose chains and allows the more hydrophobic ribbon faces to stack (Figure 1.13). Each of the β(1→4)-linked glucose residues in a chain is rotated 180^{o} around its longitudinal axis and with

respect to its neighboring residues. The glycan chains line up laterally to form sheets and these sheets stack vertically. The presence of extensive intra- and intermolecular hydrogen bonds makes the cellulose tend to form crystals that are partially insoluble in aqueous solutions.

Figure 1.13 Conformation of a sheet of cellulose I_{α}, in which the hydrogen bonds are represented by dashed lines.

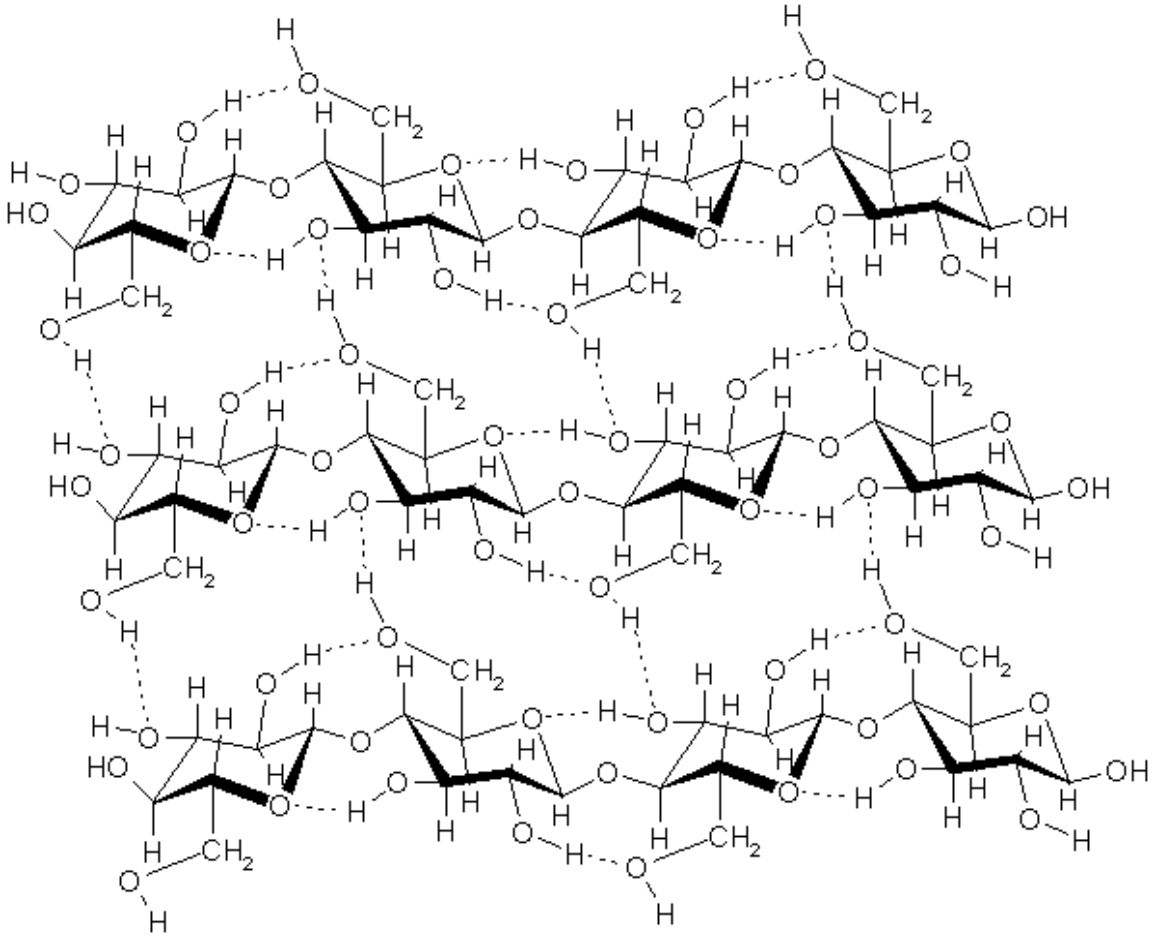

Cellulose consists of ordered and disordered regions, i.e. the amorphous and crystalline domains, respectively. The crystalline domains of native cellulose have been considered to consist of metastable cellulose I, which consists of parallel cellulose strands

with no inter-strand hydrogen bonds. This cellulose I is regarded as being composed of two distinct crystalline forms, namely I_α (triclinic) and I_β (monoclinic)[154]. The proportions between the two lattice types can vary and are dependent on the origin of the native celluloses[154, 155]. I_α is found more commonly in algae and bacteria, while I_β is the major form in higher plants. Therefore, native celluloses are divided into two classes according to the major crystalline component being form I_α or form I_β.

The distance of fibre repeats in cellulose I_α and cellulose I_β are the same: 1.043 nm for the repeated chains in the interior and 1.029 nm on the surface of the crystallites[156]. But the displacements of the sheets relative to one another are different in the two forms. The neighboring sheets of cellulose I_α, which consist of identical chains with two alternating glucose conformers, are regularly displaced from each other in the same direction. However, cellulose I_β consists of two conformationally distinct alternating sheets, in which the 2-OH and 6-OH groups both change orientations so that the hydrogen bonding pattern is altered. Each sheet of cellulose I_β is made up of crystallographically identical glucose conformers. The sheets are staggered by half the length of a glucose unit[157-159]. It is possible to interconvert between these two crystalline forms of cellulose I by bending cellulose in a plane normal to the hydrogen-bonded sheets of chains during biosynthetic microfibril formation, which causes a longitudinal displacement of the sheets with respect to one another[160].

Other structural forms of cellulose are derived from native cellulose I. The recrystallization of cellulose I gives the more thermodynamically stable cellulose II

structure, which contains an antiparallel arrangement of the strands and some intersheet hydrogen bonds. There are two different types of anhydroglucose with different backbone structures in the cellulose II structure[161]. Another structural form of cellulose is cellulose III, which is formed from cellulose I by mercerizing in ammonia. The structure of cellulose III is similar to that of cellulose II except that the chains are parallel as in cellulose I_α and cellulose I_β[162].

1.5 Conclusions

This chapter has introduced the methods to determine the structure of FPs and cellulose, and some important features of TBEV membrane fusion and cellulose structure. The FPs of all enveloped viruses have specific compositions, specific interactions with membranes, and various structures. The relationship between the structure of Class I FPs and their fusion activities has been studied extensively over the years, but less is known about their Class II counterparts. The E protein from TBEV, as a typical Class II fusion protein, displays extraordinarily fast and efficient fusogenic activity, but the structure of its FP associated with lipid bilayers is still unknown. The ability to design, synthesize and characterize the FPs would help us to further understand what the role of Class II FPs is during fusion and to elucidate the mechanism of fusion induced by flaviviruses.

The constitution and configuration of cellulose are well known and constant in many types of cellulose. However, the chiral nematic structure and crystallinity of cellulose are

variable and dependent on the origin of the sample and its preparation. Since the chiral nematic properties and degree of crystallinity strongly influence the physical and chemical behavior of such a polymer, the investigation of cellulose structure is very important. Ultimately, being able to control chiral nematic phase and crystallinity of NCC will lead to the production of cellulose-based materials with specific characteristics.

This thesis will present my efforts towards the synthesis and characterization of the FP of TBEV. It will also present the structural characterization of NCC films prepared using a range of sample conditions.

Chapter 2: Design, synthesis, and characterization of the TBEV FP and two mutants

2.0 Introduction

Chapter 1 presented findings from previous studies of Class I FPs and also data on the TBEV fusion protein. It also illustrated how designing and characterizing FPs can be used to study the mechanism of membrane fusion induced by FPs. Synthetic FPs provide a useful model system in which the contributions of structure to the activities of the FPs can be studied in a tractable manner. This chapter will describe the design, synthesis and characterization of the wild-type (WT) FP of TBEV and two other mutants L107F and L107T, which had previously been shown to display reduced activity in the intact E protein[108].

Section 2.1 of this chapter will outline the background and rationale for the synthesis of the isolated TBEV FP. Section 2.2 will focus on the synthesis and characterization of the synthesized TBEV FPs and a discussion of the experimental results will also be presented. Section 2.3 will summarize the results from this chapter and provide some conclusions from the analysis of the experimental data. Finally, Section 2.4 will outline the experimental conditions.

2.1 Rationale for synthesizing TBEV FP

As introduced in Chapter 1, depending on the position of the FP in the envelope protein, there are two classes of FPs. Class I FPs, including the FPs in the influenza HA2 and the HIV-1 gp41 proteins, have been well studied. The other architecturally and evolutionarily distinct class of FPs (Class II) is found in flaviviruses, such as yellow fever, West Nile, and dengue viruses, and in alphaviruses, such as Semliki Forest virus (SFV) and Sindbis virus (SIN).

In TBEV, the FP resides on the envelope glycoprotein E, which contains about 500 amino acids. Glycoprotein E has three domains, with folding based largely on β-sheets, as outlined in Section 1.3.3.1. Domain II, which has an elongated, finger-like structure, bears a peptide loop at its tip with a hydrophobic sequence which is highly conserved among all flaviviruses[106]. Experiments on TBEV show that this peptide loop (residues 100-113) is responsible for attachment of soluble E ectodomains to target membranes and the hydrophobic residues are essential for its activity[108]. These and other data, including results from studies of alphaviruses[163, 164], which have a very similar peptide loop structure, support the view that the peptide loop of class II fusion proteins has a function analogous to that of the N-terminal FP in class I fusion proteins: insertion into the host-cell membrane and provision of an attachment point for drawing host and viral membranes together[40].

Even though the structures of the ectodomains of E proteins have been determined in

their prefusion and postfusion states[77, 106, 117, 118], the structural changes of Class II FPs during the fusion events (Figure 1.10) are still unclear. Since studying the structure of a 500 residue protein embedded in a membrane bilayer is currently impossible, it becomes essential to develop a model fusion system consisting of the short FP segment only. For this model to be valid and provide insight into the mechanism of fusion, it must possess the same properties as when it is part of the envelope protein.

2.2 Results and discussion

This section will describe the design and synthesis of three TBEV FPs: WT, L107F and L107T. The synthesized WT FP and two other mutants will be characterized by biophysical techniques followed by a discussion of the characterization data.

2.2.1 Rationale for using SSPS as method for peptide synthesis

Understanding the specific biological activities of the TBEV FP requires detailed information about its structure and function. Our ultimate goal is to use unlabeled or selectively labeled peptide to obtain the above information when the peptide is in its native environment. Peptides can be produced by expression or solid-phase peptide synthesis (SPPS). A number of recombinant-protein-expression based strategies have been devised to selectively label a protein[165], but they suffer from the limitation that only

a particular type of amino acid or segment of the amino acid skeleton becomes labeled[166, 167]. It would therefore be useful for the structure-function studies of membrane proteins to have a methodology that provides access to site-specifically labeled membrane proteins in sufficient quantities for NMR and other spectroscopic techniques. SPPS based methods are the classic approach to the site-specific labeling of membrane proteins on the large scale needed for biophysical and spectroscopic studies. However, typical proteins in the range of 70-100 amino acid residues push the limits of synthetic accessibility. Since in our case, use of unlabeled or selectively labeled small peptides (~20 residues) is sufficient, we therefore chose SPPS to synthesize the target peptides.

2.2.2 Peptide design

The WT FP sequence was designed according to the amino-acid sequence of the FP segment in the E protein of TBEV. As described in Chapter 1, the *cd* loop at the tip of domain II in the E protein of TBEV is contained within a sequence (residue 100-113) that is almost fully conserved in all flaviviruses. This sequence is quite hydrophobic and rich in glycine. It has been proposed that it is important for the fusogenic activity of the virus[168]. The X-ray crystallographically determined structure of E protein from TBEV indicates that this sequence consists of a loop (residue 100-108) and a β-strand (residue 109-113)[106]. In order to preserve the β-strand structure in the synthetic target peptide sequence, the other antiparallel β-strand (residue 93-99) has been added at the

N-terminus of the *cd* loop sequence. The amino acid sequence of the target 21-residue WT polypeptide chain is shown in Figure 2.1. To investigate the fusogenic activity of the synthetic FP, we made mutant peptides and investigated their fusion-related properties. Our goal was to introduce amino acid substitutions that would lead to functional changes but would not disrupt the structure. One choice was to mutate Leu 107. This residue, like most of the FP region, is almost completely conserved among flaviviruses, but there are a few exceptions: the Tick-borne Powassan virus[169], the mosquito-borne Japanese encephalitis virus strain SA-14-14-2[170], and dengue virus strain PUO-280[171] have a phenylalanine at this position. We therefore chose to make a leucine-to-phenylalanine mutant (L107F) in addition to substituting a polar residue (threonine) for Leu 107 (L107T) (Figure 2.1). Data for these two mutants in the virus suggest that replacement of Leu with hydrophilic amino acid, Thr, strongly impairs fusogenic activity, whereas a Phe mutant still retains a significant degree of fusogenic activity[108]. If the synthetic mutants also display similar activity changes, the synthetic peptides may then be considered to be a useful model fusion system.

Figure 2.1 Amino acid sequences of the target TBEV FPs: the 'WT' form has the same amino acid sequence as the corresponding segment in the native fusion protein from TBEV; the 'L107F' mutant; and the 'L107T' mutant. The numbering corresponds to the numbering in the intact fusion protein.

WT K^{93}RDQSDRGWGNHCG**L**$^{\mathbf{107}}$FGKGSI^{113}

L107F K^{93}RDQSDRGWGNHCG**F**$^{\mathbf{107}}$FGKGSI^{113}

L107T K^{93}RDQSDRGWGNHCG**T**$^{\mathbf{107}}$FGKGSI^{113}

2.2.3 Peptide synthesis

The chosen peptides were synthesized by SPPS. The fundamental premise of this technique involves the incorporation of amino acids into a peptide of any desired sequence with one end of the sequence remaining attached to a solid support matrix. While the peptide is being synthesized, usually by stepwise methods, all soluble reagents can be removed from the peptide-solid support matrix by filtration and washed away at the end of each coupling step. After the desired sequence of amino acids has been obtained, the peptide can be removed from the polymeric support.

The general scheme for SPPS is outlined in Figure 2.2. To begin each coupling, the amino protecting group on the resin bound peptide/amino acid is removed. It is then rinsed and a protected amino acid is added which has been activated at its α-carboxyl group. The activated amino acid and the resin bound amino acid are allowed to react in the presence of base to form a new peptide bond. This process is repeated until the desired peptide is assembled on the resin. Once the peptide is complete, the bond between the C-terminal amino acid and the resin is cleaved, which then affords the peptide in solution.

There are two approaches based on different N-α-amino acid protection groups: the butoxycarbonyl (Boc) group[167], and the 9H-fluoren-9-ylmethoxycarbonyl (Fmoc) group[172]. The Fmoc group is stable in acid but can be removed by base. In this approach any side-chain functional groups are protected with base stable, acid labile groups (Table

Figure 2.2 Schematic representation of the basic steps in SPPS. Each of the coupling steps starts with the deblocking of the amino protecting group. This deprotected peptide is then coupled with α-carboxyl activated amino acid. The coupling step is repeated until the target sequence is assembled. The peptide is obtained by cleaving it from the resin and simultaneously deprotecting the side-chain protecting groups.

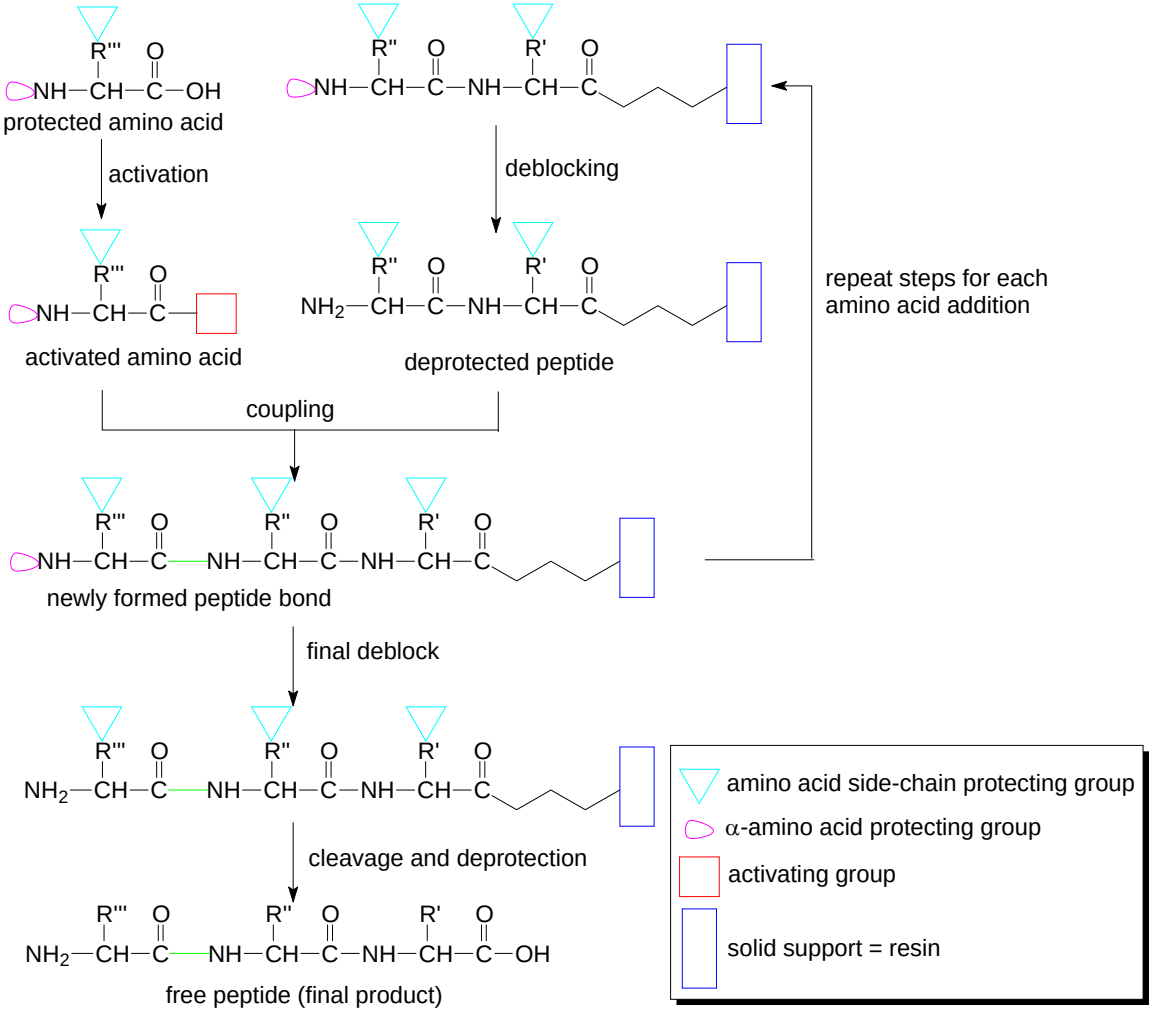

2.1), which are more easily removed than the side-chain protecting groups for Boc protected amino acids. Due to the ease of synthesis, we have therefore chosen to use Fmoc protected amino acids to synthesize the target peptides.

Table 2.1 Commonly used side-chain protecting groups for Fmoc amino acids.

Amino acid	Side-chain protecting group
Arg	2,2,5,7,8-pentamethylchroman-6-sulfonyl (Pmc)
Asp	tert-butyl ester (OtBu)
Asn	trityl (Trt)
Cys	trityl (Trt)
Glu	tert-butyl ester (OtBu)
Gln	trityl (Trt)
His	trityl (Trt)
Lys	butoxycarbonyl (Boc)
Ser	tert-butyl (tBu)
Thr	tert-butyl (tBu)
Tyr	tert-butyl (tBu)
Trp	butoxycarbonyl (Boc)

2.2.3.1 Initial synthesis

The WT peptide was firstly synthesized using the standard SPPS method. The synthetic peptide was characterized by matrix-assisted laser desorption/ionization (MALDI) mass spectrometry. However, the overall yield of purified peptide was low

(less than 5%). The elution profile (Figure 2.3) obtained from preparative reversed-phase high-performance liquid chromatography (HPLC) demonstrated that the crude product from the synthesis of WT peptide contained substantial amounts of impurities eluting very close to the product peak, at an elusion time of 25.8 min (red peak in Figure 2.3). The presence of multiple peptides eluting at the same time point would make purification difficult. Although there are ways around this problem, such as using longer HPLC gradients, we opted to optimize the peptide synthesis by identifying the cause for the impurities.

2.2.3.2 Optimization

MALDI-MS analysis of the synthetic WT FP crude product showed that the main constituent was a peptide with one Arg and one Lys or Gln missing (Figure 2.3). Because Lys and Gln have the same molecular mass, we cannot pinpoint which one was the missing residue. However, since the sequence contains two Arg residues, two Lys residues and one Gln residue, it was not possible to identify the position of the missing amino acid in the sequence. We therefore applied LC-MS/MS (i.e. daughter ion analysis of the byproduct peak in the LC-MS run) to find which two of the five possible residues (Lys 93, Arg 94, Gln 96, Arg 99, or Lys 110) were missing in the byproduct.

MS/MS is used to obtain structural information about a compound by fragmenting specific sample ions inside the mass spectrometer and identifying the resulting fragment

Figure 2.3 Preparative HPLC profiles of crude peptide, monitored at 229 nm. Crude WT peptide shows a large one-residue-missing byproduct peak A with an elution time of 27.0 min and a large two-residue-missing byproduct peak B with an elution time of 27.4 min. The peak of desired WT peptide, with the elusion time of 25.8 min, is also labeled in red in the elution profile. Other peaks containing impurity mixtures cannot be characterized by MALDI-MS.

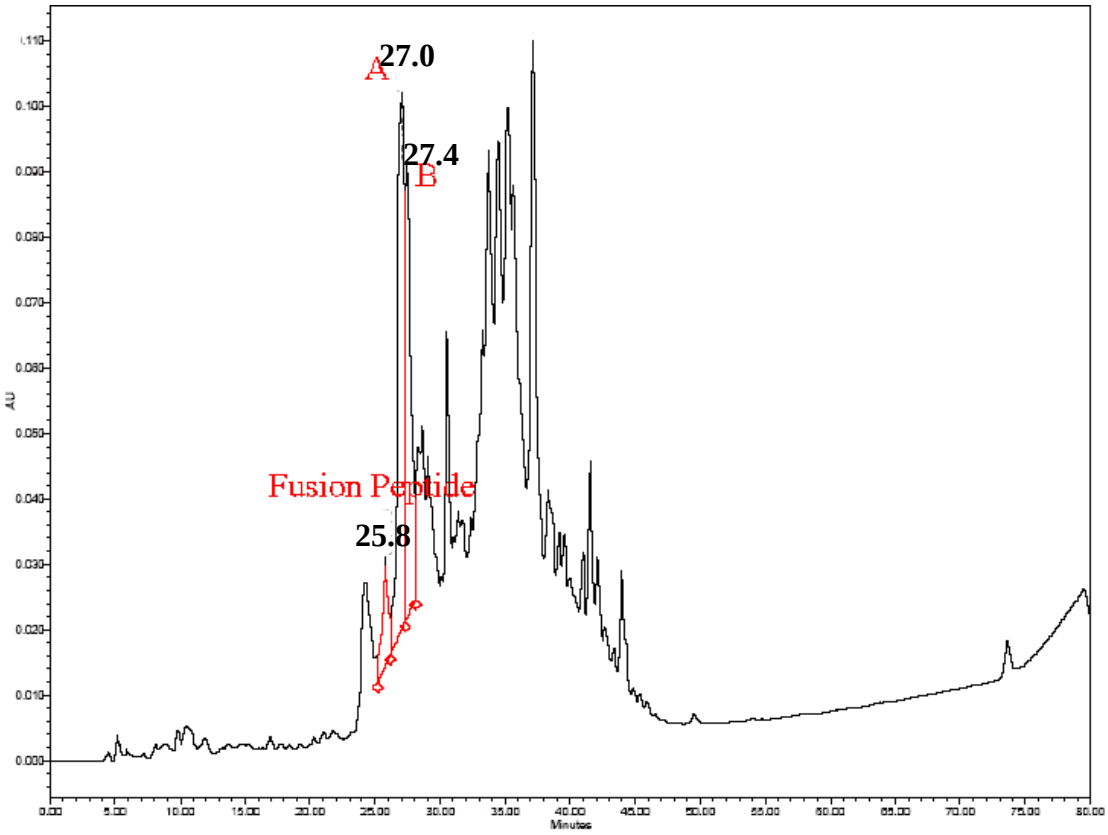

ions. A MS/MS spectrometer has more than one analyser, in practice usually two. The two analysers are separated by a collision cell into which an inert gas is admitted to collide with the selected sample ions and cause fragmentation. The most common usage of MS/MS in biochemical research is the product or daughter ion scanning experiment which is particularly useful for peptide and nucleotide sequencing. In this mode of data acquisition, the first analyser is used to select user-specified sample ions arising from a particular component, usually the molecular related ions, $M + H^+$. These chosen ions then

pass into the collision cell and are bombarded by the gas molecules which cause fragment ions to be formed. These latter fragment ions are analysed by the second analyser[173, 174]. There are three different types of bonds that can fragment along the amino acid backbone: the NH-CH, CH-CO, and CO-NH bonds. Each bond breakage gives rise to two species, one neutral and the other one charged, and only the charged species is detected. With the mass difference between adjacent members of a series, the peptide sequence can be elucidated.

Figure 2.4 shows the LC-MS/MS spectra of the byproduct in peak B from the HPLC trace in Figure 2.3. The sequence ions have been identified and the peptide was fragmented predominately at the CO-NH bonds. The mass difference between adjacent members of a series can be calculated. From right to left, the mass differences were 115.9, 128.3, 86.6, and 114.9 m/z, respectively, and correspond to the segment DQSD. These four residues correspond exactly to the residues 95-98 in the target peptide sequence (Figure 2.1). These data suggest that the two missing residues are Lys 93 and Arg 94. Subsequent systematic studies showed that double coupling of Lys 93 and Arg 94 was necessary to remedy this problem. In an optimized synthesis, the Lys 93 and Arg 94 residues were double-coupled, increasing the yield of desired peptide in each synthesis significantly. The synthesis of WT by this approach was shown to yield the desired product, in large quantities and in an easy to purify form (Figure 2.5). L107F and L107T were also synthesized using this approach. The HPLC profiles of the crude mutant peptides are shown in Figure 2.6. The overall yield of purified peptides was about 25%

Figure 2.4 Mass spectrometric daughter ion analysis. The two-residue-missing peak B from the HPLC trace is analyzed by LC-MS/MS. The data show that Lys 93 and Arg 94 in the target sequence are missing. The top spectrum shows MS/MS singly charged daughter ions obtained for peak B. The bottom spectrum shows an expanded region of the MS/MS spectrum, with singly charged daughter ions.

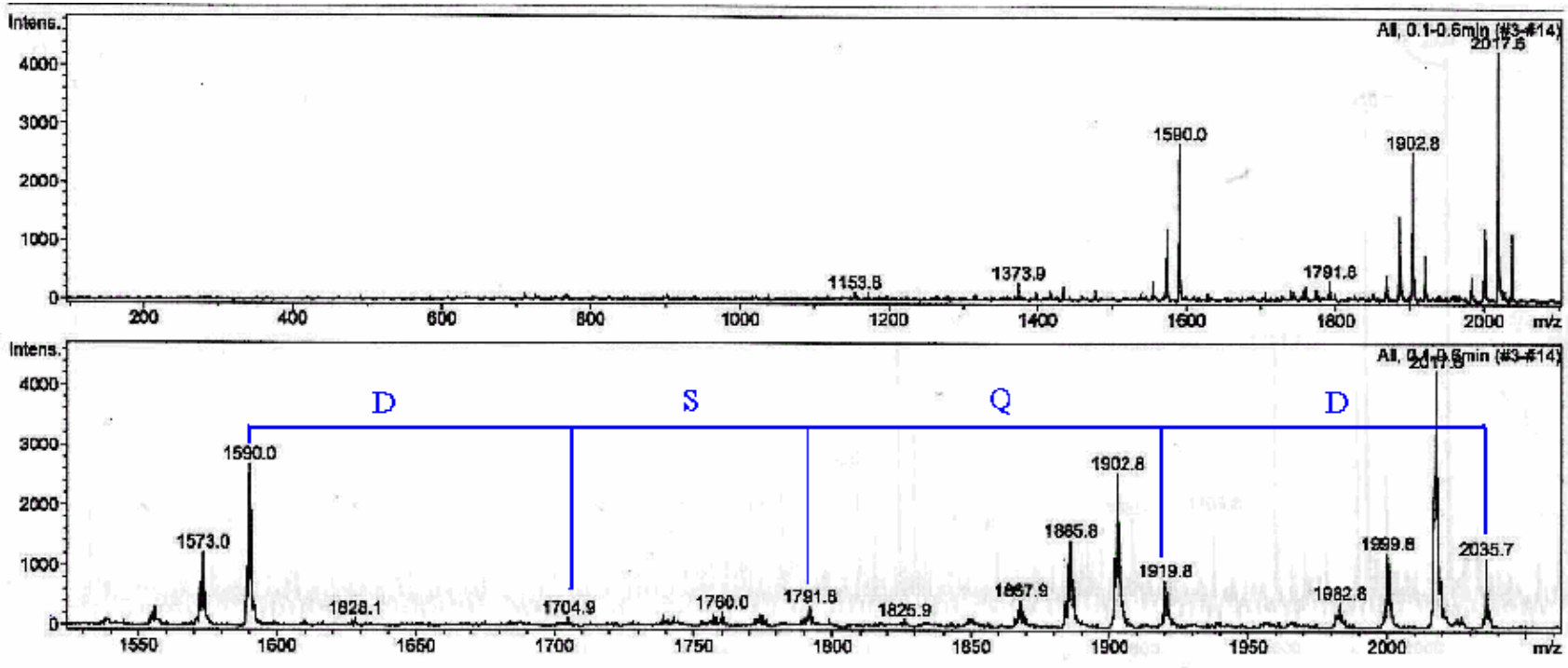

Figure 2.5 HPLC trace of crude WT peptide obtained after double coupling of the Lys 93 and Arg 94 shows no peak A or peak B, and the main peak belongs to the targeted WT peptide, which was characterized by MALDI mass spectrometry.

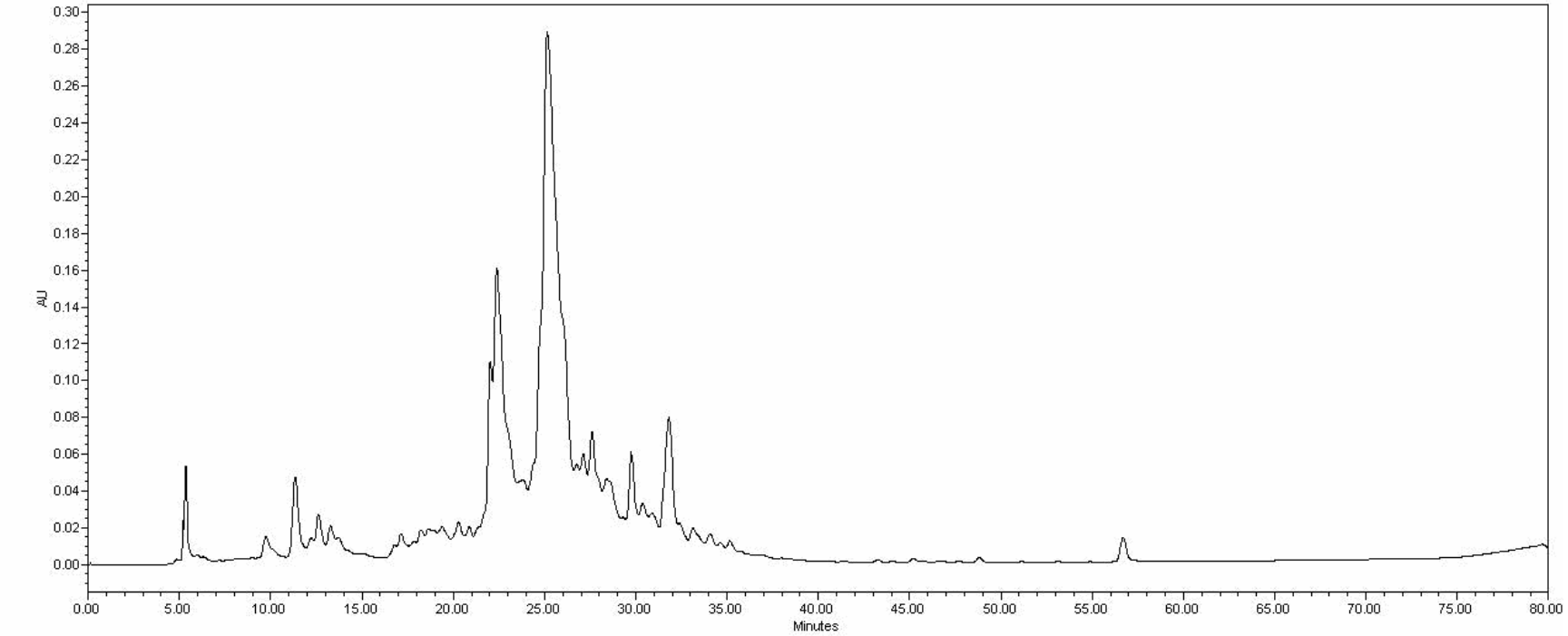

Figure 2.6 HPLC trace of crude L107F (a) and L107T (b) peptides obtained after double coupling of the Lys 93 and Arg 94. The main peak in the HPLC profile belongs to the targeted peptide, which was characterized by MALDI mass spectrometry.

(a)

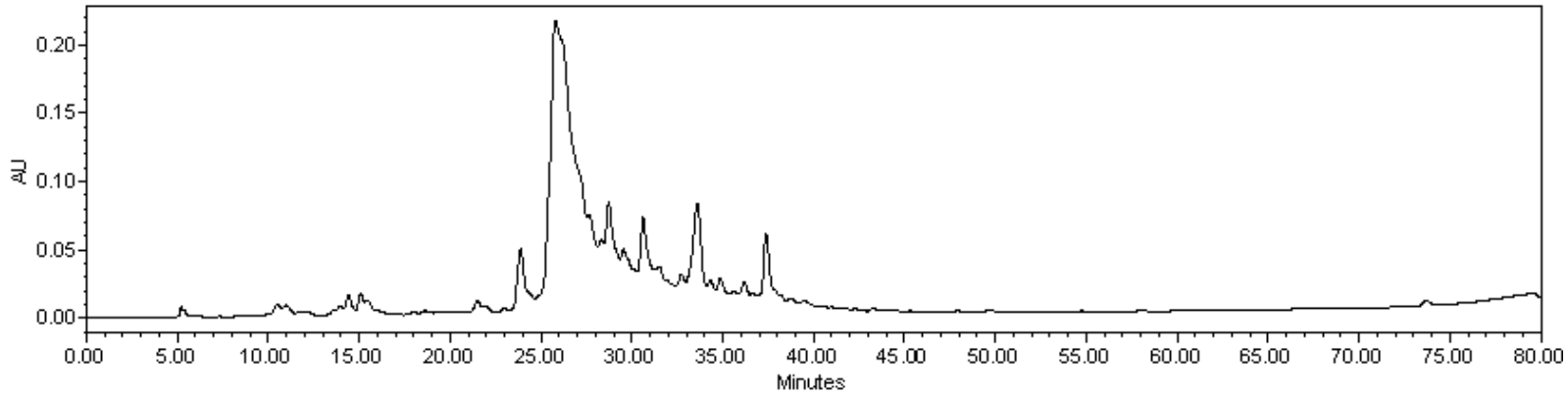

(b)

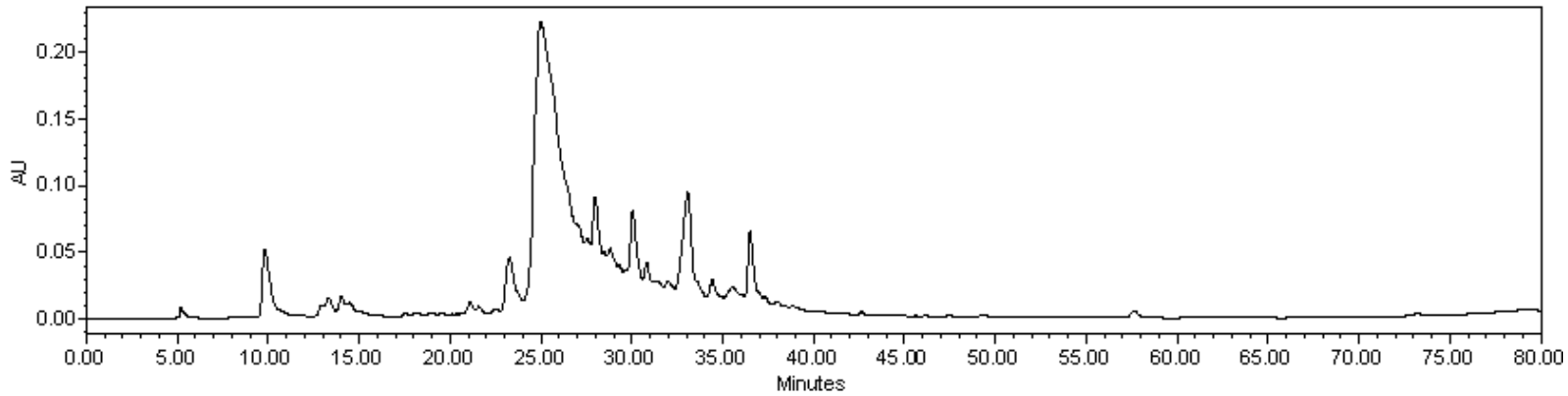

(~150 mg per synthesis).

2.2.4 Characterization of the synthetic peptides

The peptides were synthesized in good yield and with high levels of purity. Biophysical studies, which will be discussed below, were conducted to assess and compare the relative fusogenic activities and structures of WT, L107F, and L107T.

2.2.4.1 Far-UV CD spectroscopy

As introduced in Chapter 1, far-UV (195-250 nm) CD spectroscopy is used to quantify the extent of secondary structure present in peptides and proteins[20-22]. Figure 2.7 shows the CD curves observed for the synthetic peptides, WT, L107F, and L107T bound to liposomes consisting of 1-palmitoyl-2-oleoyl-*sn*-glycero-3-phosphocholine (POPC), 1-palmitoyl-2-oleoyl-*sn*-glycero-3-phosphoethanolamine (POPE), and cholesterol (Chol) at both neutral and acidic pH, as well as the WT peptide in aqueous solution or bound to cholesterol free vesicles. The secondary structure content was calculated using the programs CONTIN, SELCON3, and CDSSTR[175]. As shown in Table 2.2, the calculation of secondary structure for the synthetic peptides indicated the secondary structure of all three peptides is independent of pH. In all cases, the helical structure fraction was very small, 20–30% of the residues adopted β-strand structure, and more than 70% of the

Figure 2.7 Far-UV CD spectra for WT (a) in 20 mM phosphate buffer, (b) bound to POPC/POPE (molar ratio, 1:1) SUVs, or (c) bound to POPC/POPE/Chol (molar ratio, 1:1:1.5) SUVs. CD spectra for (d) L107F and (e) L107T bound to POPC/POPE/Chol (molar ratio, 1:1:1.5) SUVs. The spectra were recorded at neutral (pink) and acidic pH (dark blue).

(a) **(b)**

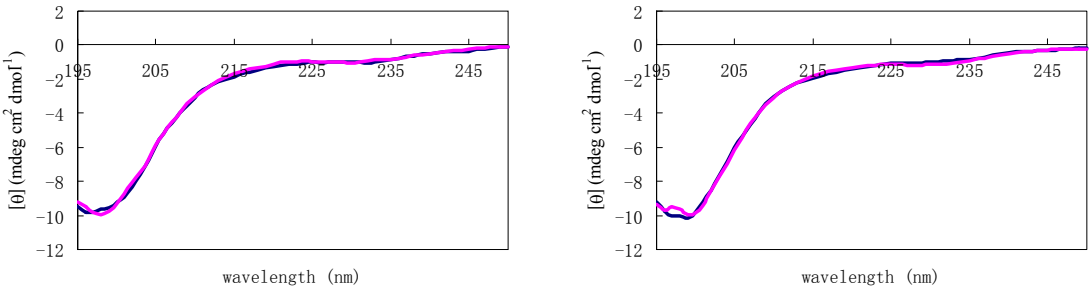

(c) **(d)**

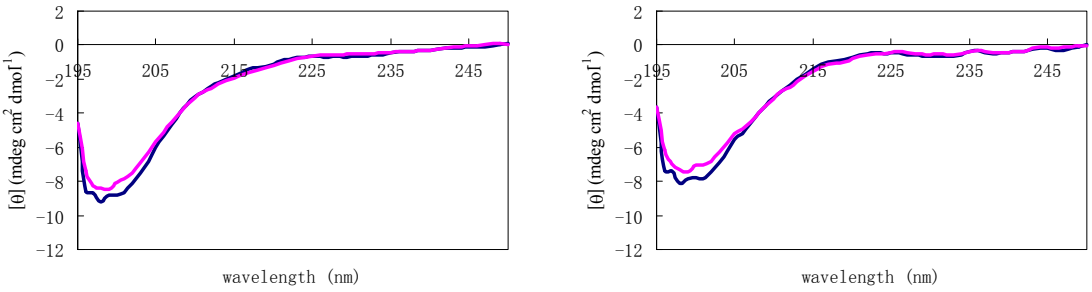

(e)

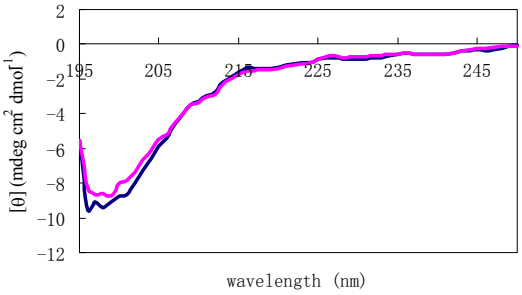

peptide sequence adopted turn or random coil structure. The amount of β-strand structures in the WT peptide was smaller than the analogous segment in the intact E protein. The mutation of Phe at position 107 did not cause any changes in secondary

Table 2.2 Secondary structure content of WT, L107F and L107T in various media and different pH, as extracted from the CD spectra. Spectra fit using CONTIN, SELCON3, and CDSSTR[175]. The error determined from the average of the calculated secondary structure content using the three programs.

			% Helix	% Strand	% Turn	% random coil
WT	**Phosphate buffer**	**pH 5.5**	6±3	24±4	26±3	44±4
		pH 7.5	6±2	24±1	26±5	45±3
	PC/PE (1:1)	**pH 5.5**	5±3	23±2	25±4	47±2
		pH 7.5	7±3	24±4	25±4	44±3
	PC/PE/Chol (1:1:1.5)	**pH 5.5**	7±3	33±3	25±2	34±4
		pH 7.5	7±4	33±2	25±1	35±3
L107F		**pH 5.5**	10±3	36±3	22±3	33±3
		pH 7.5	9±1	34±3	23±2	33±3
L107T		**pH 5.5**	15±6	24±3	26±3	35±4
		pH 7.5	11±2	25±3	24±4	40±1

structure, one of our aims in the peptide design. Interestingly, the presence of cholesterol in the liposomes increased the proportion of β-strand content from 23% to 33%. This increase translates into having two more residues which adopt β-strand structure when the WT peptide binds to cholesterol containing liposomes. The presence of cholesterol in a membrane is known to increase the lateral packing density and the conformational order of the lipid chains[176-181]. Because cholesterol imparts rigidity to a membrane bilayer,

it can therefore affect the structure of a membrane-associated peptide. Indeed, it has been shown that for membranes which have the approximate lipid headgroup and cholesterol composition of host cells, the HIV FP adopts an uninterrupted β-strand conformation[16], while for membranes without cholesterol, a significant fraction of the HIV FP adopts a helical structure[98]. It should be noted, however, that direct interactions between a FP and cholesterol are possible and that this may also contribute of the observed conformational changes[15, 182].

2.2.4.2 Tryptophan fluorescence spectroscopy

The locations of the peptides in lipid bilayers were determined by monitoring the fluorescence spectroscopy of residue Trp 101. When excited at 280 nm, the Trp101 residue in the synthetic peptides gives rise to an emission peak detected at 357nm. When WT and L107F were bound to LUVs consisting of POPC/POPE/Chol, the more hydrophobic environment and the decreased flexibility of the Trp residue in the membrane caused an increase in the fluorescence intensity (Figure 2.8.a, 2.8.b and 2.8.d). The intensity increase could also be observed when WT was bound to POPC/POPE LUVs, but the increase was smaller. There results indicated that the Trp side chain of WT and L107F was positioned in a more hydrophobic environment and was more sterically confined in POPC/POPE/Chol LUVs and POPC/POPE LUVs. In the crystal structure of the E protein from TBEV, the Trp 101 residue is located at the tip of the *cd* loop[106].

Figure 2.8 Fluorescence emission spectra of (a) WT, (b) L107F, and (c) L107T in 20 mM HEPES buffer at pH 5.5 (dark blue), and incubated with POPC/POPE/Chol (molar ratio, 1:1:1.5) (pink) or POPC/POPE (molar ratio, 1:1) (red) LUVs with peptide-to-lipid ratios of 1:100. (d) Fluorescence emission spectra of WT in 20 mM HEPES buffer at pH 7.5 (dark blue), and incubated with POPC/POPE/Chol (molar ratio, 1:1:1.5) LUVs with peptide-to-lipid ratios of 1:100 (pink).

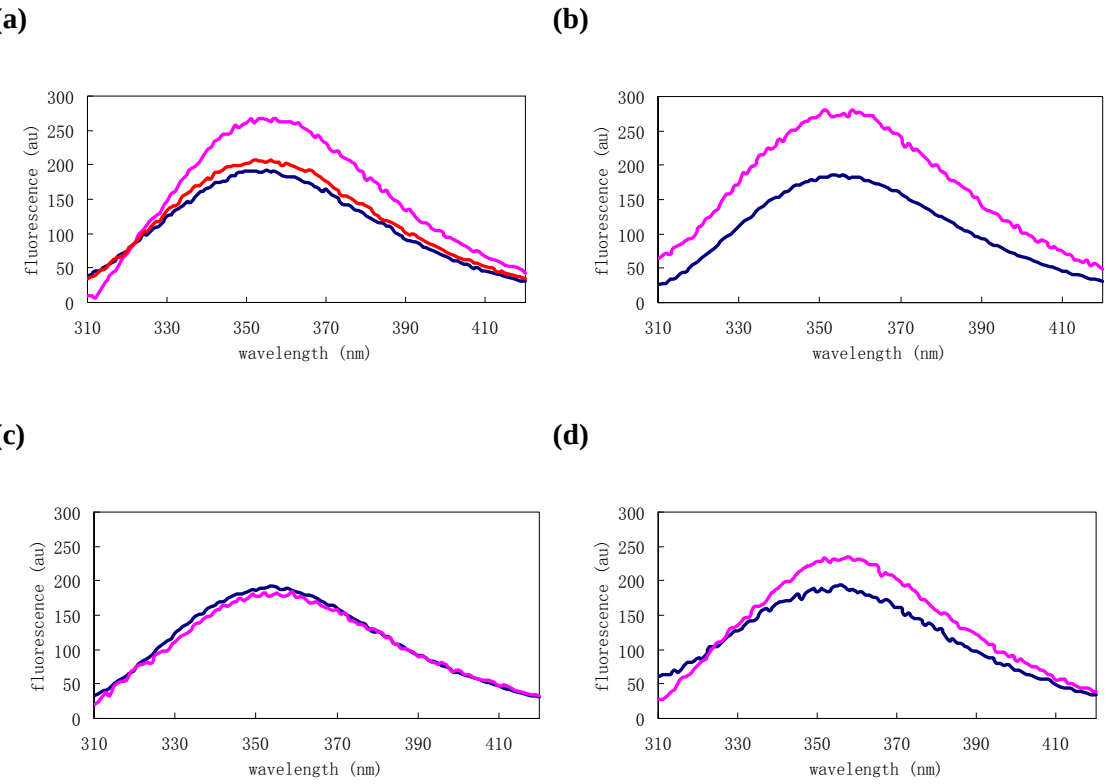

Therefore, the enhancement of Trp emission intensity can be interpreted as the WT and L107F having penetrated into the hydrophobic core of the bilayers. By contrast, the Trp emission intensity did not significantly increase when L107T was bound to POPC/POPE/Chol LUVs (Figure 2.8.c), indicating that the Trp 101 residue in L107T did not penetrate as deeply into the membrane as in the WT or L107F sample. This finding can be rationalized in terms of a Leu 107 mutation to Thr resulting in a less hydrophobic peptide which is less likely to partition into a hydrophobic membrane bilayer. These data

have provided functional evidence that the highly conserved loop at the tip of each subunit of the flavivirus E protein may be directly involved in interactions with target membranes during the initial stages of membrane fusion. Previous studies on the mutant E protein indicated that the mutation of L107F has similar fusogenic activity to WT E protein, whereas the mutation of L107T strongly impairs the membrane fusion. The localization of peptide into the lipid bilayer might therefore correlate with the fusogenic activity. The shallow insertion of L107T might be a cause of the decrease in membrane fusion. It is interesting to note that the increase of Trp emission intensity was larger when WT was bound to POPC/POPE/Chol LUVs than when it was bound to POPC/POPE LUVs, which also indicated that WT penetrated deeper into POPC/POPE/Chol bilayers than into POPC/POPE bilayers. This effect suggested that the presence of cholesterol in the membrane, which has been known to increase the lateral packing density and higher conformational order for the lipid chains[176-181], might influence the insertion of FPs into membranes. The studies on SFV[133] and SIN[134] also indicated that cholesterol appears to be primarily involved in the binding of the virus to the liposomes. Finally, the changes in pH seemed not to affect the peptide insertion significantly.

2.2.4.3 Fluorescence resonance energy transfer assay

The fusogenic activity of the synthetic FPs was determined by a fluorescence resonance energy transfer (FRET) assay. FRET is a distance-dependent interaction

between the electronic excited states of two dye molecules in which excitation is transferred from a donor molecule to an acceptor molecule without emission of a photon. The efficiency of FRET is dependent on the inverse sixth power of the intermolecular separation[183], making it applicable over distances comparable with the dimensions of biological macromolecules. Thus, FRET is an important technique for investigating a variety of biological phenomena that produce changes in molecular proximity[183-191]. FRET can take place when donor and acceptor molecules are in close proximity (typically 10-100 Å) and if the absorption spectrum of the acceptor overlaps with the fluorescence emission spectrum of the donor (Figure 2.9.a). Finally, FRET occurs when donor and acceptor transition dipole orientations are approximately parallel.

FRET can be used to monitor membrane fusion. One typical method is based on NBD – rhodamine energy transfer[192] (Figure 2.9.b), in which membranes labeled with a combination of FRET donor and acceptor lipid probes, typically *N*-(7-nitro-2,1,3-benzoxadiazol-4-yl)phosphatidylethanolamine (NBD-PE) and *N*-(lissamine Rhodamine B sulfonyl)phosphatidylethanolamine (Rh-PE), respectively, are mixed with unlabeled ones. FRET detected as rhodamine emission at ~585 nm resulting from NBD excitation at ~470 nm, decreases when the average spatial separation of the probes is increased upon fusion of labeled membranes with unlabeled ones. At both prefusion and postfusion stages, the NBD-PE and Rh-PE are homogeneously distributed in the labeled lipid vesicles. The reverse detection scheme, in which FRET increases upon fusion of membranes that have been separately labeled with donor and acceptor

Figure 2.9 (a) Schematic representation of the FRET spectral overlap integral[193]. (b) Illustration representing a membrane fusion assay based on FRET. The average spatial separation of the donor (D) and acceptor (A) lipid probes that are homogeneously distributed, increases upon fusion of labeled membranes with unlabeled membranes, resulting in decreased efficiency of proximity-dependent FRET (represented by blue arrows). Decreased FRET efficiency is recorded by increased donor fluorescence intensity and decreased acceptor fluorescence intensity.

(a)

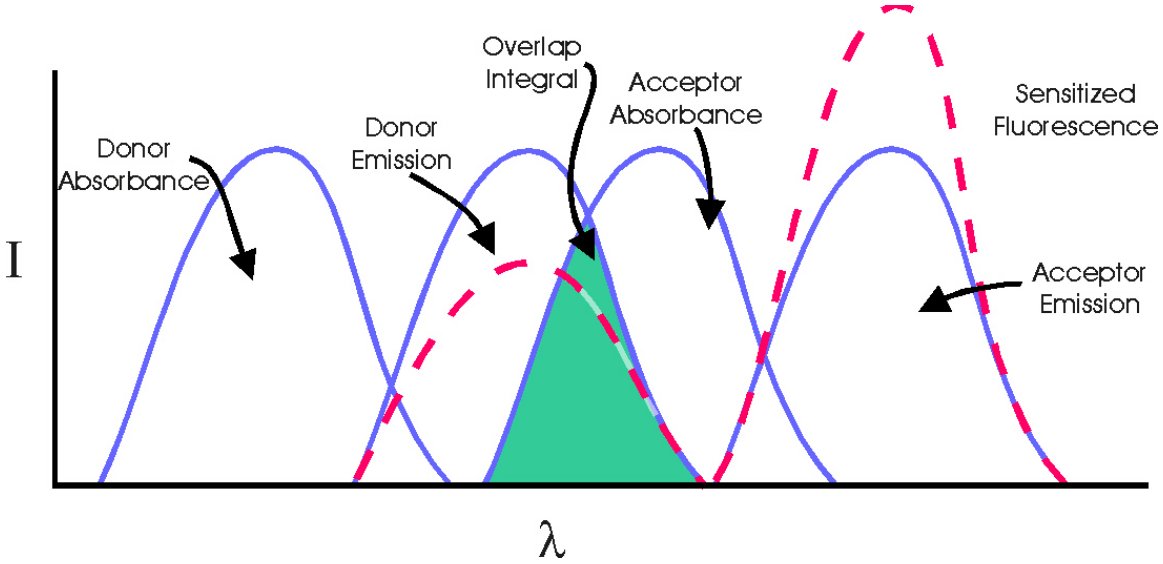

(b)

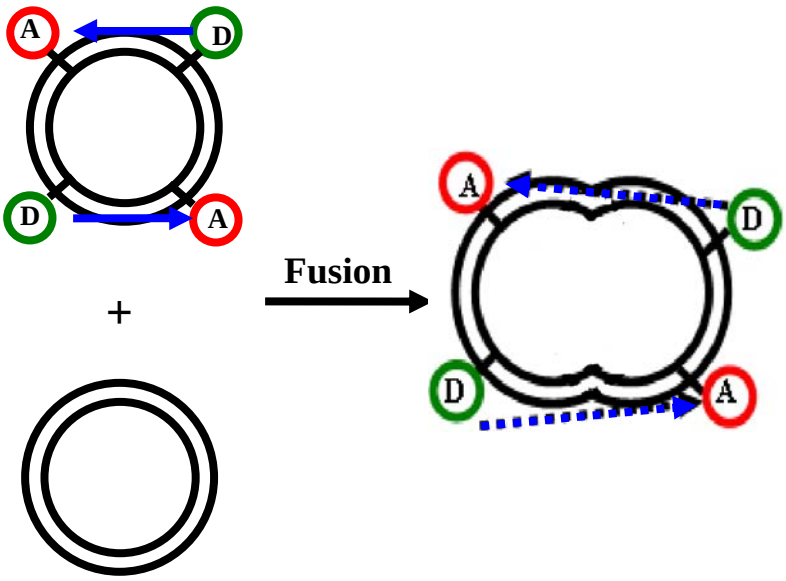

probes, has also proven to be a useful membrane fusion assay[194].

The synthetic WT peptide was tested for its ability to undergo fusion with artificial membranes (unilamellar liposomes with an average diameter of 100 nm, composed of POPC, POPE and Chol, at a molar ratio of 1:1:1.5). The fusogenic activity was determined by the change in fluorescence of the sample:

$$\% \text{ fusion} = [(F(t) - F_0)/(F_{max} - F_0)] \times 100 \quad (2.1)$$

where F(t) is the fluorescence intensity as a function of time t, F_0 is the initial fluorescence intensity, and F_{max} is the maximum fluorescence intensity obtained by adding 20 μL of 10% Triton X-100. As shown in Figure 2.10.a, rapid fusion of the synthetic WT peptide with liposomes was observed when a peptide-liposome mixture was acidified to pH 5.5 at 37 ℃. Under these conditions, the fluorescence changed by about 40% within the first 15 s. This implied that within 15 s at least 40% of the liposomes labeled by NBD-PE and Rh-PE had fused at least once with an unlabeled liposome. No fusion was observed when the experiment was carried out at pH 7.5, consistent with earlier reports that E protein from TBEV requires an acidic pH for fusion[109, 110, 112]. However, compared with fusion induced by pyrene-labeled TBEV virus[110], the fusogenic activity of the synthetic peptide was weaker and the fusion rate was slower. A possible explanation for this difference in activity may be that the oligomerization state and the interactions between FP and other compartments of the E protein (in the intact protein) might enhance the fusogenic activity of the FP segment.

The ability of the L107F and L107T mutants to fuse membranes was also

Figure 2.10 (a) Extent of fusion of synthetic WT peptide with liposomes consisting of POPC/POPE/Chol (molar ratio, 1:1:1.5) at pH 5.5 (dark blue) and pH 7.5 (pink). (b) low-pH-induced fusion of WT (dark blue), L107F (pink), and L107T (red) with liposomes consisting of POPC/POPE/Chol (molar ratio, 1:1:1.5). The zero represents the time of acidification for the curves at pH 5.5. The zero was set arbitrarily for the data at pH 7.5.

(a)

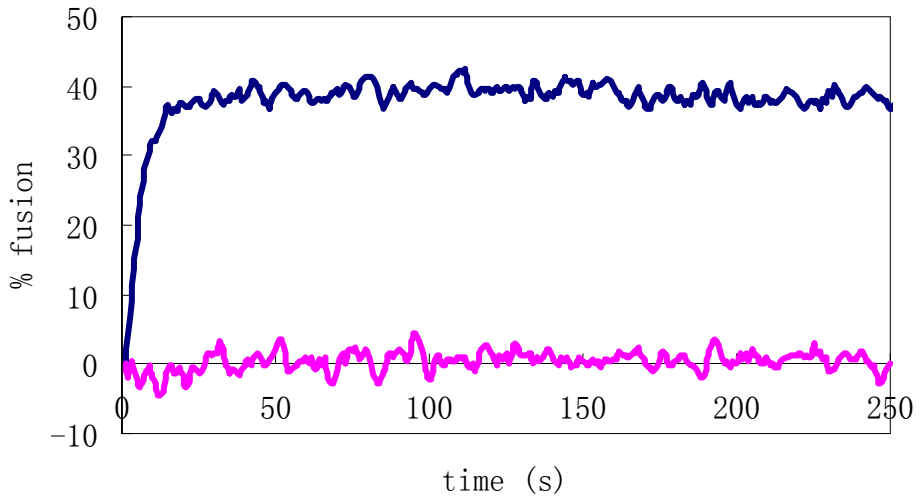

(b)

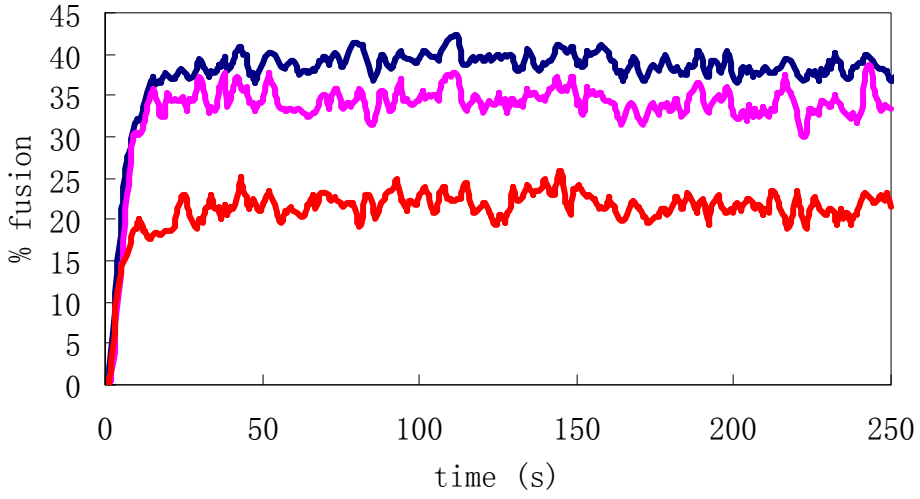

investigated. Figure 2.10.b shows that L107F also fused with liposomes at low pH, and both the initial rate and final extent of fusion were similar to WT. The Thr mutant, L107T, on the other hand, retained only a low level of fusion activity. These results corresponded to the mutational studies on the intact E protein from TBEV[108]. The data presented here provide further functional evidence that mutation in the highly conserved FP segment of the fusion protein leads to loss of activity. Therefore, the fusogenic loop at the tip of each subunit of the flavivirus is important for fusogenic activity. In addition, the notion that this portion of the protein serves as an internal FP is consistent with previous observations that antibodies, recognizing the region from residue 98 to 110, are capable of blocking low-pH-induced fusion of TBEV with artificial membranes[195] and react more strongly with the low-pH form of the dengue 2 virus E protein, in which the Leu is changed to Phe at 107 position, than with the native neutral form[196]. All of these data suggest that the *cd* loop itself might insert into the target membrane during fusion and might be the key contributing factor at the initial stages of membrane fusion.

2.2.4.4 Photon correlation spectroscopy

Another method to study the membrane fusion induced by FPs is to use photon correlation spectroscopy to determine the diameter of vesicles in a dispersion[197]. Since membrane fusion causes aggregation of the lipid vesicles, resulting in an increase in their diameter, the fusogenic activity of FPs can be determined by monitoring the size changes

of lipid vesicles. In this method, the particle size is determined by measuring the rate of diffusion of particles through a fluid. The rate of diffusion depends on three factors: temperature of the fluid, viscosity of the fluid, and particle size. If the temperature and viscosity are known, the particle size can be determined.

2.2.4.4.1 Theory behind particle size determination

The motion caused by thermal agitation, that is, the random collision of particles in solution with solvent molecules, is called Brownian motion. These collisions result in random movement that causes suspended particles to diffuse through the solution. For a solution of given viscosity, at a constant temperature, the rate of diffusion or diffusion coefficient (D) is inversely related to the particle size according to the Stokes-Einstein equation:

$$D = \frac{k_B T}{3\pi\eta d} \tag{2.2}$$

where k_B is the Boltzmann constant, T is temperature, η is the viscosity, and d is averaged spherical diameter of particles. Information concerning the size of particles in solution is obtained by measuring the diffusion coefficients of such particles.

Particles undergoing Brownian motion are detected and analyzed by illuminating the particles with a laser and measuring the scattered light. The light scattered by the particles at any given instant adds together to form an interference pattern. The intensity

of the scattered light depends on this interference pattern which in turn depends on the pattern of particles in the laser beam. As the particles move randomly through the solution, their positions relative to one another change, causing a constantly changing interference pattern and varying light intensity at the detector.

In order to calculate the diffusion coefficient, and therefore the particle size from the changing light intensity signal, the signal must be mathematically transformed. The result of this transformation is called the autocorrelation function $G(\tau)$. This function is defined as:

$$G(\tau) = \langle I(t) \times I(t + \tau) \rangle \quad (2.3)$$

where $I(t)$ is the intensity detected at time t, $I(t + \tau)$ is the intensity detected at time $t + \tau$, τ is the delay time, and $\langle \rangle$ represents a time average. If the molecules or particles in solution are the same size and shape, $G(\tau)$ is a single exponential decay:

$$G(\tau) \propto \exp^{-2\Gamma\tau} \quad (2.4)$$

The decay constant of the exponential is Γ, which is defined as:

$$\Gamma = DK^2 \quad (2.5)$$

where D is the diffusion coefficient and:

$$K = (4\pi n / \lambda) \sin (\theta / 2) \quad (2.6)$$

where n is refractive index of the solution, λ is the wavelength of the laser light used, and θ is the angle at which the scattering intensity is measured.

2.2.4.4.2 Determination of fusogenic activity induced by synthetic peptides

The fusogenic activity of the synthetic peptides was determined by measuring the change in diameter of the lipid vesicles. At first, we attempted to examine the possible size variation of lipid vesicles as a function of pH and time. It is known that phosphatidylcholine (PC) vesicles in their liquid crystalline phase are well separated and fuse very slowly[198, 199]. This relative stability can be attributed, at least partly, to the layer of bound water on the surface of vesicles, which inhibits close approach of vesicles and presents a thermodynamic barrier that impedes transfer of apolar groups to the aqueous phase[200]. Though the liposomes we investigated were a mixture of POPC, POPE, and cholesterol (i.e. not only POPC), a negligible change in the diameter of these vesicles was still observed over a period of several hours. Only negligible diameter changes were observed in the pH range of 3.5-7.5 in the absence of FP (Figure 2.11). Thus it serves as an appropriate control for studying the fusion over a greater pH range.

In order to gain insight into the nature of fusion, the FP-induced aggregation of dispersions of vesicles was monitored by photon correlation spectroscopy. The vesicles were incubated with the peptides for half an hour, a time which was found sufficient to achieve maximum fusion. As demonstrated in Figure 2.12.a, a significant increase in the vesicle diameter induced by the synthetic FPs was observed at acidic pH. The increase in the measured particle diameter reflected that the merger of vesicles was indeed induced by the peptide used, and not merely the result of a clustering of vesicles at fusogenic pH.

Figure 2.11 Effect of pH on the average size of vesicles prepared in the absence of FPs. The liposomes consisted of POPC/POPE/Chol with a molar ratio of 1:1:1.5, and the concentration of liposomes was kept at 26 μM.

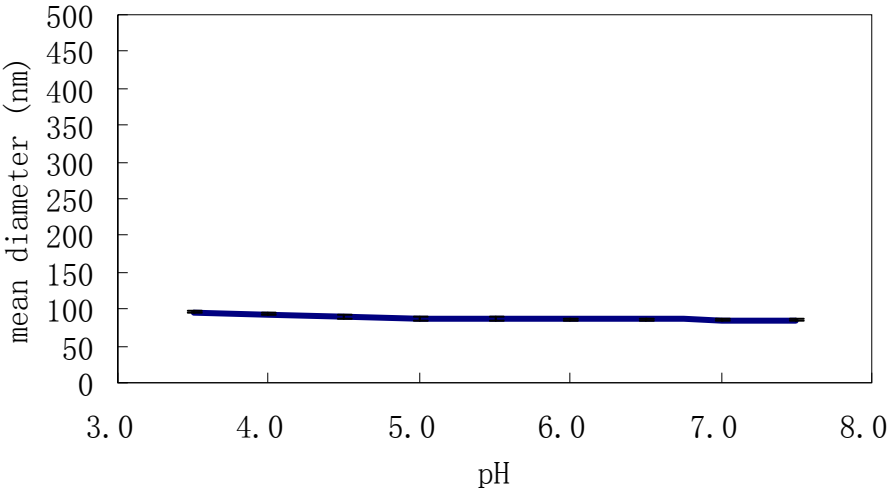

However, the size of the vesicles increased as the pH decreased when synthetic peptides were present. At pH 5.5, which is the optimum fusion pH of intact E protein[110], the diameter of these vesicles with WT, L107F, or L107T, became 1.7, 1.6, or 1.2 times the size of vesicles at neutral pH, respectively. These results indicated that replacement of the Leu 107 residue with hydrophilic amino acid (Thr) strongly impaired fusogenic activity, whereas the Phe mutant still retained a significant degree of fusogenic activity, consistent with the data obtained from FRET experiments. In addition, the pH dependence exhibited a threshold below pH 7.0 for both WT and L107F peptides, because the ratio of the vesicle size at pH 7.0 to the size at pH 7.5 was 1.0 for both peptides, whereas the ratio of the vesicle size at pH 6.5 to the size at pH 7.5 became 1.2. A similar observation was made for the fusion induced by intact E protein from TBEV[110]. Furthermore, a pH

Figure 2.12 (a) pH dependence in the average size of vesicles induced by WT (dark blue), L107F (pink), and L107T (red). The data are an average of two independent measurements. The lipid concentration was 26 μM and peptide-to-lipid ratios were 1:1. (b) Effect of the liposomal lipid composition on fusion of WT peptide with liposomes. Dark blue curve, POPC/POPE/Chol (molar ratio, 1:1:1.5); pink curve, POPC/POPE/Chol (molar ratio, 1:1:1); red curve, POPC/POPE/Chol (molar ratio, 1:1:0.5); and black curve, POPC/POPE (molar ratio 1:1).

(a)

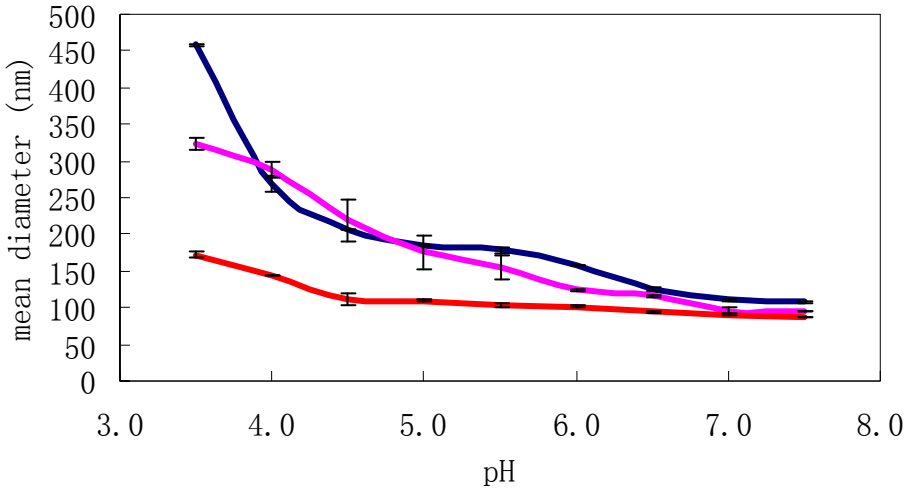

(b)

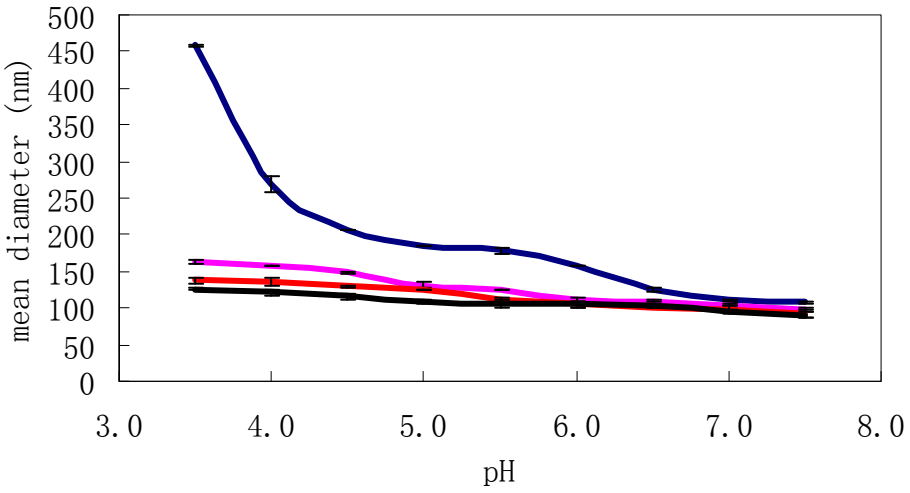

threshold of pH 6.7 has been reported for fusion in West Nile virus, another flavivirus[201]. The pH threshold is relatively high compared with that for fusion of alphaviruses, such as SFV[202] or SIN[134]. Also, the pH threshold for fusion of influenza virus, is generally lower than the threshold observed here, although it varies somewhat between virus strains[203-205]. The comparatively high pH threshold for fusion implies that flaviviruses may fuse within early endosomes[206]. However, there is no evidence to show a direct correlation between the high pH threshold for fusion and the membrane fusion rate induced by enveloped viruses.

Some viruses have a specific requirement for particular lipids in the target membrane. For example, SFV and SIN require the presence of cholesterol for membrane fusion to take place[129, 131-134]. To determine whether TBEV also has a specific lipid requirement, we measured the fusion of WT peptide with liposomes of several different compositions. As shown in Figure 2.12.b, the diameter of lipid vesicles with WT peptide increased as the pH decreased. At pH 5.5, the vesicle size of liposomes consisting of POPC/POPE/Chol (1:1:1.5), POPC/POPE/Chol (1:1:1), POPC/POPE/Chol (1:1:0.5), or POPC/POPE (1:1) became 1.7, 1.3, 1.2 or 1.2 times larger than liposomes at neutral pH. These results indicated that the inclusion of cholesterol in the target membrane, although not absolutely essential, appears to facilitate fusion by the FP of TBEV. Similar results have been reported for the fusion induced by the synthetic HIV FP[105]. Cholesterol appears to be primarily involved in the low-pH binding of the virus to the liposomes[133, 134], as discussed in Section 2.2.4.2. It may be speculated that the decrease in TBEV FP

fusion seen with cholesterol free liposomes is due to a lower extent of peptide-liposome binding.

2.3 Summary and conclusions

This chapter presented the design, synthesis and characterization of the three independent FPs from TBEV, namely WT, L107F, and L107T. The aim was to design viable model systems for the fusion in E protein from TBEV. The peptide sequences were designed and synthesized after optimization and obtained in reasonable yields. In order to test their validity as models, we (1) examined their secondary structures; (2) characterized the binding of the peptides to membranes; and (3) determined their fusogenic activities.

We found that for all of the three synthetic peptides, most of their structures were turn or random coil. The acidic pH in the solution seemed not to affect the secondary structure of the peptides. The presence of cholesterol in the membrane resulted in a slight increase in the fraction of β-strand conformation in the WT peptides, which might explain the effect of cholesterol on the peptide insertion and the fusogenic activity induced by FPs.

The WT and L107F FPs can insert into the hydrophobic core of lipid bilayers, whereas the polar substitution of Thr at position 107 strongly impairs the binding of L107T with liposomes. Furthermore, the inclusion of cholesterol in the target membrane

had an important impact on the insertion of the WT peptide into the target membrane at acidic pH.

Membrane fusogenic activity was monitored using a FRET assay and photon correlation spectroscopy. The fusion induced by the FP is strictly dependent on low pH with a threshold at pH 6.5-7.0. At pH 5.5 and 37 ℃, the rate and extent of fusion induced by WT peptide were high, with more than 40% of membranes fusing within 15 s. The replacement of Leu 107 in WT with hydrophilic amino acid (Thr) weakened the fusogenic activity, whereas the Phe mutant, L107F, still retained a significant degree of fusogenic activity. These results indicated that the synthetic WT peptide can serve as a fusion system in itself and open an opportunity to gain insight into the fusion mechanism of the E protein from TBEV. In addition, the study of fusion in various liposome compositions demonstrated that the presence of cholesterol appeared to facilitate fusion by the TBEV FP, though it is not essential for the membrane fusion to proceed.

2.4 Experimental

2.4.1 Materials

Fmoc-protected amino acids, Wang resin, and 2-(1*H*-benzotriazol-1-yl)-1,1,3,3-tetramethyluronium hexafluorophosphate (HBTU) were

obtained from Advanced Chemtech. *N*-Hydroxybenzotriazole (HOBT) was obtained from Novabiochem. *N*,*N*-Dimethylformamide (DMF), dichloromethane (DCM), and acetonitrile were purchased from Fisher. *N*,*N*-diiopropylethylamine (DIEA), trifluoroacetic aicd (TFA), thioanisole, phenol, ethane dithiol (EDT), triethylsilane (TES), and 4-(2-hydroxyethyl)-1-piperazineethanesulfonic acid (HEPES) were purchased from Sigma-Aldrich. Dithiothreitol (DTT) was purchased from Invitrogen. POPC, POPE, NBD-PE, and Rh-PE were used as supplied from Avanti Polar Lipids. No purification was carried out for the experimental materials.

2.4.2 Peptide synthesis

To couple the first residue onto the Wang resin, Fmoc-Ile (1 mmol) was preactivated for 3 min with 1 mmol of HBTU and HOBT (0.5 M in DMF) in the presence of 2 mmol DIEA and coupled for overnight to 0.25 mmol Wang resin. Next, prepared Ile-Wang resin was loaded onto an Applied Biosystems 431A peptide synthesizer to synthesize the target peptides by the in situ neutralization Fmoc chemistry[35]. Side-chain protection for amino-acids was as follows: Arg(Pmc), Asn(Trt), Asp(OtBu), Cys(Trt), Gln(Trt), His(Trt), Lys(Boc), Ser(tBu), Trp(Boc). For double coupling of Lys 93 and Arg 94, one additional coupling step was performed with only DMF washes intervening in the middle of two coupling steps for each amino acid. After chain assembly was complete, the peptide was deprotected and simultaneously cleaved from the resin using the cleavage mixture: 81.5%

TFA, 5% thioanisole, 5% phenol, 5% ddH2O, 2.5% EDT, and 1% TES, for 5 hr. After evaporation of the TFA under reduced pressure, crude products were precipitated and triturated with chilled diethyl ether, and the peptide products were dissolved in water and then were lyophilized. Crude peptide solid was dissolved in 0.1% TFA aqueous solution and injected into the preparative HPLC system. Purified peptide was lyophilized, to yield a fluffy white solid peptide. The peptide showed a single peak by analytical reversed-phase HPLC (> 95% pure), and had the expected molecular mass by characterized using MALDI-MS (Table 2.3).

Table 2.3 Percent yield and MALDI-MS characterization of the synthetic peptides.

Peptide	% Yield	Cal. Mass (Da.)	Obs. Mass (Da.)
WT	**28**	**2318.5**	**2318.7**
L107F	**26**	**2352.5**	**2352.8**
L107T	**25**	**2306**	**2306.4**

2.4.3 HPLC

Synthetic peptides were purified by preparative gradient RP-HPLC on a Waters 600 system with Waters 2996 Photodiode Array Detector with 229 nm UV detection using a Phenomenex C4 column (20 μm, 2.1 × 25 cm) at a flow rate of 10 mL/min, with a

gradient of 0 to 50% buffer B (10% dd water, 90% acetonitrile containing 0.1% TFA) in buffer A (90% dd water, 10% acetonitrile containing 0.1% TFA) over 60 min.

2.4.4 Vesicle preparation

SUVs were prepared by sonicating lipids in 20 mM phosphate buffer for 3 hours. LUVs were prepared by the extrusion method using a small-volume extrusion apparatus[52]. After a final trace amount of organic solvent was evaporated, the dried lipid film was suspended in 20 mM HEPES buffer. After 5 freezing and thawing cycles, the lipid suspensions were extruded by using an extruder 10 times through two stacked 0.l-μm-pore-size polycarbonate filters.

2.4.5 CD spectroscopy

CD spectra were measured using a Jasco J-710 spectropolarimeter. Spectra were recorded from 250 to 195 nm at a sensitivity of 5 millidegrees, resolution of 1 nm, response of 1 s, bandwidth of 1.0 nm, and a scan speed of 20 nm/min with 3 accumulations in order to increase the signal-to-noise ratio. The peptide concentration in 20 mM phosphate buffer was 50 μM. In order to prevent the intermolecular oxidation of the Cys residue, DTT was added in the solution with a molar ratio of DTT to peptide of 10:1[207]. Phospholipid concentrations of SUVs were 1 mM.

2.4.6 Tryptophan fluorescence spectroscopy

In this assay, the peptide-lipid mixtures were incubated at room temperature for 1 hr before data acquisition. Peptides at 1 μM concentration and DTT at 10 μM concentration were in 20 mM HEPES buffer. The total phospholipid concentration was 100 μM and the LUVs were prepared using the appropriate lipid composition. Corrected Trp emission spectra were acquired at 37 ℃ on a Varian Eclipse Fluorescence Spectrophotometer. Excitation of the indole ring was set at 280 nm.

2.4.7 FRET assay

Measurements were conducted at 37 ℃ using thermostated cuvettes with constant stirring, on a Varian Eclipse Fluorescence Spectrophotometer. The assay is based on the dilution of NBD-PE and Ph-PE. The dilution due to membrane lipid fusion results in a decrease in Rh-PE fluorescence. LUVs consist of POPC, POPE, and cholesterol (molar ratio, 1:1:1.5). LUVs containing 1 mol % of each probe were mixed with unlabeled LUVs at a 1:9 ratio with 100 μM total lipid in 2 ml 20 mM HEPES buffer at pH 7.5. The Rh-PE emission was monitored at 590 nm, with the excitation wavelength set at 465 nm. The fluorescence scale was calibrated such that the zero level corresponded to the initial residual fluorescence of the labeled vesicles and the 100% value to the fluorescence after addition of 20 μl of 10% (vol/vol) Triton X-100. Synthetic peptides at 5 μM

concentration were added in 20 mM HEPES buffer with 50 μM DTT. The pH was adjusted by adding the appropriate volume of a 1 mM HCl solution.

2.4.8 Photon correlation spectroscopy

Measurements were carried out on a Beckman Coulter N4plus photon-correlation spectrometer using 600 nm laser at 90^{o}[197]. The liposomes (total phospholipids, 26 μM) were in 20 mM HEPES buffer (pH 7.5) in the presence of 260 μM DTT. Synthetic peptides were added into the liposome solution to reach a final concentration of 26 μM. The vesicle sizes were measured after the liposome sample was incubated for half an hour. The fusion reaction was initiated by the addition of 1 M HCl to yield the desired pH.

Chapter 3: Structural and functional studies of modified TBEV FPs

3.0 Introduction

Chapter 2 focused on the design and synthesis of native-like TBEV FP and two mutants, and on investigating their functional and structural properties. The peptides described in Chapter 2 can induce membrane fusion at low pH, and the mutations to residue 107 can affect their fusogenic activity, indicating that the synthetic TBEV FP can serve as a model fusion system. However, the synthetic peptides did not adopt significant β-strand conformation, as the segment in the intact E protein does. This may be due to the fact that in the short peptides studied here, there is no stabilization of the structure via disulfide bond formation and oligomerization, as in the intact protein. Therefore, synthesizing modified FP where these are systematically reintroduced would offer us an opportunity to study the importance of these factors in membrane fusion and the possible conformational changes that may occur during the fusion process.

Section 3.1 of this chapter will outline the rationale for synthesizing modified TBEV FPs. Section 3.2 will be broken down into two sub-sections describing the design, synthesis, structural and functional studies on the FP with a disulfide bond present (Section 3.2.1) and FP trimers (Section 3.2.2). Section 3.3 will summarize the

experimental findings for this chapter, in addition to highlighting some conclusions that may be drawn from the experimental results.

3.1 Rationale for synthesizing modified FPs

As introduced in Chapter 1, the FP of TBEV is a hydrophobic and conserved sequence located at the tip of Domain II in the E protein[106]. This peptide loop in the middle of two β-strands has a tightly folded conformation, probably stabilized by a disulfide bond that links the two strands. The disulfide bond is a single covalent bond derived from the coupling of two thiol groups. In proteins, disulfide bonds are formed between the free thiol groups of cysteines. The disulfide bond stabilizes the protein fold in several ways. It can hold two portions of the protein together to destabilize the unfolded form of the protein by lowering its entropy, making it less favorable compared with the folded form[208]. The disulfide bond may also form the nucleus of a hydrophobic core of the folded protein, by favoring the interaction of surrounding hydrophobic residues with each other[209]. In addition, the disulfide bond can stabilize the folded structure of the protein. Therefore, the introduction of a disulfide bond in the synthetic FP may promote the formation of a relatively stable structure as in the intact protein.

Another factor possibly stabilizing the protein fold is the oligomerization state. The structural studies on E protein of TBEV have indicated that the FP loop is buried in the middle of the protein dimer at the prefusion stage[106] (Figure 1.10), whereas it is exposed

and forms a trimer when the membrane fusion is triggered by acidic pH[107]. This trimerization has also been observed in structures of fusion proteins from class I enveloped viruses, including HIV and influenza virus[41, 47, 92, 93, 210]. Previous studies have indicated that the rate of fusion induced by the FP trimer of HIV is up to 40 times higher than the rate induced by the FP monomer[105], suggesting that the oligomeric topology is functionally important. In addition, the conformation and membrane location of FPs are significant factors which impact the rate of fusion and thus might explain the increased fusion rates of FP oligomers[58, 99]. Therefore, the synthesis of a FP trimer construct of TBEV can not only mimic the oligomerization state of this segment in the intact protein at low pH, but may also possibly stabilize the fold of the peptide.

3.2 Results and discussion

This section will start by describing the design, synthesis and characterization of the TBEV FP which contains a disulfide bond, followed by the studies on the TBEV FP trimer constructs.

3.2.1 TBEV FP with disulfide bond

The synthetic peptide with a disulfide bond, labeled as TFPSS, will be designed and synthesized. The determination of its secondary structure, peptide insertion, and

fusogenic activity will be presented, followed by a discussion of these results.

3.2.1.1 Peptide design

In the intact E protein of TBEV, the FP segment is located in the middle of two β-strands, which are stabilized by the disulfide bond linked between the Cys 92 and Cys 116 residues[106]. In order to mimic the structural and functional characters of this segment in the E protein, we designed a synthetic peptide corresponding to residues 89-119. Since there were three Cys amino acids in this peptide chain and only one disulfide bond was desired, we mutated the Cys 105 residue to alanine in order to avoid the formation of a disulfide bond at this position and the possible disruption of the structure and fusogenic activity of the peptide. The designed peptide sequence is shown in Figure 3.1.

Figure 3.1 Amino acid sequence of target peptide TFPSS, corresponding to residues 89 to 119 in the TBEV E protein. The same numbering is preserved here. Bold indicates mutation at the Cys 105 residue.

$G^{89}TVCKRDQSDRGWGNH\mathbf{A}^{\mathbf{105}}GLFGKGSIVACVKA^{119}$

SS

3.2.1.2 Peptide synthesis

The reduced peptide was synthesized following the optimized method described in Chapter 2, in which the Lys 93 and Arg 94 residues were double coupled during the standard Fmoc peptide synthesis procedure.

The disulfide bond was obtained by the oxidation of the thiol groups in both cysteine residues (Figure 3.2.a). One method to achieve this is to use molecular oxygen. The disulfide bond in the synthetic peptide was formed by exposing the solution to air with slow stirring. The formation of the disulfide bond was monitored by using Ellman's reagent or 5, 5'-dithiobis (2-nitrobenzoate) (DTNB), which is a symmetric aryl disulfide. DTNB can readily undergo a thiol-disulfide interchange reaction in the presence of a free thiol group[211-213] (Figure 3.2.b) to yield 2-nitro-5-thiobenzoate (TNB) which has a relatively intense absorbance at 412 nm. Because the stoichiometry of protein thiol to TNB formed is 1:1, TNB formation can be used to assess the number of thiol groups present. This assay indicated that after exposing a solution of TFPSS to the air for 1 day, > 95% of the free thiol groups in the peptide were oxidized.

3.2.1.3 Characterization of TFPSS

The synthetic TFPSS was characterized by using CD, tryptophan fluorescence spectroscopy, FRET, and photon correlation spectroscopy. Its structural and functional

properties were studied and compared with the WT TBEV FP discussed in Chapter 2.

Figure 3.2 (a) Formal depiction of disulfide bond formation in the protein under oxidizing conditions. (b) Formation of disulfide, as monitored using Ellman's reagent.

(a)

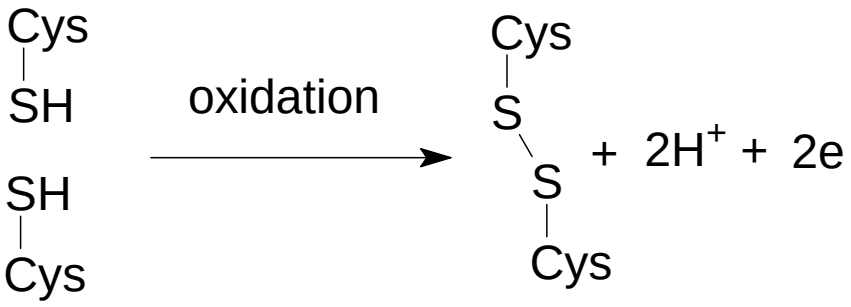

(b)

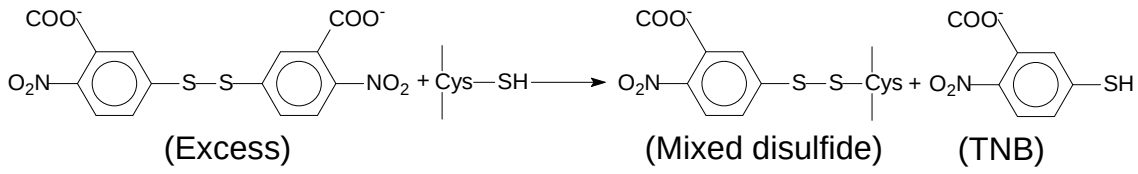

3.2.1.3.1 Far-UV CD spectroscopy

The far-UV CD spectra for the TFPSS are shown in Figure 3.3, and the contents of secondary structural elements were calculated by using the programs CONTIN, SELCON3, and CDSSTR[175] (Table 3.1). As for the WT FP, the change in pH did not affect the fraction of secondary structure. When the peptide was bound to PC/PE SUVs, the secondary structure adopted was similar to the conformation formed in the buffer, in which less than 3 residues adopt helical conformation and more than half of the peptide

Figure 3.3 Far-UV CD spectra for TFPSS (concentration, 50 μM) (a) in 20 mM phosphate buffer, (b) bound to POPC/POPE (molar ratio, 1:1) SUVs, or (c) bound to POPC/POPE/Chol (molar ratio, 1:1:1.5) SUVs. The spectra were recorded at neutral (pink) and acidic pH (dark blue).

(a)

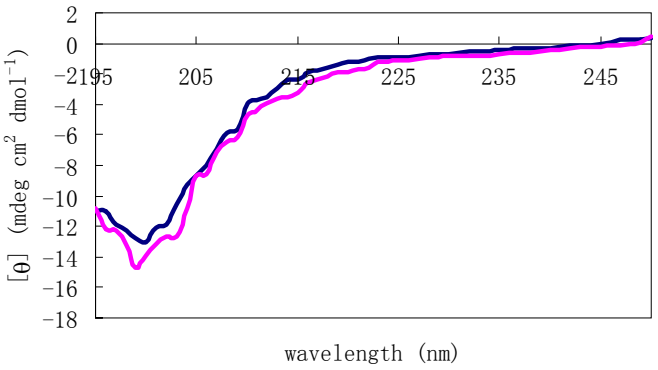

(b)

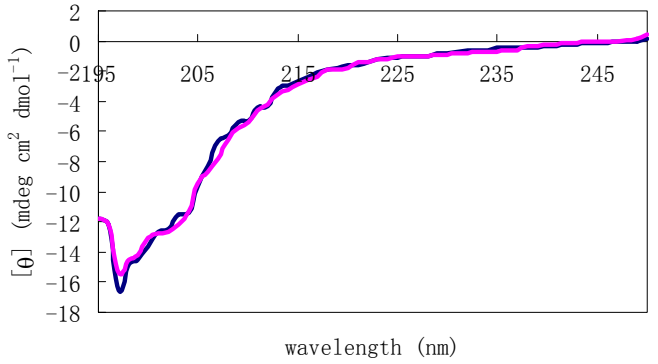

(c)

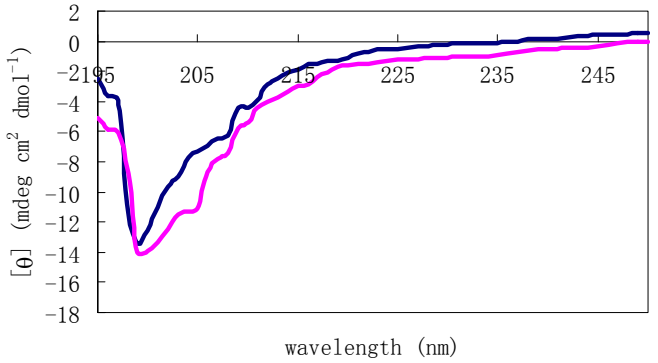

Table 3.1 Secondary structure content of TFPSS in various media and different pH, as extracted from the CD spectra. Spectra fit using CONTIN, SELCON3, and CDSSTR[175]. The error determined from the average of the calculated secondary structure content using the three programs.

		% Helix	% Strand	% Turn	% random coil
Phosphate buffer	**pH 5.5**	8±3	30±4	23±3	39±1
	pH 7.5	8±4	29±4	20±5	43±5
PC/PE (1:1)	**pH 5.5**	7±3	27±2	22±1	44±2
	pH 7.5	8±4	27±5	23±3	42±2
PC/PE/Chol (1:1:1.5)	**pH 5.5**	7±1	45±3	24±5	25±1
	pH 7.5	10±3	43±3	27±4	20±3

was turn and random coil structure. However, the presence of cholesterol in the liposomes resulted in about 15 % more residues in the peptide sequence adopting β-strand conformation. This observation was consistent with the results in Chapter 2 that the direct or indirect interactions of TBEV FP with cholesterol in the lipid bilayers may be the cause of the observed conformational changes. Comparing the fraction of β-strand conformation in TFPSS with that found for WT FP indicates that about 7 more residues in TFPSS adopt a regular secondary structure. The increase in β-strand conformation likely results from the stabilization of the peptide fold by the disulfide bond. It has been shown that the increase in the stability of the folded structure due to the formation of a

disulfide bond is directly proportional to the number of residues between the linked cysteines: the larger the number of the residues between the disulfide, the greater the stability imparted to the folded structure[214, 215]. There are 23 residues between Cys 92 and Cys 116 in TFPSS, which may help the segment between the formed disulfide bond fold.

3.2.1.3.2 Tryptophan fluorescence spectroscopy

As explained in Chapter 2, tryptophan fluorescence spectroscopy is a useful method to determine the extent of peptide insertion into lipid vesicles. The results are shown for TFPSS in Figure 3.4. Similar to the data of TBEV FP without a disulfide bond, TFPSS can insert into PC/PE/Chol LUVs at both acidic and neutral pH. It does not, however, bind well with the cholesterol free membranes. In addition, these results indicate that the formation of a disulfide bond may not enhance the insertion ability of TFPSS. In other words, the increase of β-strand conformation adopted by the peptide does not affect the peptide binding to lipid vesicles. These results suggest that the increased β-strand conformation does not form in the lipid binding portion of TFPSS. The picture which emerges from this and the CD data is that when associated with PC/PE/Chol bilayers, the same portion of WT FP and TFPSS inserts into the liposomes. The depth of insertion appears to be similar based on the fact that the increase of fluorescence intensity was similar when both of the peptides bound to the POPC/POPE/Chol SUVs (Figure 2.8.a and 3.4.a). The only difference between WT FP and TFPSS appears to be in the

non-lipid-binding segment (Figure 3.5).

Figure 3.4 (a) Fluorescence emission spectra of TFPSS in 20 mM HEPES buffer at pH 5.5 (dark blue), and incubated with POPC/POPE/Chol LUVs with molar ratio of 1:1:1.5 (pink) or POPC/POPE LUVs with molar ratio of 1:1 (red) and peptide-to-lipid ratios of 1:100. (b) Fluorescence emission spectra of TFPSS in 20 mM HEPES buffer at pH 7.5 (dark blue), and incubated with POPC/POPE/Chol (molar ratio, 1:1:1.5) LUVs, with peptide-to-lipid ratios of 1:100 (pink).

(a)

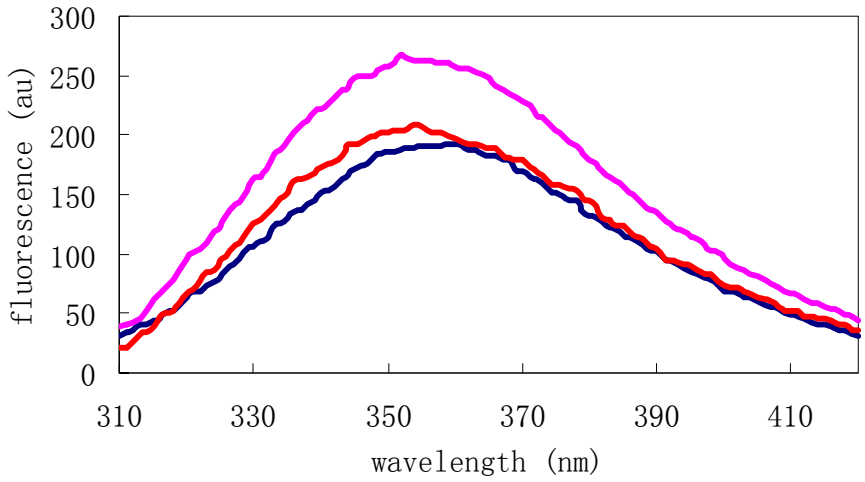

(b)

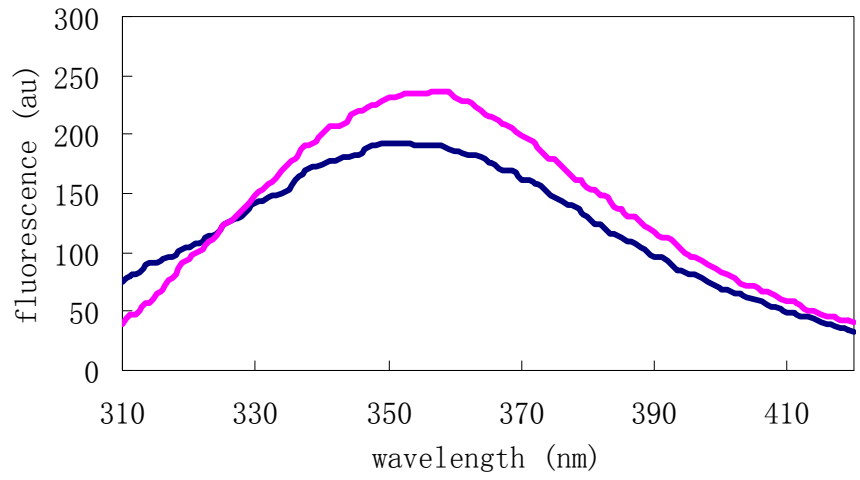

Figure 3.5 Proposed structures of (a) WT and (b) TFPSS when bound to PC/PE/Chol bilayers. The binding portion of both peptides has similar insertion depth. There are 6 more residues adopting β-strand conformation in the non-lipid-binding segment in TFPSS than in WT. The disulfide in TFPSS is colored in green.

(a) **(b)**

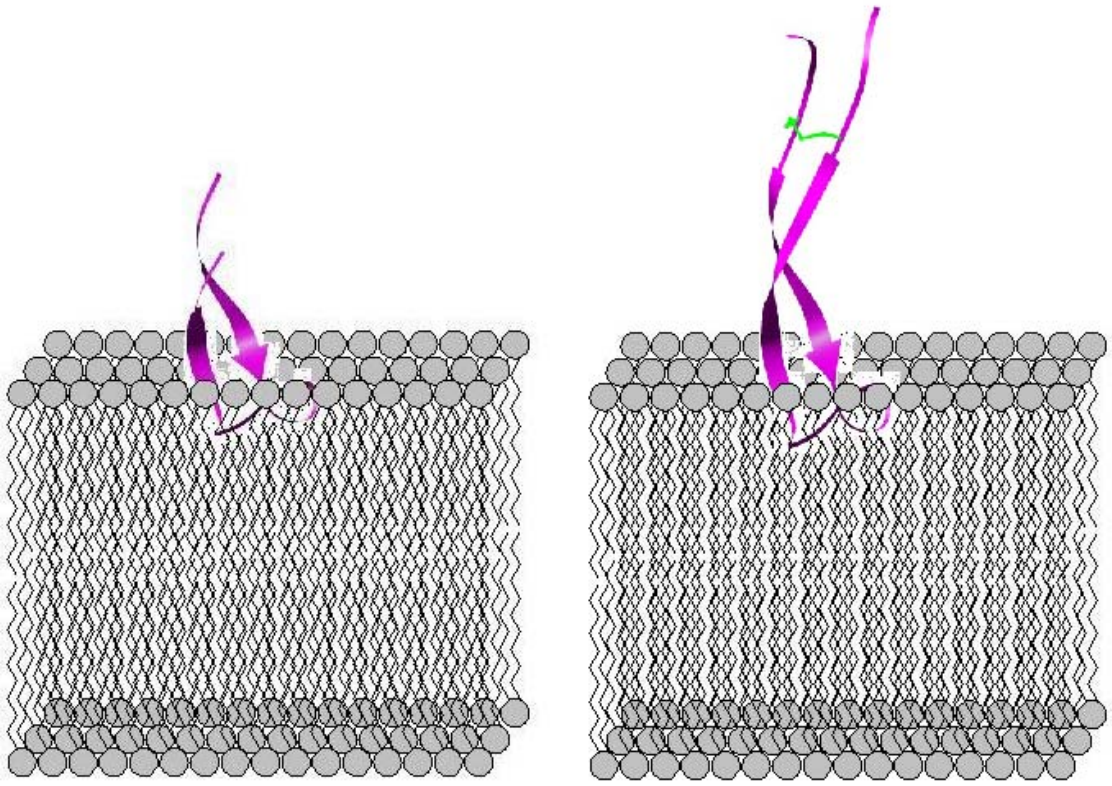

3.2.1.3.3 FRET assay

The fusogenic activity of TFPSS was determined by using a FRET assay. The results are shown in Figure 3.6. No membrane fusion was observed at a pH of 7.5. However, the synthetic TBEV FP with disulfide bond induced membrane fusion rapidly within the first 15 seconds after acidification. Within 15 seconds, the fusion extent reached a maximum

of around 40%. Similar results were obtained from the WT peptide in Chapter 2. Both the initial rate and final extent of fusion were almost the same for both peptides under the same conditions. A comparison indicated that the presence of the disulfide bond, though increasing the structural content of the peptide, did not increase the activity. This suggests that the overall structure of the peptide does not correlate with its function. Rather the ability of a segment of the peptide to interact and insert into the membrane and the structure of this segment dictate whether a given peptide will display functional activity. Furthermore, the substitution of Ala at position 105 has no effect on the fusogenic activity of the TBEV FP, indicating that this residue (and the corresponding Cys 105 in the E protein) may not participate in the peptide-lipid interaction.

Figure 3.6 Fusion of synthetic TFPSS peptide with liposomes consisting of POPC/POPE/Chol (molar ratio, 1:1:1.5) at pH 5.5 (dark blue) and pH 7.5 (pink). The peptide-to-lipid ratios were 1:20. The zero represents the time of acidification for the curve at pH 5.5. The zero was set arbitrarily for the data at pH 7.5.

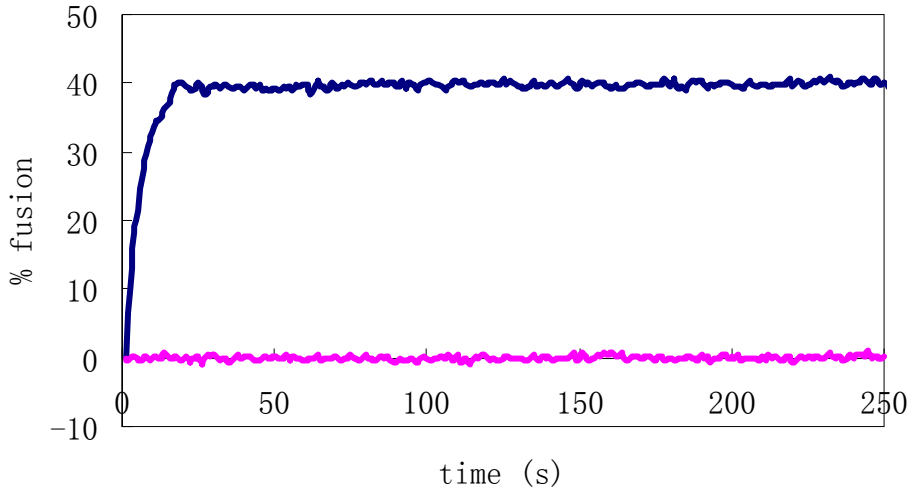

3.2.1.3.4 Photon correlation spectroscopy

As in Chapter 2, we have also determined fusogenic activity using photon correlation spectroscopy. We have applied this technique to study the membrane fusion induced by TFPSS and the effect of membrane composition and temperature on fusion. The results are shown in Figure 3.7. As with the data from the investigation on the TBEV FP without a disulfide bond, the fusion induced by TFPSS was pH dependent. The average size of the vesicles increased as the pH decreased. The pH dependence exhibited a threshold around pH 7.0. As before, the presence of cholesterol enhances activity, but is not essential for fusion to take place. These results indicate that the presence of a disulfide bond and the replacement of Cys 105 residue by Ala do not affect the fusogenic activity of TBEV FP, further supporting to the picture that emerged in Section 3.2.1.3.2 (Figure 3.5). Furthermore, with TFPSS, the pH-dependent vesicle size changes at 37 ℃ and 20 ℃ were similar. The average size of vesicles with TFPSS at pH 5.5 was 1.5 times larger than vesicles at pH 7.5, at both temperatures. Though the temperature dependence of fusion for WT FP is unknown, we can speculate that WT FP has a similar fusogenic activity as TFPSS at 20 ℃, because both peptides behave exactly the same at the higher temperature of 37 ℃. The fast and efficient fusion induced by TBEV FP in the temperature range of 20-37 ℃ was consistent with previous reports on the intact E protein of TBEV[110], indicating that the binding portion of TFPSS on the liposomes might share the same conformation with the intact E protein. Compared with other enveloped

viruses, the TBEV fusion reaction differs markedly from the fusion induced by SFV, which also has an internal FP loop located at the same relative position in the fusion protein as TBEV[106, 117-121]. For example, with SFV, the fusogenic activity at 37 ℃ is about 16 times larger than at 20 ℃[202, 216, 217]. The present observation that TBEV fusion is not drastically reduced as temperature is decreased suggests that the possible conformational change in the FP during the fusion process represents a very facile process with a low activation energy.

Figure 3.7 pH dependence in the average size of vesicles induced by TFPSS. Dark blue curve, TFPSS with POPC/POPE/Chol (molar ratio, 1:1:1.5) LUVs at 37 ℃; pink curve, TFPSS with POPC/POPE (molar ratio, 1:1) LUVs at 37 ℃; red curve, TFPSS with POPC/POPE/Chol (molar ratio, 1:1:1.5) LUVs at 20 ℃. The data are an average of two independent measurements. The lipid concentration was 26 μM and the peptide-to-lipid ratios were 1:1.

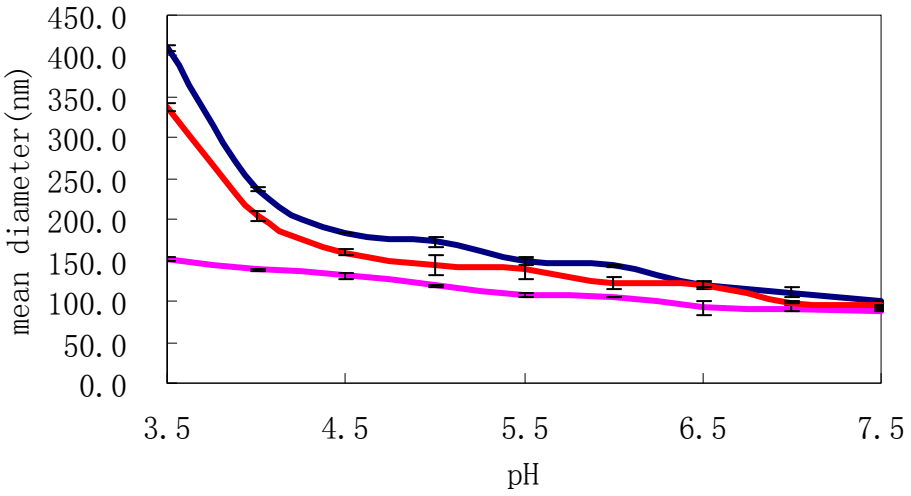

3.2.2 TBEV FP trimer

In this section, the effect of oligomerization on the structure and activity of TBEV FP will be discussed. Since the hydrophobicity of WT FP is 0.13[218], oligomerization would increase the local concentration of the peptide strands, which may make the peptide more difficult to dissolve in aqueous solution. As introduced in Chapter 1, a sequence containing several lysine residues is often linked at the C-terminus of synthetic FPs so as to solubilize the entire peptide[60, 105]. In order to investigate the effect of solubility on the conformational and functional features of TBEV FP, peptides with additional soluble segments were synthesized and characterized using biophysical techniques.

3.2.2.1 Peptide design

The crystal structure of the E protein in flaviviruses shows that the protein is trimeric at the postfusion stage[77, 107] (Figure 1.9.b). The FPs of the three subunits come together to form a membrane-inserting anchor at the tip of the trimer. In an effort to mimic the biologically relevant topology in a peptide model system and study the structural and functional effects of trimeric oligomerization, we have designed a FP trimer, TFPtr, whose three FP strands were chemically bound at their C-termini[105]. The individual strands consist of residues 93-113 in the E protein[106]. In order to avoid the formation of intermolecular disulfide bonds, the Cys 105 residue was replaced by Ala. As discussed in

Section 3.2.1, this mutation did not perturb the structure and activity of the FP with disulfide bond. To ensure that the mutation does not disturb the structure and activity of the selected sequence and to investigate the effects of oligomerization, the monomeric peptide, TFPmn, was also synthesized as the control system. In order to investigate whether solubility has an impact on the structure and activity of TBEV FP, we also designed a TBEV FP monomer and trimer with a six-lysine sequence at their C-termini, TFPmnK and TFPtrK, respectively. The amino acid sequences of all the peptides are listed in Figure 3.8. One strand of the FP trimer had a C-terminal β-alanine because the small side chain ensures efficient synthesis of the target peptide.

Figure 3.8 Amino acid sequences of the target peptides: TFPmn, TFPtr, TFPmnK, and TFPtrK.

TFPmn
K^{93}RDQSDRGWGNHAGLFGKGSI^{113}
TFPtr
K^{93}RDQSDRGWGNHAGLFGKGSI^{113}KA
K^{93}RDQSDRGWGNHAGLFGKGSI^{113}K
|
K^{93}RDQSDRGWGNHAGLFGKGSI^{113}K
TFPmnK
K^{93}RDQSDRGWGNHAGLFGKGSI^{113}KKKKKK
TFPtrK
K^{93}RDQSDRGWGNHAGLFGKGSI^{113}KKKKKKA
|
K^{93}RDQSDRGWGNHAGLFGKGSI^{113}KKKKKK
|
K^{93}RDQSDRGWGNHAGLFGKGSI^{113}KKKKKK

3.2.2.2 Peptide synthesis

The monomers were synthesized using the optimized protocol described in Chapter 2. The trimers were synthesized with a lysine side-chain scaffold[105]. As shown in Figure 3.9, the trimer backbone was firstly formed by two sequential couplings of Fmoc-Lys(Mtt) followed by a coupling with Fmoc-Lys(Boc). After the first and second couplings, the Mtt group on the lysine side chain was removed with 1 % TFA in DCM[219]. The rest of the trimer was then synthesized using the same optimized procedure as used for the synthesis of the monomers. The purified yield of the synthetic peptide trimers was about 6 % (~45 mg per synthesis). Considering that this synthesis is equivalent to the direct synthesis of ~70-mer, however, this yield is considered to be good. Recently, another approach for synthesizing peptide trimers has been developed[220]. It is based on the cross-linking of a peptide monomer with a dimer, each of which contains a single cysteine. Since the formation of a specific disulfide can be complex, we did not apply this approach to synthesize the TBEV FP trimers.

3.2.2.3 Characterization of TFPtr, TFPmn, TFPtrK, and TFPmnK

Biophysical experiments, which will be discussed below, were conducted to assess and compare the secondary structures and relative activities for each of the synthetic FPs listed in Figure 3.8.

Figure 3.9 Schematic representation of the synthesis of the trimer backbone.

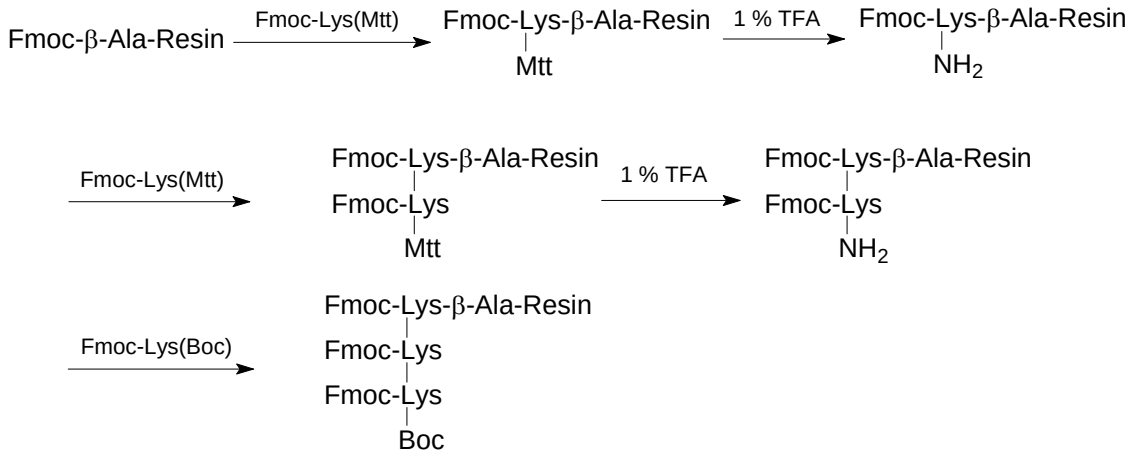

3.2.2.3.1 Far-UV CD spectroscopy

The conformations of the four synthetic peptides were assessed using far-UV CD spectroscopy (Figure 3.10). As shown in Table 3.2, the CD spectra of the four synthetic peptides were characteristic of turn and random coil structure adopted by more than half of the residues when dissolved in buffer and associated with lipids. The secondary structures of the peptides did not change much between the neutral and acidic environments, consistent with the previous studies on the other synthetic TBEV FPs. When associated with POPC/POPE/Chol SUVs, the conformation of TFPtr (Figure 3.10.c) was different from that in buffer (Figure 3.10.a). About 10 more residues in TFPtr adopted a β-strand conformation, and the fraction of random coil structure was significantly decreased. This is in agreement with results obtained for class I FP trimers associated with cholesterol containing membranes, which have been shown to more

Figure 3.10 Far-UV CD spectra for synthetic peptides at pH 5.5 (dark blue) and 7.5 (pink). (a) TFPtr in phosphate buffer; (b) TFPtr bound to PC/PE (molar ratio, 1:1) SUVs; (c), (d), (e), and (f), TFPtr, TFPmn, TFPtrK, and TFPmnK, respectively, bound to PC/PE/Chol (molar ratio, 1:1:1.5). The peptide-to-lipid ratios were 1:20.

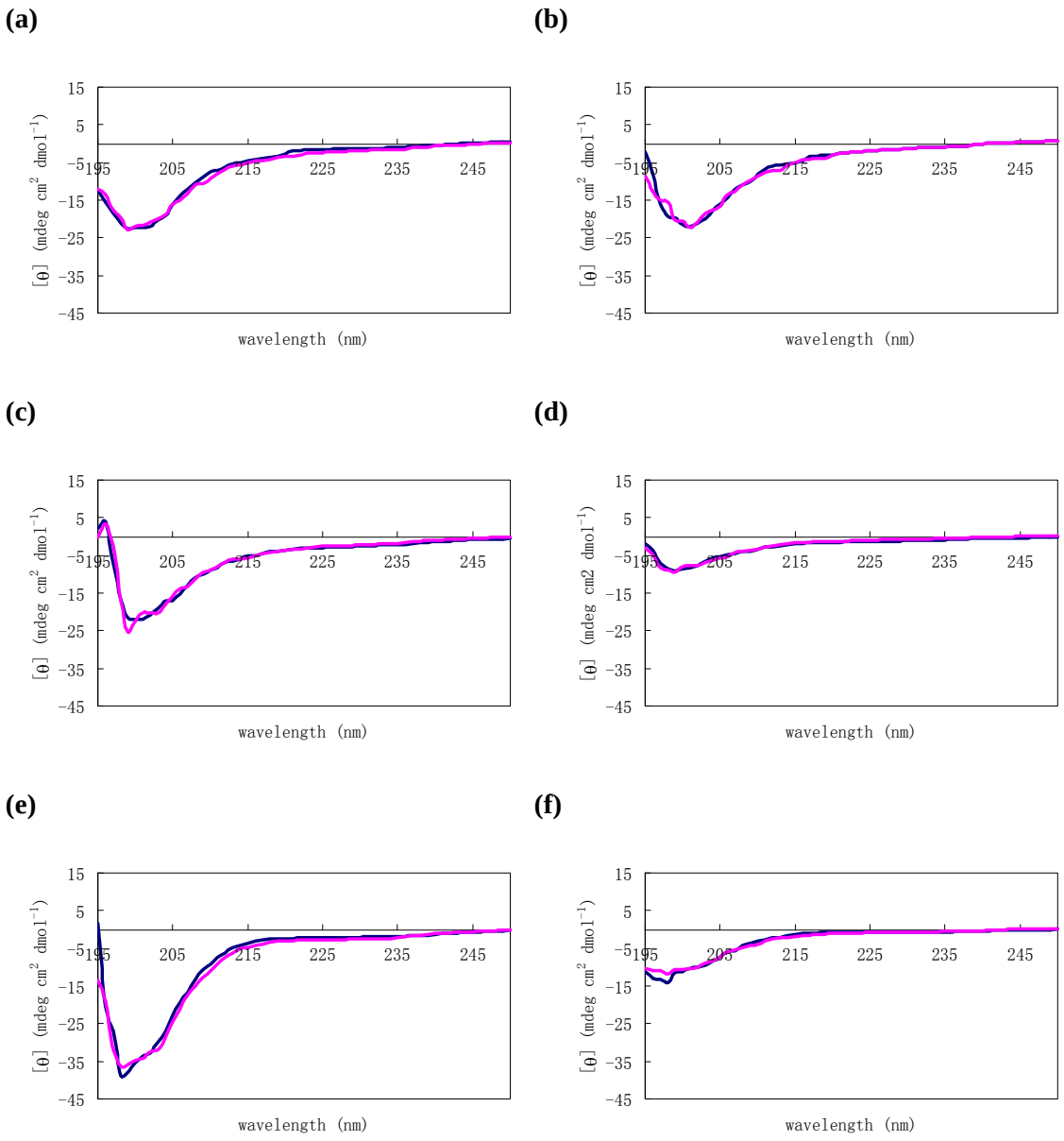

adopt β-strand conformation[74, 104, 105]. The CD data also show that in TFPtr, about 7 residues per branch adopt β-strand structure, similar to TFPmn and less than the 13 residues in TFPSS. TFPmn adopted a similar conformation to that of the WT peptide

Table 3.2 Secondary structure content of TFPtr, TFPmn, TFPtrK, and TFPmnK in various media and different pH, as extracted from the CD spectra. Spectra fit using CONTIN, SELCON3, and CDSSTR[175]. The error determined from the average of the calculated secondary structure content using the three programs.

			% Helix	% Strand	% Turn	% random coil
TFPtr	**Phosphate buffer**	**pH 5.5**	20±1	16±2	26±3	39±4
		pH 7.5	17±2	20±3	25±1	38±4
	PC/PE (1:1)	**pH 5.5**	18±3	18±3	26±3	38±3
		pH 7.5	21±4	16±2	25±4	38±2
	PC/PE/Chol (1:1:1.5)	**pH 5.5**	16±3	32±3	22±4	30±2
		pH 7.5	14±5	29±5	25±4	32±4
TFPmn		**pH 5.5**	11±4	30±3	21±3	38±5
		pH 7.5	11±3	32±3	21±2	35±4
TFPtrK		**pH 5.5**	18±3	16±3	27±2	39±3
		pH 7.5	17±2	18±4	25±2	40±5
TFPmnK		**pH 5.5**	11±4	17±4	24±4	48±4
		pH 7.5	13±3	15±4	24±2	48±1

(also 21 residues) observed in Chapter 2, confirming that the replacement of Cys 105 residue by Ala did not disturb the peptide folding. TFPmnK and TFPtrK did not fold well when bound to PC/PE/Chol SUVs, as seen by the fact that the proportion of β-strand

conformation is the same as that in buffer (data did not show, but similar to the results of TFPtr in buffer). The reason for this might be that the soluble sequence favors the partitioning of the peptides in the buffer rather than into the liposomes. This will be examined further in the following section.

3.2.2.3.2 Tryptophan fluorescence spectroscopy

The fluorescence of the Trp 101 residue in the synthetic peptides was used to determine their ability to insert into membrane bilayers. In Figure 3.11, the emission spectra of the peptides in buffer and in the presence of lipid LUVs are compared. In Figure 3.11.a, the Trp emission intensity was enhanced for TFPtr in the presence of POPC/POPE/Chol vesicles at low pH. These results suggest that the Trp 101 residue inserts into the hydrocarbon core of the bilayers. Interestingly, the insertion of TFPtr was concentration dependent. When the peptide-to-lipid ratios were below 1:150, higher concentration favors the insertion of the peptide into the lipid bilayers, resulting in an increase in fluorescence intensity. However, when peptide-to-lipid ratios were above 1:150, the trimer interacted only weakly with the lipid vesicles, resulting in a decrease in fluorescence intensity, which may be due to the saturation of the peptides on the surface of the vesicles under these conditions. Further experiments on TFPtr indicated that the peptide can penetrate the POPC/POPE/Chol LUVs not only at low pH, but also at neutral pH (Figure 3.11.b). However it can only interact weakly with the POPC/POPE

Figure 3.11 Fluorescence emission spectra of the Trp 101 residue in the synthetic peptides. (a) TFPtr in 20 mM HEPES buffer at pH 5.5 (dark blue), and incubated with POPC/POPE/Chol (molar ratio, 1:1:1.5) LUVs using peptide-to-lipid ratios of 1:300 (pink), 1:150 (red), and 1:60 (black); (b) TFPtr in 20 mM HEPES buffer at pH 7.5 (dark blue), and incubated with POPC/POPE/Chol (molar ratio, 1:1:1.5) LUVs using peptide-to-lipid ratios of 1:300 (pink); (c) TFPtr in 20 mM HEPES buffer at pH 5.5 (dark blue), and incubated with POPC/POPE (molar ratio, 1:1) LUVs using peptide-to-lipid ratios of 1:300; (d), (e), and (f), TFPmn, TFPtrK, and TFPmnK, in 20 mM HEPES buffer at pH 5.5 (dark blue), and incubated with POPC/POPE/Chol (molar ratio, 1:1:1.5) LUVs using peptide-to-lipid ratios of 1:100, 1:300, and 1:100 (pink), respectively.

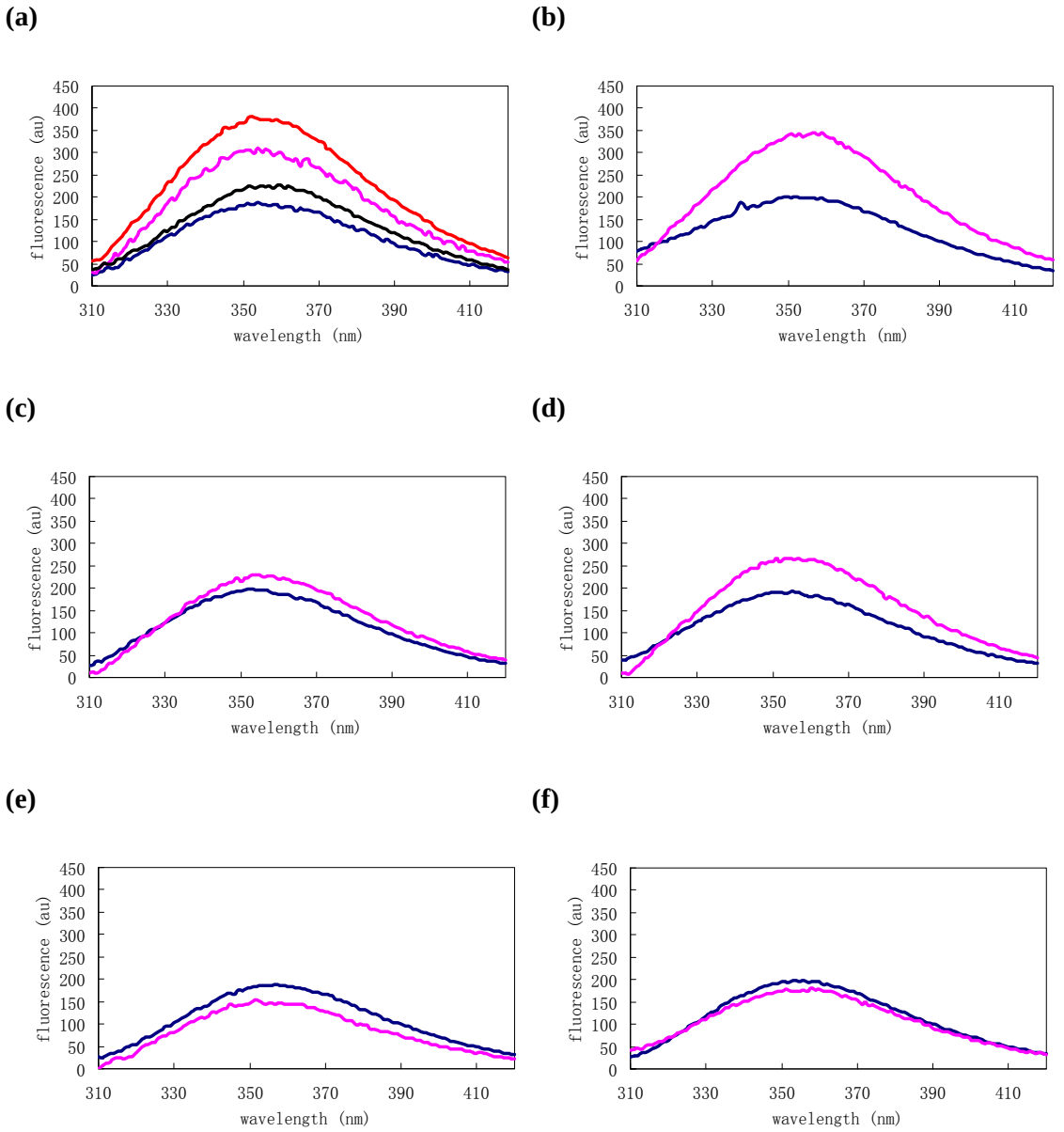

lipid vesicles (Figure 3.11.c) based on the fact that the increase of fluorescence intensity when the TFPtr was bound to cholesterol free LUVs was not as extensive as when bound to the cholesterol containing liposomes. This difference indicated that the presence of cholesterol in the lipid vesicles promoted peptide insertion, possibly due to interactions between the cholesterol and TFPtr. Finally, the decreases in Trp emission intensity, illustrated in Figures 3.11.e and Figure 3.11.f, suggest that TFPmnK and TFPtrK do not associate strongly with POPC/POPE/Chol LUVs. This may be due to the fact that the more water-soluble TFPmnK and TFPtrK partition more readily in aqueous solution than into lipid vesicles. If one assumes that peptide-lipid interactions promote β-strand formation, then the limited insertion of the lysine containing mutants may explain the smaller proportion of β-strand conformation observed in the CD spectra (Figure 3.10).

3.2.2.3.3 FRET assay

As before, the FRET assay was used to probe the fusogenic activity of the four constructs given in Figure 3.8. In this assay, the final extent of lipid mixing was used as a general measurement of peptide fusogenic activity. As seen in Figure 3.12, even though the concentration of TFPtr was only one third of that of TFPmn, TFPtr can induced about 1.5 times more fusion extent than TFPmn, and the fusion rate of TFPtr was much faster than that of TFPmn. Within the first 5 s, TFPtr had induced the fusion of about 50 % lipid vesicles, and the final extent of fusion was about 60 %. For TFPmn, on the other hand,

Figure 3.12 Induction of liposome fusion by TFPtr (dark blue), TFPmn (pink), TFPtrK (red) and TFPmnK (black). Membrane fusion induced by 1.7 μM TFPtr, 5 μM TFPmn, 1.7 μM TFPtrK, or 5 μM TFPmnK was measured by FRET at pH 5.5 and 37 ℃. The LUVs contained POPC, POPE, and cholesterol with the molar ratio of 1:1:1.5, and the total lipid concentration was 100 μM.

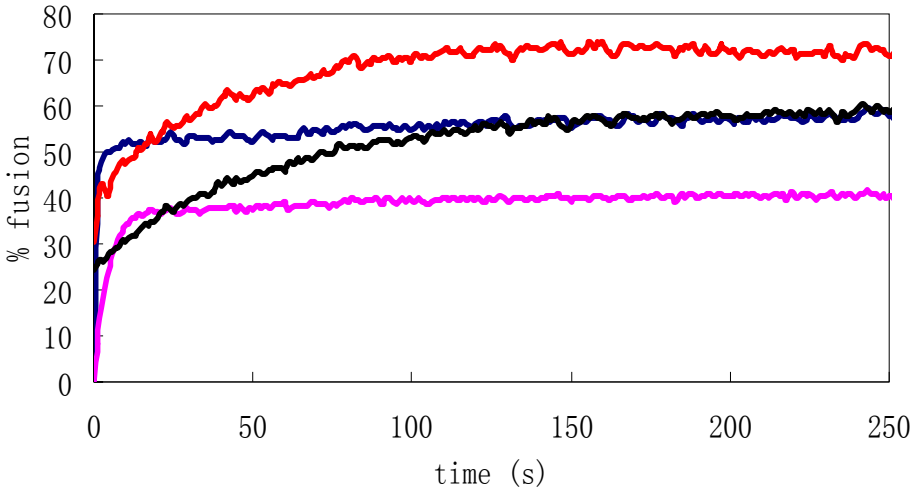

more than 35 % lipid vesicles had fused within the first 15 s, and the final extent of fusion was about 40 %. The extent of fusion induced by the synthetic peptide, M(t), can be fitted by equation 3.1[105]:

$$M(t) = M_0 + M_1(1-e^{-k_1 t})+M_2(1-e^{-k_2 t}) \qquad (3.1)$$

where M_0, M_1, M_2, k_1 and k_2 are fitting parameters. M_0, represents the extent of fusion prior to adding acid. The induced fusion increase after acidification is modeled as the sum of a fast buildup with overall induced fusion M_1 and rate constant k_1, and a slow buildup with overall induced fusion M_2 and rate constant k_2. The fit is much poorer if a single buildup rate is used. The fitting results were given in Table 3.3. In the fitting of fusion induced by TFPtr and TFPmn, M_0 was around zero and the fast component likely

Table 3.3 Fitting parameters of TFPtr, TFPmn, TFPtrK, and TFPmnK-induced vesicle fusion using equation 3.1.

	M_0 (% fusion)	M_1 (% fusion)	k_1 (s^{-1})	M_2 (% fusion)	k_2 (s^{-1})	R^2
TFPtr	**0.1±0.7**	**50.6±0.7**	**1.63±0.07**	**8.1±0.2**	**0.009±0.001**	**0.97238**
TFPmn	**0±0.8**	**39.8±0.8**	**0.19±0.01**	**0±0.2**	**0±0.001**	**0.93146**
TFPtrK	**30±1**	**9±1**	**1.1±0.3**	**32.7±0.4**	**0.027±0.001**	**0.98104**
TFPmnK	**24.5±0.3**	**3±1**	**0.06±0.03**	**32±1**	**0.016±0.001**	**0.99461**

represented the fusion induced from the initial interaction of FPs with membranes. In comparison, the slow component M_2 in induced fusion is small and can therefore be ignored. The fitted rate constant k_1 for TFPtr and TFPmn was 1.63 and 0.19 s^{-1}, respectively. Studies on the HIV FPs have shown that the peptide trimer can induce vesicle fusion at a rate that is up to 40 times larger than the rate induced by the FP monomer[105]. These results suggest that trimer formation increases the local concentration of the FP strands in the membrane. In addition, the fusion rate induced by TBEV FP trimer is much faster than HIV FP trimer (0.43 s^{-1})[105], which is consistent with the comparison of the data for intact fusion proteins[99, 110]. Surprisingly, the extent of fusion induced by TFPtrK or TFPmnK was larger than that induced by TFPtr or TFPmn, respectively. The extent of fusion induced by TFPmnK was smaller than that induced by TFPtrK, but similar to the extent induced by TFPtr. However, the fitted rate constant k_1 for TFPtrK and TFPmnK was smaller than TFPtr and TFPmn, respectively. The weaker

interactions between the lysine containing constructs and the lipids can possibly account for the smaller k_1 of fusion, but do not serve to explain why these peptides are better at fusing liposomes. The slow component contributed more to the fusion of TFPtrK and TFPmnK than to the fusion of TFPtr and TFPmn. These data indicated that the additional lysine sequence might facilitate the vesicle mixing, but the rate was slow. The slow component constant k_2 for TFPtrK was larger than that for TFPmnK, indicating that the higher local concentration of the polar segment can enhance the fusion rate induced by the lysines. Furthermore, for the fusion of TFPtrK and TFPmnK, the M_0 was not zero, indicating these two peptides can induce fusion prior to the acidification (further discussion will be present in the following section).

3.2.2.3.4 Photon correlation spectroscopy

In photon correlation spectroscopy (Figure 3.13), the sizes of the liposomes were measured as a function of pH. Because fusion induced by the peptides results in aggregation of lipid vesicles, the increase in the mean diameters of LUVs measured by this assay is used to quantify fusogenic activity of the peptides. Since the trimers have three times as many strands per molecule as their monomers, the experiments were performed with the concentrations of the trimers being one third of those of monomers. In these experiments, all peptides initiated lipid vesicle aggregation, as the pH value decreased. Since the size of the LUVs alone is independent of pH, the increase in mean

Figure 3.13 pH dependence in the average size of vesicles induced by TFPtr (dark blue), TFPmn (pink), TFPtrK (red) and TFPmnK (black) as measured by photon correlation spectroscopy. The data are an average of two independent measurements. The liposome concentration was 26 μM. TFPtr, TFPmn, TFPtrK and TFPmnK were at the concentration of 9 μM, 26 μM, 9 μM and 26 μM, respectively.

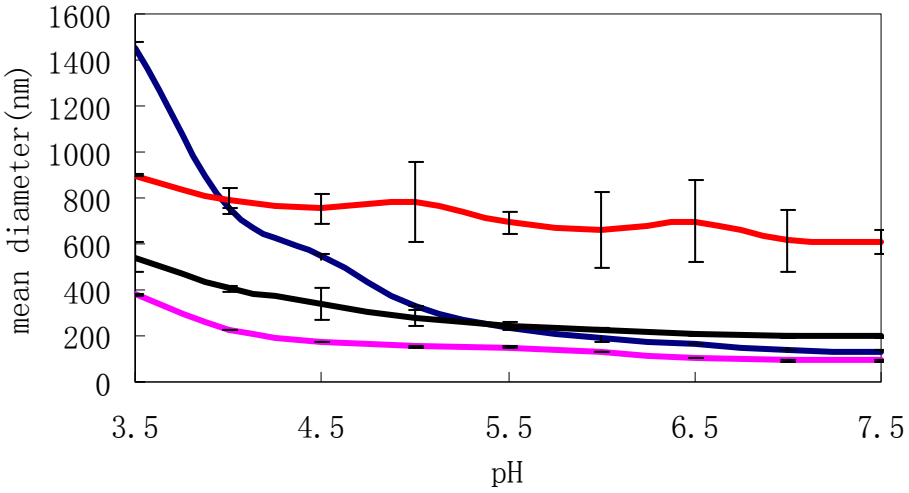

diameters of the LUVs in the presence of the peptides is likely to be due to the fusion induced by the synthetic FPs at low pH. The mean diameters of lipid vesicles with TFPtr, TFPmn, TFPtrK, and TFPmnK at pH 5.5 were 2.7, 1.7, 8.0, and 2.8 times larger than the size of the peptide-free liposomes, respectively. These data were consistent with the results from the FRET assay, in which the final extent of fusion induced by TFPmn was smallest, followed by TFPmnK and TFPtr, and TFPtrK being largest at pH 5.5. The mean diameter ratios of LUVs at pH 5.5 to the vesicles at pH 7.5 with TFPtr, TFPmn, TFPtrK, and TFPmnK were 1.8, 1.6, 1.1 and 1.2, respectively. If one quantifies fusogenic activity as the change in mean diameter ratios, then clearly TFPtr possess the highest fusogenic activity, while the fusogenic activities of the FP segment in TFPtrK and TFPmnK are

weaker. This may be due to the shallower insertion of TFPtrK and TFPmnK into target membranes and their lack of a defined structure. The additional lysine sequence does have the effect of producing larger vesicles, consistent with the observations in the FRET assay. Previous studies have shown that PE vesicles can aggregate at low pH and that the aggregation can also happen at pH 9.0 when divalent cations are added[221, 222]. Perhaps, the presence of the positively charged lysines on the surface of the liposomes contained in TFPtrK and TFPmnK promotes aggregation in a similar way. This remains to be investigated.

3.2.2.3.5 ^{13}C CP/MAS solid state NMR

The structural and functional studies on the four synthetic peptides containing the TBEV FP sequence indicate that TFPtr, which is the trimeric construct and has the highest fusogenic activity, can serve as the model system to mimic the behavior of FP in the intact protein. As previously stated, our aim is to establish whether there is a relationship between the structure and the membrane fusion induced by the TBEV FP, and whether fusion is accompanied by a pH dependent conformational change. The studies on the FP of influenza virus have shown that its structure is different when the pH is changed from neutral to acidic, possibly triggering membrane fusion at low pH[56]. Furthermore, the H^+ cations present at low pH may break the salt bridges and protonate the His 104 residue, which might cause subtle structural changes in the TBEV FP. The

CD results yielded the overall secondary structure of the TBEV FPs, but it does not provide localized structural information. We therefore attempted to use solid-state NMR spectroscopy to develop the high-resolution structural models of membrane-associated TBEV FPs.

We tried to apply ^{13}C CP/MAS to assign the TFPtr whose Phe 108 residue was labeled by ^{13}CO. The carbonyl signals obtained in the chemical shift range of 160-190 ppm are shown in Figure 3.14. For the lyophilized sample, there was a predominant peak shown in the spectrum with a chemical shift of ~175 ppm (Figure 3.14.a), indicating that the ^{13}CO labeling in the peptide was successful. The peak was broad suggesting that the TFPtr adopted several conformations as the lyophilized powder. Figure 3.14.b showed a peak at ~174 ppm, which was assigned to the CO groups in the POPC and POPE lipids[223]. Compared to the peptide-free NMR spectrum, the spectra of TFPtr associated with membranes did not show significant differences in the CO region. Because of the overlap of the large natural abundance signal from the lipid carbonyls and the low signal to noise ratio in this region, the signal from the peptide was difficult to distinguish (Figure 3.14.c). In order to try to reduce the mobility in the sample, we decreased the temperature to -40 ℃[224]. However, no new peak or shoulder was observed (Figure 3.14.d). The reason for this might be that the peptide was still too mobile at this temperature, which may indeed be the case given the direct detection spectrum obtained (Figure 3.14.e). In this spectrum the carbonyl signal intensity was high, indicating that the peptide/lipids were too flexible under this condition. Most likely, however, the main reason for the results obtained from

Figure 3.14 ^{13}C NMR spectra of: (a) CP/MAS with lyophilized TFPtr at room temperature; (b) CP/MAS with POPC/POPE/Chol and pH 5.0 at -40 ℃; (c) CP/MAS with TFPtr and POPC/POPE/Chol at pH 5.0 and room temperature; (d) CP/MAS with TFPtr and POPC/POPE/Chol at pH 5.0 and -40 ℃; (e) direct detection with TFPtr and POPC/POPE/CHol at pH 5.0 and -40 ℃; (f) CP/MAS with TFPtr and POPC/POPE/Chol at pH 7.4 and -40 ℃ in the chemical shift range of 160-190 ppm. 20k scans, a spinning speed of 8 kHz, a contact time of 1 ms and a delay time of 2 s were used.

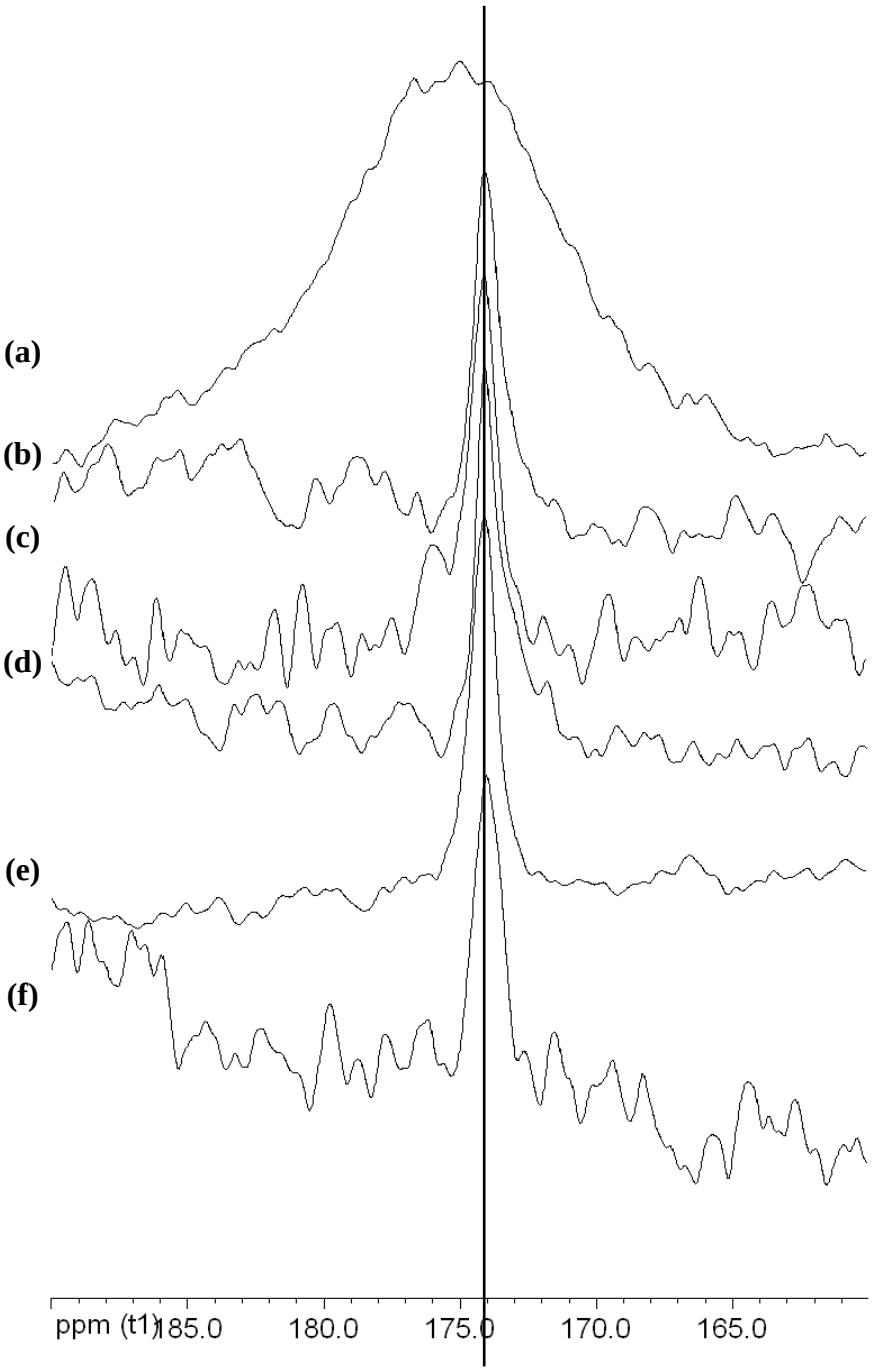

the ^{13}C CP/MAS spectra is nature of the interaction of TFPtr with lipids. Tryptophan fluorescence spectroscopy experiments have demonstrated that when the peptide-to-lipid ratios are above 1:150 (as they were for the NMR experiments), the peptide interacts weakly with the lipid vesicles. Therefore, the effective concentration of TFPtr in the solid-state NMR samples was too low for us to detect the peptide clearly.

3.3 Summary and conclusions

This chapter has presented the design, synthesis and characterization of several modified FPs from TBEV in the hopes of creating more native-like peptides, and to study the relationship between their structures and activities. Two different approaches were developed and characterized. The first one used a disulfide bond to stabilize the folded structure, and the second one mimicked the oligomerization state of E protein of TBEV at the postfusion stage. The former approach was successful in stabilizing the folded structure, and the latter approach resulted in an increase in the fusion rate and in the extent of fusion induced by TBEV FP.

The disulfide bond was formed by oxidation of the thiol groups on the residues Cys 92 and Cys 116. In order to avoid the disulfide forming at Cys 105 residue, it was replaced by Ala. CD spectroscopy demonstrated that more β-strand conformation was formed in the TFPSS than in the WT peptide studied in Chapter 2, indicating the folded structure was stabilized by the disulfide bond. However, the peptide penetration and

fusogenic activity did not change, indicating that lipid-binding portion in the FP might fold similar structure as in the WT FP without the disulfide. The studies on the effect of temperature on the fusogenic activity of TFPSS indicated that the conformational change in the TBEV FP at different fusion stages might be a facile process with a small energy barrier.

The structural and functional studies on the oligomerization were carried out on the synthetic peptide trimer, TFPtr, linked with a lysine side-chain scaffold at C-terminus. The comparison of structure and activities with the analogous monomer, TFPmn, indicated that the close proximity of FP strands in TFPtr can increase the rate and extent of membrane fusion induced by this FP. Therefore, TFPtr can serve as a model fusion system to study the structure of FPs during the fusion process. In order to promote the solubility of synthetic FPs in aqueous solution, we attached a six-lysine segment on the C-terminus of the peptide trimer and monomer and investigated the effect of having an additional water-soluble sequence on the peptide fold and functional properties. The results showed that the additional soluble sequence can induce PC/PE/Chol vesicle aggregation at neutral pH and prevent the peptide binding to liposomes. The latter observation account for the weaker fusogenic activity of the FP segments in these two peptides.

A picture (Figure 3.15) has emerged from the CD data, the insertion ability and the fusion induced by WT FP, TFPSS and TFPtr. When associated with lipid bilayers, the same portion of the WT FP, TFPSS and TFPtr inserts into the liposomes. The depth of

insertion appears to be similar. The only difference between TFPSS and the other two disulfide-free peptides appears to be in the non-lipid-binding segment. Finally, the close proximity of three FP segments in TFPtr causes stronger fusogenic activity than WT FP and TFPSS due to the higher local concentration of the peptide strands.

Figure 3.15 Proposed structures of (a) WT, (b) TFPSS and (c) TFPtr when binding to PC/PE/Chol bilayers. The binding portion of all peptides has similar insertion depth. There are 6 more residues adopting β-strand conformation in the non-lipid-binding segment in TFPSS than in WT and in each branch of TFPtr. The disulfide in TFPSS is colored in green.

(a) **(b)** **(c)**

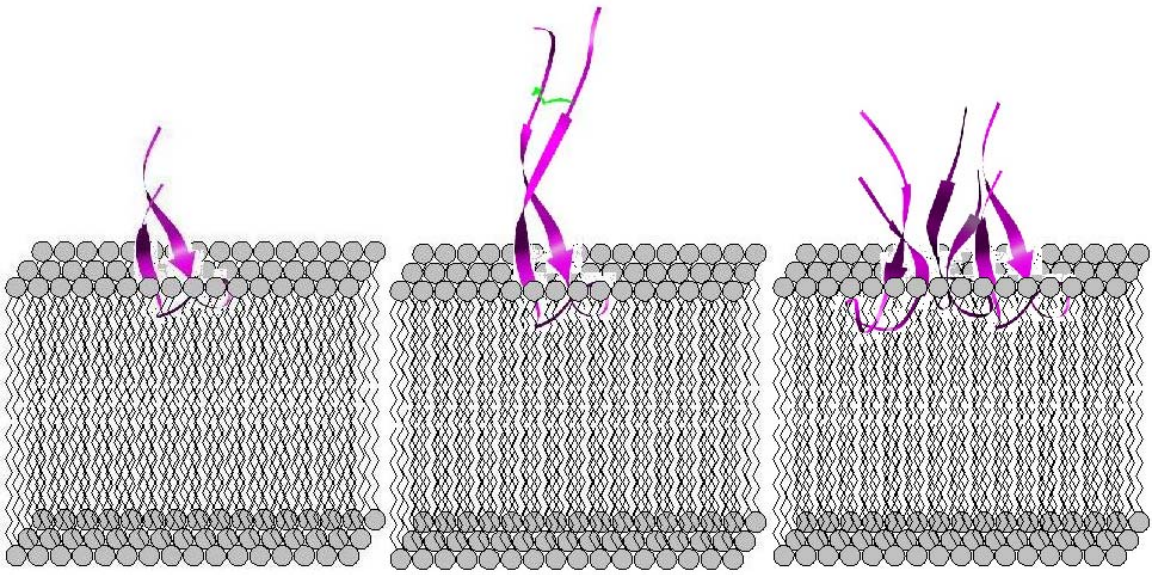

3.4 Experimental

3.4.1 Materials

Fmoc-protected amino acids, Wang resin, and HBTU were obtained from Advanced Chemtech. DMF, DCM, and acetonitrile were purchased from Fisher. HEPES, DIEA, TFA, thioanisole, phenol, EDT, TES, and cholesterol were purchased from Sigma-Aldrich. POPC, POPE, NBD-PE and Rh-PE were used as supplied from Avanti Polar Lipids. ^{13}CO labelled phenylalanine was obtained from Cambridge Isotope Laboratories, Inc. No purification was carried out for the experimental materials.

3.4.2 Peptide synthesis

Reduced TFPSS, TFPmn and TFPmnK were synthesized by following the optimized SPPS procedure as described in Chapter 2. In the cases of TFPtr and TFPtrK, a lysine side-chain scaffold was firstly synthesized, followed by a similar synthesis procedure to that used for the other peptides. Each peptide was cleaved from the resin with a 5 hr treatment with a mixture of 81.5% TFA, 5% thioanisole, 5% phenol, 5% ddH_2O, 2.5% EDT, and 1% TES.

The formation of disulfide bond in TFPSS was achieved by slowly stirring the

solution of 3 mg/mL reduced peptide in 0.1 M Tris-HCl buffer at pH 8.0, exposed to the air. The oxidation reaction was monitored by Ellman's assay. After stirred for 1 day, above 95% reduced peptide was oxidized. The peptide solution was lyophilized and dissolved in 0.1% TFA aqueous solution.

The synthesis of trimers began with coupling of 0.4 mmol Fmoc-β-Ala on 0.1 mmol Wang resin[105]. Sequent couplings of two Fmoc-Lys(Mtt) and one Fmoc-Lys(Boc) formed a lysine trimer backbone. After each addition of Fmoc-Lys(Mtt), the Mtt protection group was removed by a 1:5:94 mixture of TFA:TES:DCM. The 1% TFA deprotection cycle was repeated six times until the TFA solution remained colorless. After the trimer scaffold was completed by the addition of Fmoc-Lys(Boc), the synthesis was then continued on the synthesizer and the peptide was cleaved from the resin using the same cleavage procedure as in the synthesis of monomers.

Each of the peptides was purified by reversed-phase HPLC as described in Chapter 2. The elution time of TFPmn, TFPtr, TFPmnK, and TFPtrK was 27.0, 34.0, 25.4, and 31.8 min, respectively. The peptides showed a single peak by analytical reversed-phase HPLC (> 95% pure), and had the expected mass weight by characterized using MALDI-MS (Table 3.4).

3.4.3 Vesicle preparation

SUVs were prepared by sonicating lipids in 20 mM phosphate buffer for 3 hours.

Table 3.4 Percent yield and MALDI-MS characterization of the synthetic peptides.

Peptide	% Yield	Cal. Mass (Da.)	Obs. Mass (Da.)
TFPSS	**15**	**3217.6**	**3217.3**
TFPtr	**6**	**7278.8**	**7278.7**
TFPmn	**25**	**2286.9**	**2287.1**
TFPtrK	**5**	**9200.2**	**9219.8**
TFPmnK	**24**	**3055.5**	**3055.6**

LUVs were prepared by the extrusion method using a small-volume extrusion apparatus[52]. After a final trace amount of organic solvent was evaporated, the dried lipid film was suspended in 20 mM HEPES buffer. After 5 freezing and thawing cycles, the lipid suspensions were extruded by using an extruder 10 times through two stacked 0.l-μm-pore-size polycarbonate filters.

3.4.4 CD spectroscopy

CD spectra were measured using a Jasco J-810 spectropolarimeter. Spectra were recorded from 250 to 195 nm at a sensitivity of 50 millidegrees, resolution of 1 nm, response of 4 s, bandwidth of 1.0 nm, and a scan speed of 20 nm/min with 3 accumulations in order to increase the signal-to-noise ratio. The peptide concentration in

20 mM phosphate buffer was 50 μM. Phospholipid concentration of SUVs was 1 mM.

3.4.5 Tryptophan fluorescence spectroscopy

In this assay, the peptide-lipid mixtures were incubated at room temperature for 1 hr before data acquisition. Peptides TFPSS, TFPmn, TFPmnK, TFPtr and TFPtrK at 1, 1, 1, 0.3 and 0.3 μM concentrations, respectively, were diluted from stock solutions in 20 mM HEPES buffer. The lipid vesicles were prepared with an appropriate lipid composition. Corrected Trp emission spectra were acquired at 37 ℃ on a Varian Eclipse Fluorescence Spectrophotometer. Excitation of the indole ring was set at 280 nm.

3.4.6 FRET assay

Measurements were conducted at 37 ℃ using thermostated cuvettes with constant stirring, on a Varian Eclipse Fluorescence Spectrophotometer. LUVs containing 1 mol% of NBD-PE and Rh-PE were mixed with unlabeled LUVs at a 1:9 ratio in 2 ml HEPES buffer at pH 7.5. The total lipid concentration was 100 μM. The Rh-PE emission was monitored at 590 nm, with the excitation wavelength set at 465 nm. The fluorescence scale was calibrated such that the zero level corresponded to the initial residual fluorescence of the labeled vesicles and the 100% value to the fluorescence after addition of 20 μl of 10% (vol/vol) Triton X-100. Peptides TFPSS, TFPmn, TFPmnK, TFPtr and

TFPtrK at 5, 5, 5, 1.7 and 1.7 μM concentrations, respectively, were added from stock solution in 20 mM HEPES buffer. The pH was adjusted by adding the appropriate volume of a 1 mM HCl solution.

3.4.7 Photon correlation spectroscopy

Measurements were carried out on a Beckman Coulter N4plus photon-correlation spectrometer using 600 nm laser at 90^{o}[197]. The liposomes (total phospholipids, 26μM) were in 20 mM HEPES buffer. Synthetic peptides were added into the liposome solution to reach a final concentration of 26 μM for TFPSS, 26 μM for TFPmn, 26 μM for TFPmnK, 9 μM for TFPtr and 9 μM for TFPtrK, respectively. The vesicle sizes were measured after the liposome sample was incubated for half an hour. The fusion reaction was initiated by the addition of 1 M HCl to yield the desired pH.

3.4.8 ^{13}C CP/MAS solid state NMR

In the sample preparation protocol, a 2 mL TFPtr solution was prepared which contained 5 mg peptide in 20 mM HEPES buffer. The TFPtr solution was mixed with a 3.5 mL LUV solution with the final peptide-to-lipid ratios of 1:60. The mixed solution was kept at room temperature overnight, then ultracentrifuged at 20, 000 rpm for 5 hr at 4 ℃ to pellet the LUVs and associated bound peptide. A portion of the TFPtr/LUV pellet

formed after ultracentrifugation was transferred by spatula to a 6 mm diameter MAS NMR rotor.

^{13}C CP/MAS NMR experiments were carried out with a 6 mm triple-resonance MAS probe using Varian AS400 spectrometer operating at 100.2 MHz for ^{13}C. On average 20k scans, a spinning speed of 8 kHz, and a contact time of 1 ms[225-227] were accumulated. Decoupling was achieved using SPINAL-64 using a field strength of 90.9 kHz. The spectra were referenced to external adamantine, δ_{CH} = 29.50 ppm and δ_{CH_2} = 38.56 ppm relative to TMS[228].

Chapter 4: Structural studies of nanocrystalline cellulose films

4.0 Introduction

Chapter 1 introduced the different levels of cellulose structure and the methods to determine structures at the microscopic (using NMR) and macroscopic levels (using CD). Chapter 4 will apply these methods to determine the optical characteristics and the crystallinity of nanocrystalline cellulose (NCC) films prepared as a function of sample preparation variables, such as temperature, ionic strength, concentration, and the presence of an external magnetic field.

Section 4.1 of this chapter will outline the background and rationale for the structural studies of NCC films. Section 4.2 will focus on the structural analysis of the films and a discussion of the experimental results will also be presented. Section 4.3 will summarize the results from this chapter and provide some conclusions from the analysis of the experimental data. Finally, Section 4.4 will describe the experimental details.

4.1 Rationale for structural studies of NCC films

As introduced in Chapter 1, cellulose can adopt a range of structures, at different levels. This chapter will only focus on the studies of the chiral nematic structure (i.e.

pitch and handedness) and crystallinity of NCC films.

NCC is a material with unique strength and special optical and magnetic properties[229]. The individual crystallites are prepared using acid hydrolysis of cellulose containing materials, under strictly controlled conditions of time and temperature. Initially, the acid serves to remove the polysaccharide material which is bonded to the microfibril surface, resulting in an overall decrease of amorphous material. Subsequent hydrolysis breaks down those portions of the long glucose chains into accessible, non-crystalline regions and leaves highly crystalline regions of the original fibre. Hydrolysis is terminated by rapid dilution of the acid. This process is completed by a brief sonication to disperse the individual particles of cellulose and results in an aqueous suspension[6].

A chiral nematic, or cholesteric, structure contains stacked planes of molecules aligned along a director (*n*), with the orientation of each director rotated about the perpendicular axis from one plane to the next[230] (Figure 4.1). This structure is known to be a common structure formed spontaneously from solutions of rigid, rod-like molecules, for example, tobacco mosaic virus[231], poly(tetrafluoroethylene)[232], boehmite[233], and fd phage[234]. When the particles involved are optically active, a chiral nematic structure is formed. Colloidal suspensions of cellulose crystallites form chiral nematic structures upon reaching a critical concentration[6]. A chiral nematic pitch can be affected by adding electrolyte[235]. Chiral nematic structure whose pitch is on the order of the wavelength of visible light, reflects circularly polarized light (CPL)[8]. The wavelength of this selectively

reflected light changes with viewing angle, leading to an iridescent appearance. By simply casting films from suspensions of cellulose crystallites, cellulose films with the optical properties of chiral nematic structures can also be prepared[7]. Possible applications of the films include optically variable films and ink pigments for security papers, as the optical properties cannot by reproduced by printing or photocopying[9].

Figure 4.1 Schematic representation of the chiral nematic structure. Each pseudo-layer contains rod-like cellulose crystallites lining up parallel to each other, with the orientation of the rods in each layer being slightly different from those in the adjacent layers due to rotation of the director (*n*) about the perpendicular chiral nematic axis.

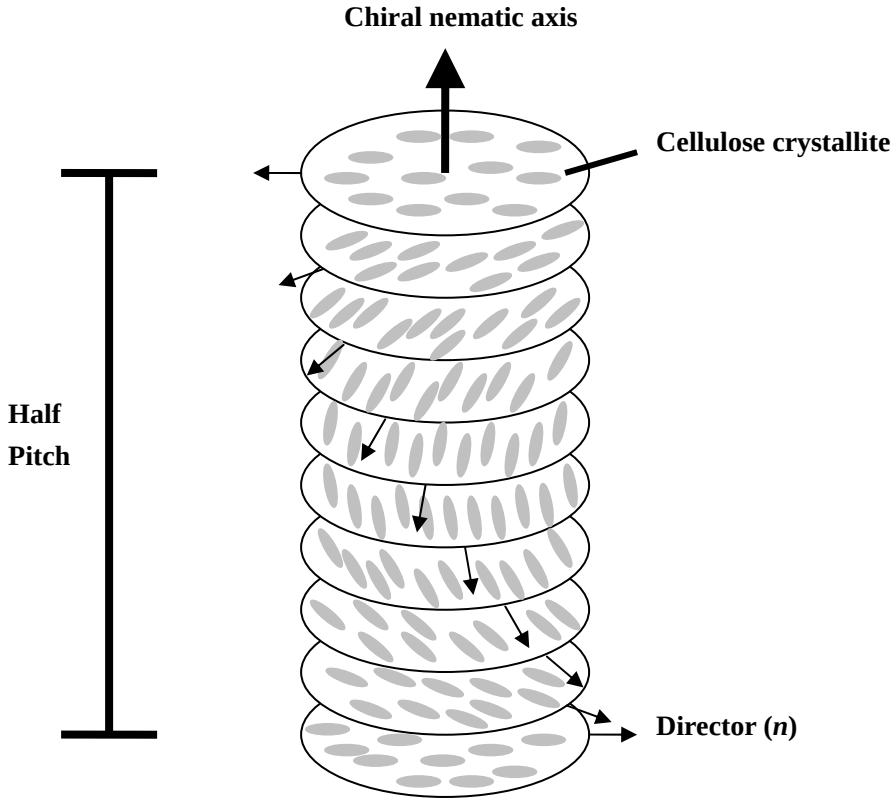

Crystallinity is another important structural characteristic of cellulose. It is defined as the crystalline fraction in the cellulose sample. As mentioned in Chapter 1, there are

ordered and disordered regions in cellulose crystallites, i.e. crystalline and amorphous domains, respectively. Hydrogen bonding between cellulose chains can stabilize local structure in cellulose and plays a role in the formation of crystalline domains[236]. The physical and chemical behavior of the cellulose is strongly influenced by its degree of crystallinity. For example, the crystallinity of cellulose directly influences the accessibility for chemical derivatization, swelling and water-binding properties[237].

Our approach was to produce NCC films from the colloidal suspensions under various conditions, such as drying the suspension with various amounts of added salt, drying the suspension at various cellulose concentrations, at different temperatures and in the presence of a strong external magnetic field. In this way, we sought to produce films with different optical properties and crystallinities, and tried to understand the effect of the above factors on the formation of chiral nematic structure and cellulose crystallinity in the NCC films in order to help us optimize the production of NCC films with predictable properties in the future.

4.2 Results and discussion

This section will start by describing the cellulose suspensions used to produce the films followed by the characterization of those films dried using CD, induced circular dichroism (ICD), polarized microscopy, and ^{13}C CP/MAS solid-state NMR.

4.2.1 Cellulose crystallites

The NCC samples used in this chapter were extracted from pulp fibers by using a variety of acid hydrolysis conditions (Proprietary information, FP Innovations Paprican). A total of seven samples were investigated, designated as S1 to S3, H1 and H2, and L1 and L2. The samples labeled S1, S2, and S3 were obtained using standard hydrolysis conditions, namely 64 % sulfuric acid at 45 ℃ for 25 minutes[238]. They were produced at different time points in the pilot plant and represented replicates. The samples H1 and H2 were obtained using hydrolysis where the acid concentration was 64 %, the temperature was 65 ℃ and the reaction time was 25 minutes. Finally, the L1 and L2 samples were obtained using the following conditions: 60 % sulfuric acid at 65 ℃ for 25 minutes. The original concentration of all these cellulose suspensions was 1.0 w%, except that of sample S1 which was 2.0 w%.

4.2.2 Chiral nematic structure

In order to characterize the chiral nematic structure of NCC, air-dried films of all samples described above were prepared, under different conditions: ionic strength in the suspension, suspension concentration, drying temperature, and magnetic field. The optical properties of the resulting films were characterized using CD spectroscopy, ICD spectroscopy and polarized microscopy, discussed in detail below.

4.2.2.1 CD spectroscopy

CD spectroscopy can be used to determine the handedness and pitch, which are the two major features of the chiral nematic structure. The orientation of pseudo-layers in a left-handed chiral nematic structure changes in an anticlockwise direction on moving away from the observer along the chiral nematic axis; the layers rotate clockwise in a right-handed chiral nematic structure. The chiral nematic pitch, *P*, which is the distance required for the pseudo-layers to complete one full rotation, is related to the wavelength of maximum reflection, λ, by equation 4.1:

$$\lambda = n\,P \tag{4.1}$$

where *n* is the average refractive index[8]. When the incident light is not normal to the surface of the crystallite, an angular dependence arises and the wavelength can be defined as

$$\lambda = n\,P\sin\varphi \tag{4.2}$$

where φ is the angle of incidence. Chiral nematic cellulose crystallites do not only reflect a particular wavelength of light, but also reflect selectively polarized light: right-handed cellulose crystallites reflect right-handed CPL and left-handed cellulose crystallites reflect left-handed CPL[23]. Therefore, the pitch and handedness of chiral nematic structure can be determined by CD spectroscopy. The CD signal, θ, is defined as the difference in absorption of left- and right-handed CPL:

$$\theta = A_L - A_R \tag{4.3}$$

where A_L is the absorption of left-handed CPL and A_R, the absorption of right-handed CPL[239]. The reflection of CPL appears as apparent absorption of the incident light. Thus, for chiral nematic samples that reflect visible light, the sign of the apparent CD signal resulting from the reflection of CPL gives the handedness of the chiral nematic structure. For example, if a chiral nematic sample predominantly reflects right-handed CPL, the light transmitted through the sample will be reduced by the amount of reflected light, resulting in the apparent absorption of the right CPL, but not of the left CPL. The CD signal will therefore be negative and will indicate a right-handed helical structure. Conversely, left-handed helices will give rise to positive CD signals[240].

4.2.2.1.1 NCC suspension

The experiments performed here start with a suspension of the NCC samples listed in Section 4.2.1. When dealing with suspensions, one has to keep in mind that these samples can spontaneously separate into phases. Previous studies have shown that there are critical concentrations for the phase separation[235, 241]. These concentrations are temperature dependent and can be predicted by theoretical calculations for cellulose crystallites[242-245]. At room temperature, there are two critical concentrations which are 5.14×10^{-6} nm^{-3} and 15.3×10^{-6} nm^{-3} and which have been verified experimentally[7]. These concentrations are the number density concentration *C* calculated from the weight percentage concentration *w*:

$$C = \frac{w}{[w + (100 - w)\rho]LD^2} \tag{4.4}$$

where ρ is the density of cellulose in water, L and D are the length and diameter of cellulose crystallites, respectively. When the total cellulose crystallite concentration is below 5.14×10^{-6} nm^{-3}, the suspension displays a single isotropic phase. As the total concentration rises above this first critical concentration, two phases appeared in the cellulose suspension, an upper isotropic phase and a lower anisotropic phase. The lower phase shows optical properties characteristic of chiral nematic structure. The fraction of the lower anisotropic phase increases with the total suspension concentration until, at the next critical concentration, the isotropic phase disappeared completely and the whole suspension becomes anisotropic[235].

The chiral nematic character of the cellulose suspensions studied here was determined by CD. In the CD spectrum of 2.0 w% cellulose suspension of S1 (Figure 4.2), for example, there was no obvious reflection peak in the observed region (250-700 nm). Thus, the 2.0 w% suspension of S1 was isotropic. The suspension was then sealed in a glass tube and kept standing vertically for one month. It did not separate into two phases. Therefore, the concentration of 2.0 w% is below the first critical concentration. The chiral properties of other NCC suspensions were also determined. They were all isotropic, and did not phase separate in the same time frame.

Figure 4.2 CD spectrum of 2.0 w% NCC suspension of sample S1.

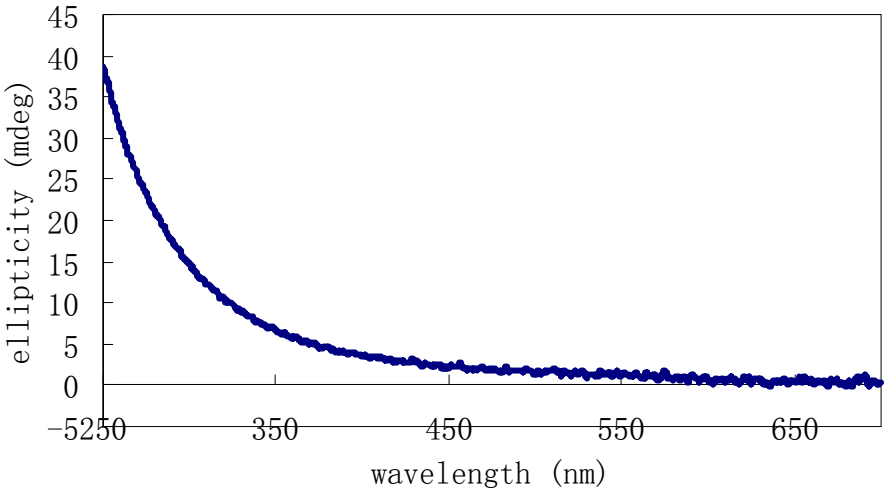

4.2.2.1.2 NCC film

The NCC films were firstly dried from colloidal cellulose suspensions using the original concentrations (1.0 or 2.0 w%) at room temperature. The chiral nematic properties of these films were determined by CD spectroscopy (Figure 4.3). For the S1, S2, and S3 films, a positive peak can be seen in the CD spectra, which indicates that the chiral nematic structures of cellulose crystallites in these films were left-handed. The experiments were performed with the incident light normal to the surface of the cellulose films. Using equation 4.1, the chiral nematic pitch was calculated for each film, using a refractive index $n \approx 1.5$[246] and found to be 317， 247, and 231 nm, for the S1, S2, and S3 films, respectively. These cellulose crystallites were produced using the same procedure, but their films had different chiral nematic structure. This may be due to differences in

the original concentration of the cellulose suspensions (S1 was 2.0 w%, while S2 and S3 were 1.0 w%) or in how the batches were processed in the pilot plant. The effect of suspension concentration on the chiral nematic properties of cellulose films will be discussed in Section 4.2.2.1.2.2. The films produced from the H1, H2, L1, and L2 samples did not give rise to reflection peaks in the CD spectra, indicating that either the chiral nematic properties of these films were very weak or that the maximum reflection was out of the observation range. The lack of a significant chiral nematic phase for these samples is supported by results from previous studies, which suggested that the iridescence of films generated from H1, H2, L1, and L2 was affected by the hydrolysis conditions in the sample preparation. The handedness of these films will be further discussed in Section 4.2.3.

Figure 4.3 CD spectra of cellulose films produced from S1 (dark blue), S2 (pink), S3 (red), H1 (black), H2 (violet), L1 (dark red), and L2 (green) suspensions at original concentrations of 1.0 w% (or 2.0 w% for S1), at room temperature.

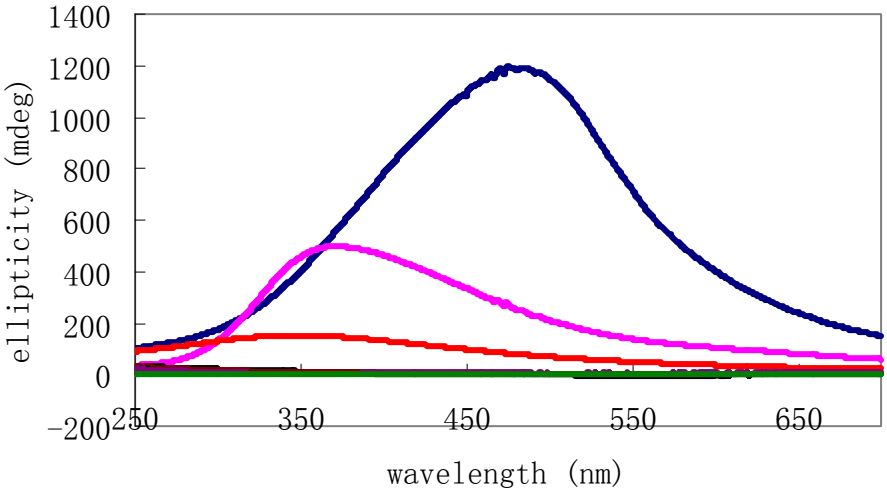

4.2.2.1.2.1 Effect of ionic strength

The ionic strength can affect the formation of the anisotropic phase in a cellulose suspension[235]. With increasing electrolyte concentration, the critical concentration of spontaneously forming anisotropic phase increases, and the pitch and the volume fraction of the anisotropic phase in the biphasic cellulose suspension decreases. In our work, the formation of chiral nematic structure in NCC films was studied as a function of added electrolyte (NaCl) concentrations. The suspension of sample S1 was used to produce the films. The original 2.0 w% suspension was diluted to 1.0 w% and an appropriate amount of a 10 mM NaCl stock solution was added to achieve the desired electrolyte concentration before evaporation. The positive reflections shown in Figure 4.4.a indicated that films prepared from S1 samples had left-handed chiral nematic structure, and the ionic strength in the suspension did not influence the handedness. As the concentration of added NaCl increased, the maximum reflection shifted to shorter wavelength, indicating that the chiral nematic pitch of the resulting film decreased as a linear function of added salt concentration (Figure 4.4.b). When the concentration of added NaCl reached 0.5 mM, there was no peak in the observed CD range, indicating that under this condition the film did not have iridescence in the visible light region. The effect of NaCl on the formation of chiral nematic structure in NCC films might result from two factors: (1) a decrease in the electrical double layer thickness at higher ionic strength increases the chiral interactions between the crystallites, thus decreasing the

Figure 4.4 (a) CD spectra of cellulose films produced from 1.0 w% suspensions of S1 with 0 (dark blue), 0.1 (pink), 0.2 (red), 0.3 (black), 0.4 (violet), and 0.5 mM (dark red) NaCl at room temperature. (b) Plot of the calculated chiral nematic pitches of S1 cellulose films as a function of the concentration of added NaCl. The error bars represent the wavelength range of 98% of the maximum reflection ellipticity in the CD spectra.

(a)

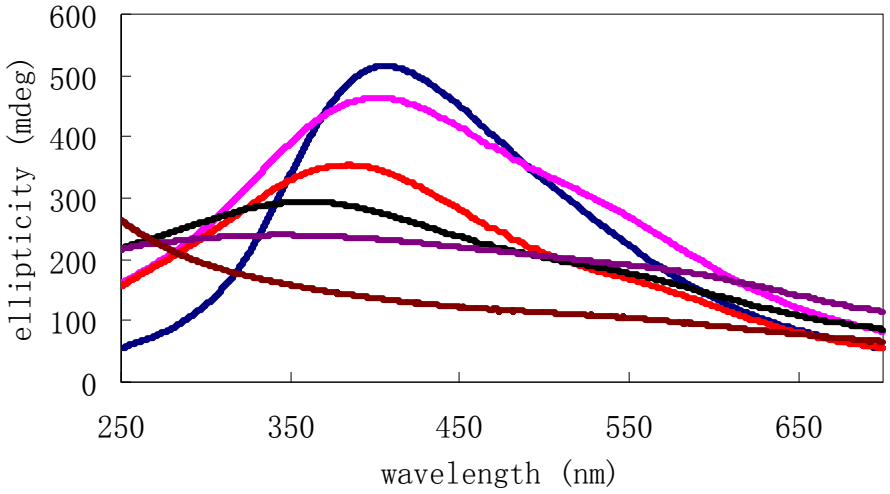

(b)

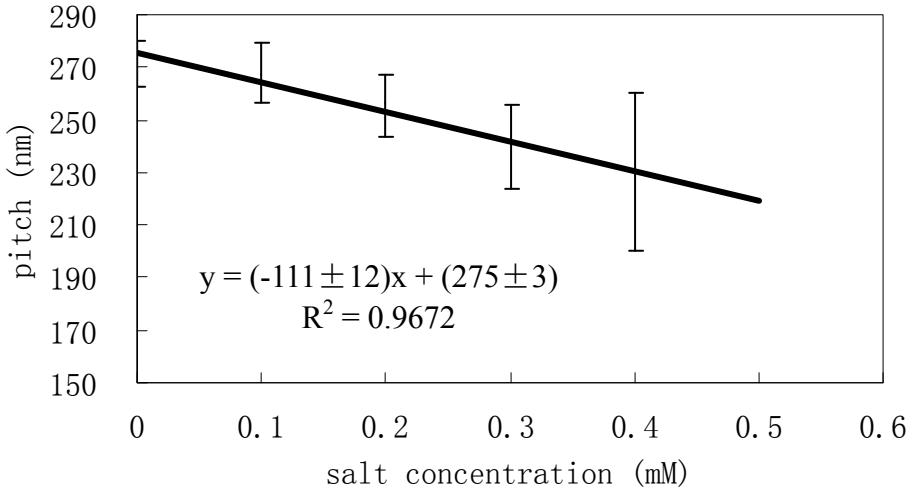

chiral nematic pitch[235]; and (2) the high salt concentration shifts the critical concentration to higher values[235], making it more difficult for the anisotropic phase and thus the chiral nematic structure to form.

4.2.2.1.2.2 Effect of suspension concentration

Studies on the chiral nematic structure of solutions of poly-γ-benzyl-*L*-glutamate, poly-γ-benzyl-*D*-glutamate and poly-γ-alkyl-*L*-glutamate have shown that the chiral nematic pitch (*P*) depends on the concentration (c) of the polymer, according to

$$\ln(1/P) = k \ln(c) + A \qquad (4.5)$$

where *A* is a constant dependent on the solvent, temperature and the molecular weight of the solute polymer and k is typically below 2 and is solvent dependent[247, 248]. This relationship has not been applied to cellulose yet, but the effect of suspension concentration on chiral nematic order has been observed for cellulose derivatives[249]. We have therefore investigated the effect of suspension concentration on the chiral nematic phase using the cellulose sample S1 and tried to use equation 4.5 to fit our data. The original 2.0 w% cellulose suspension of sample S1 was diluted to the following series of concentrations: 0.1, 0.2, 0.5, and 1.0 w%. The suspensions were dried at room temperature. To ensure that the films consisted of the same amount of material, 400 μL of the 0.5 w% suspension, 200 μL of the 1.0 w% suspension and 100 μL of the 2.0 w% suspension were used. Deionized water at pH 6.3 was used to dilute the sample,

minimizing any potential contribution arising from the presence of electrolytes (as outlined in the previous section).

The CD spectra (Figure 4.5.a) of the resulting films showed a positive peak for the films produced from 0.5, 1.0, and 2.0 w% suspensions, but no obvious peak was observed for the films produced starting from 0.1 and 0.2 w% suspensions. These observations indicated that the chiral nematic structure of the films produced from 0.5, 1.0, and 2.0 w% suspensions was left-handed. In other words, dilution did not change the handedness of the S1 films. The pitch, on the other hand, increased as a function of increasing concentration. Figure 4.5.b shows that equation 4.5 can be fit to the experimental data very well. In summary, this suggests that the concentration of suspension has an effect on the chiral nematic structure formed in the NCC films. When the sample is dilute, it may take longer for the anisotropic phase, and therefore the chiral nematic structure to form.

4.2.2.1.2.3 Effect of temperature

Previous studies have shown that temperature can influence the chiral nematic structure in the suspension of cellulose derivatives[250, 251]. Depending on the different substitutions and the degree of substitution of the cellulose, the effect is varied. A statistical theory for the chiral nematic ordering of polypeptide solutions has been used to predict the temperature dependent pitch (P) of the chiral nematic structure in cellulose

Figure 4.5 (a) CD spectra of cellulose films produced from S1 suspensions with the concentrations of 0.1 (dark blue), 0.2 (pink), 0.5 (red), 1.0 (black), 2.0 w% (violet) at room temperature. (b) Plot of ln(1/*P*) of S1 cellulose films against ln(c) of cellulose crystallites. The error bars represent the wavelength range of 98% of the maximum reflection ellipticity in the CD spectra.

(a)

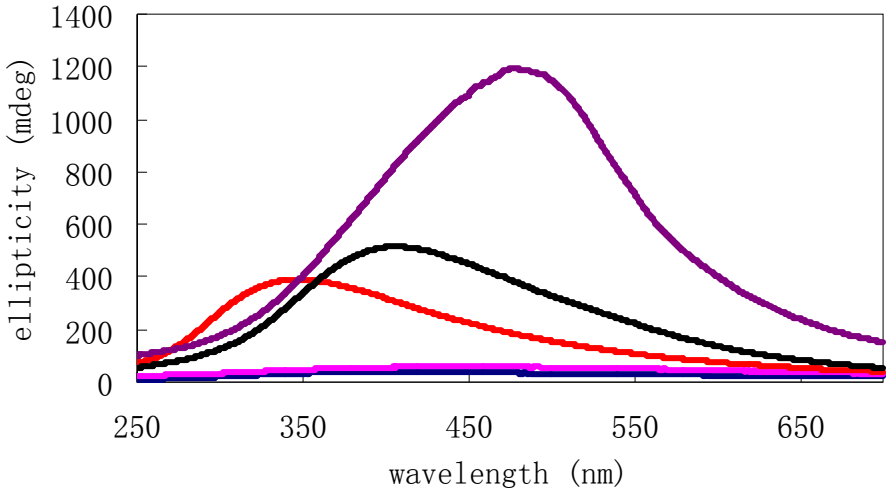

(b)

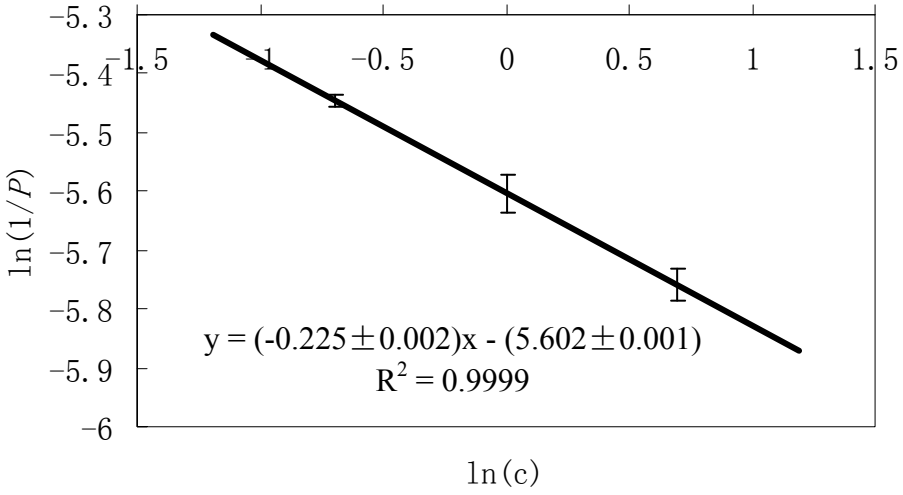

derivative solutions[248]:

$$\frac{1}{P} = B\left(\frac{T_N}{T} - 1\right) \tag{4.6}$$

where T is temperature, B is a constant which is a function of the solution concentration and the molecular weight of the solute polymer, and T_N is the compensation temperature, defined as the temperature at which the pitch is infinite.

To our knowledge, the effect of temperature on the chiral nematic structure in pure cellulose samples has not been determined to date. In order to investigate the effect on formation of chiral nematic structure in NCC films, crystallite suspension S1 at a concentration of 2.0 w% was dried at various temperatures. The evaporation temperature of 4 ℃ was achieved by drying the sample in the fridge. Other samples were dried in an incubator with the temperature set at 40, 50, 60, or 70 ℃. A positive peak was shown in the CD spectra of all the films (Figure 4.6.a), indicating that the handedness of these films was left-handed and independent of temperature. However, the wavelength of maximum reflection changed as a function of the drying temperature. A plot of the inverse pitch as a function of reciprocal temperature (Figure 4.6.b) yielded a straight line, as predicted by equation 4.6[248]. T_N, as evaluated from the extrapolation of the plot to infinite pitch, was -67 ℃. Since temperature has an impact on the diffusion and evaporation rates, the results suggest that the rate at which cellulose crystallites come together to form a chiral nematic phase is directly related to the pitch of chiral nematic phase formed in the films.

Figure 4.6 (a) CD spectra of cellulose films produced from 2.0 w% S1 suspensions at 4 (dark blue), 22 (pink), 40 (red), 50 (black), 60 (violet), and 70 °C (dark red). (b) Plot of reciprocal pitch of S1 films as a function of reciprocal drying temperature. The error bars represent the wavelength range of 98% of the maximum reflection ellipticity in the CD spectra.

(a)

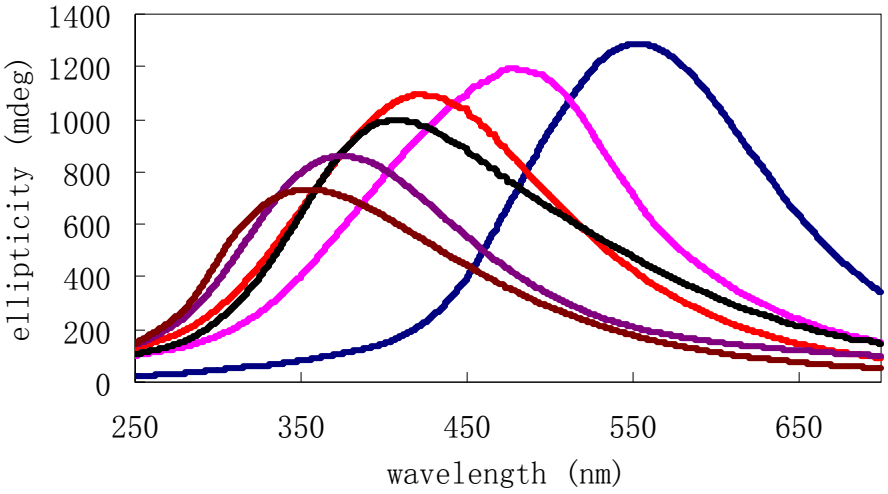

(b)

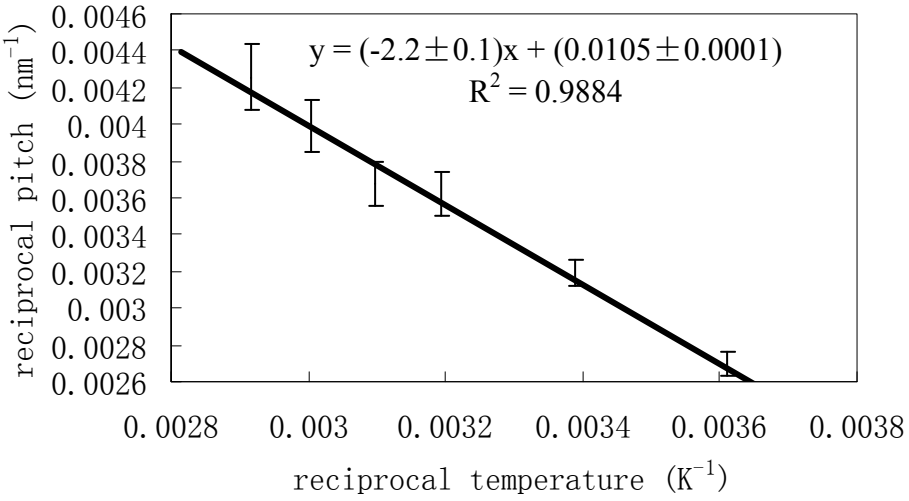

4.2.2.1.2.4 Effect of magnetic field

Magnetic field is a useful means of processing weakly magnetic materials[252]. When a weakly magnetic particle is subjected to a magnetic field gradient, the particle receives a magnetic force so that it is pushed toward the location where the field strength is weak or strong depending on its magnetic nature. If a particle has magnetic anisotropy, it undergoes magnetic alignment. When a suspension of cellulose crystallites is allowed to dry in a homogeneous magnetic field, the crystallites exhibit an alignment with their long axes perpendicular to the direction of the field, indicating a negative diamagnetic susceptibility anisotropy[253]. In other words, the chiral nematic axis is parallel to the external magnetic field applied[254, 255]. This section will focus on studying the effect of magnetic filed on the chiral nematic structure of the NCC films.

The chiral nematic structure of the NCC films produced in a magnetic field was studied by drying S1 suspensions using a series of concentrations on glass slides. Since the glass slides were kept perpendicular to the direction of the external magnetic field, the chiral nematic axis is perpendicular to the surface of the glass slides. As shown in Figure 4.7.a, the CD spectra of S1 films produced from 0.5, 1.0, and 2.0 w% suspensions had a strong positive peak, indicating that the chiral nematic phase was left-handed, while the CD spectra of the films produced from 0.1 and 0.2 w% suspension did not yield any apparent peaks, indicating that they possessed little chiral nematic structure. For the films with chiral nematic structure, the wavelength of the maximum reflection increased as the

Figure 4.7 (a) CD spectra of cellulose films produced from S1 suspensions with the concentration of 0.1 (dark blue), 0.2 (pink), 0.5 (red), 1.0 (black), and 2.0 w% (violet) in a 9.7 T magnetic field at room temperature. (b) Plot of ln(1/*P*) of S1 cellulose films made in the magnetic field against ln(c) concentration of cellulose crystallites. The error bars represent the wavelength range of 98% of the maximum reflection ellipticity in the CD spectra.

(a)

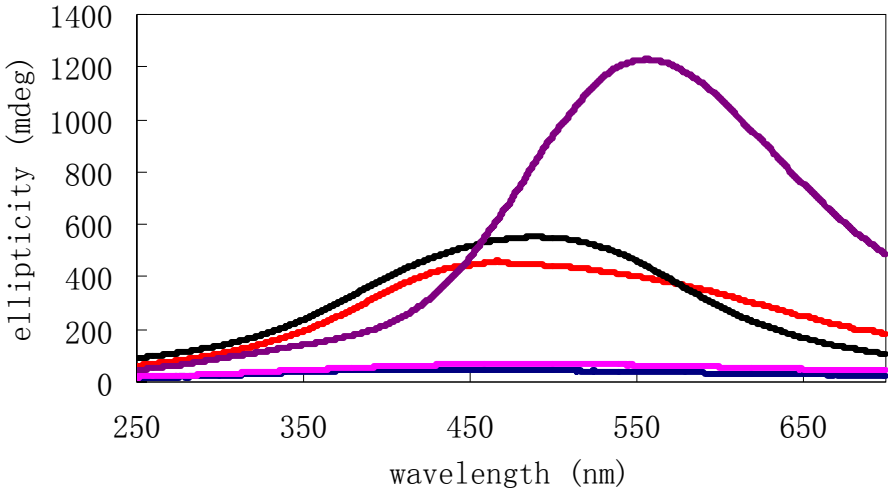

(b)

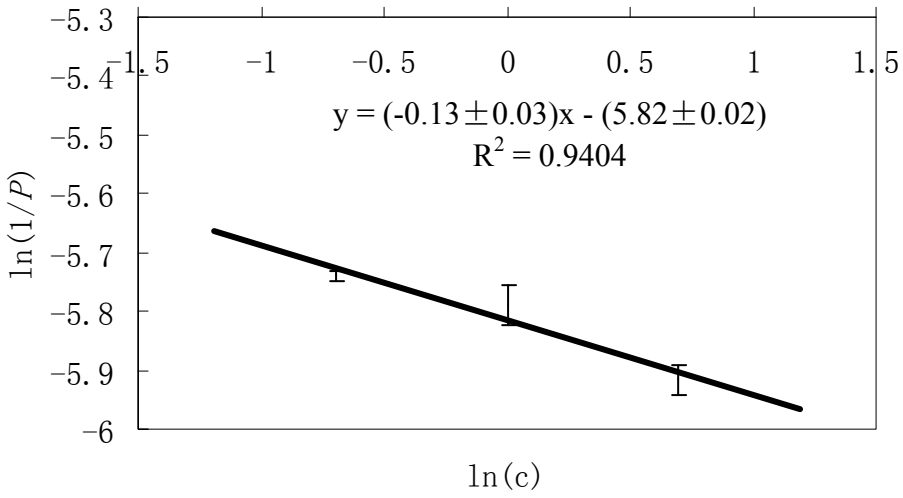

original suspension concentration increased. These data can also be fitted using equation 4.5 (Figure 4.7.b), but in this case the functional form is different. For the films dried outside the magnetic field, the value of *A* was -5.60 and the value of k was -0.23; while for the films dried in the magnetic field, the values were -5.82 and -0.13 for *A* and k, respectively. In both cases, the values of *A* were similar. Because *A* is a constant dependent on the solvent, temperature and the molecular weight of the solute polymer, the applied magnetic field did not dramatically affect this constant. However, the magnetic alignment significantly changed the k value. Table 4.1 shows a comparison of the chiral nematic pitch of the films produced in and out of the magnetic field. For the films produced from suspensions with the same concentration in the 0.5-2.0 w% range, the calculated chiral nematic pitch increased when the samples were dried in the presence of a magnetic field. The magnetic field did not help to reintroduce the chiral nematic phase in suspensions of low concentrations (0.1-0.2 w%), as there was still no detectable iridescence in the visible range. These observations indicate that the magnetic field did not influence the formation of chiral nematic structure, but only had an effect on the pitch of the resulting films. The increase in chiral nematic pitch was probably due to the magnetic alignment of cellulose crystallites, which might cause the tilt angle between the directions of directors in adjacent pseudo-layers to decrease.

The chiral nematic structure of NCC films was also studied as a function of exposure time in the magnetic field. In order to control the drying time of the cellulose suspension in the magnetic field, we have made use of two drying protocols, designated as fast and

Table 4.1 Comparison of the chiral nematic pitch obtained for films produced in and out of a magnetic field. The pitch is calculated based on the CD data in Figures 4.5.a and 4.7.a.

Concentration (w%)	Pitch (nm)	
	In a magnetic field	Out of a magnetic field
0.5	311	232
1.0	327	271
2.0	371	317

slow evaporation. In the fast evaporation, the cellulose suspension was directly dried in the surrounding atmosphere (e.g. 100 μL NCC suspension was dried in 0.5 hr). In the slow evaporation, the evaporation process was slowed down by covering the sample with a petri dish. In this case, the same volume of NCC suspension took about 8 hr to dry. Using these protocols, the 2.0 w% S1 suspension was dried in a 9.7 T magnetic field for 0.5, 2.5, 4.5, 6.5, or 8.0 hr. The CD spectra of these films are shown in Figure 4.8.a. There was a positive peak in all the CD spectra, indicating the handedness of the films remained left-handed as the exposure time in the magnetic field increased. Moreover, the maximum reflection shifted to longer wavelengths as the drying time increased. These data were fitted by two linear functions, yielding the relation between the chiral nematic pitch and drying time in the magnetic field shown in Figure 4.8.b. The data suggests that the cellulose crystallites exposed to the magnetic field for the longest time can better align than those exposed for only a short time. It is also possible that the shorter drying

Figure 4.8 (a) CD spectra of cellulose films produced from 2.0 w% S1 suspensions exposed to a 9.7 T magnetic field for 0.5 (dark blue), 2.5 (pink), 4.5 (red), 6.5 (black), and 8.0 hr (violet) at room temperature. (b) Plots of the calculated chiral nematic pitches of S1 cellulose films against the drying time in a 9.7 T magnetic field. The error bars represent the wavelength range of 98% of the maximum reflection ellipticity in the CD spectra.

(a)

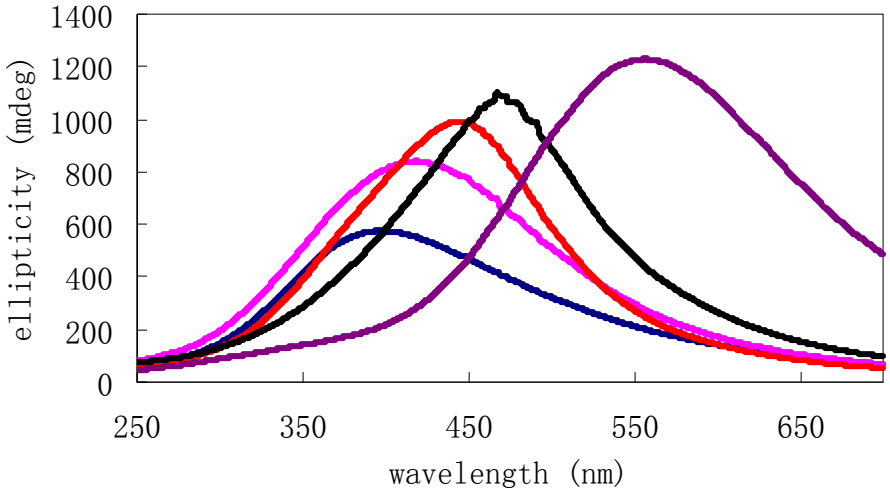

(b)

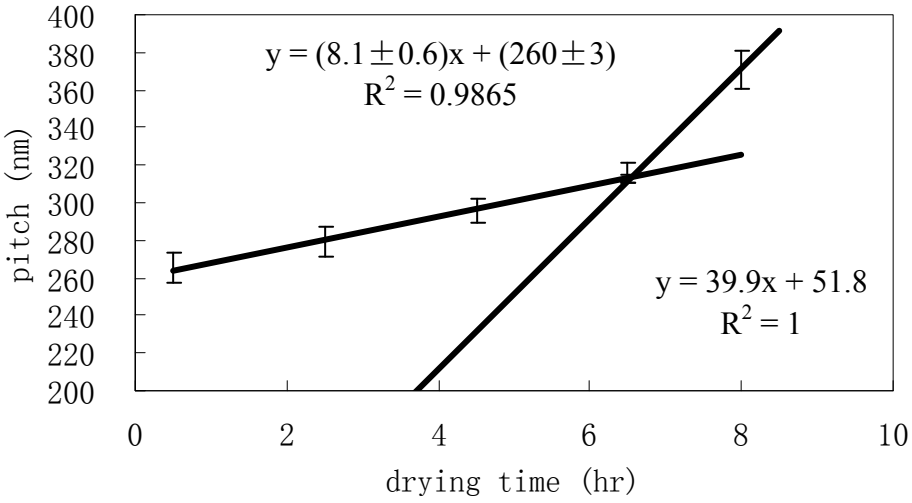

times are such that the film may dry completely before the equilibrium of the formation of an anisotropic phase in the suspension can reach. The reason for the sudden pitch change after the drying time of 6 hr is not clear and would require further study.

The effect of the magnetic field on the chiral nematic structure of NCC films was also studied by drying S2, S3, H1, H2, L1, and L2 suspensions. The CD spectra of the films produced in and out of the 9.7 T magnetic field are shown in Figure 4.9. There was a positive peak in the CD spectra of S2 and S3 films, indicating the left-handed chiral nematic structure in those films. The maximum reflection shifted to the longer wavelength after the magnetic field was applied, indicating that the chiral nematic pitch increased. By drying in the magnetic field, the calculated pitch changed from 247 nm to 285 nm, and from 231 nm to 251 nm, for the S1 and S2 NCC films, respectively. This is similar to the trends observed for the NCC sample S1 (Table 4.1). On the other hand, the CD spectra of the films prepared from H1, H2, L1, and L2 samples did not show any apparent peaks, indicating their chiral nematic properties were too weak to be determined by CD spectroscopy. The handedness and chiral nematic pitch of these films will be discussed in the next section.

4.2.2.2 ICD spectroscopy

ICD spectroscopy is a method to determine the chiral nematic character of cellulose crystallites, which have no chromophores that absorb the light in regions easily accessible

Figure 4.9 CD spectra of cellulose films produced from 1.0 w% (a) S2, (b) S3, (c) H1, (d) H2, (e) L1, and (f) L2 NCC suspensions. The CD spectra of the cellulose films produced in or out of the magnetic field are dark blue or pink, respectively.

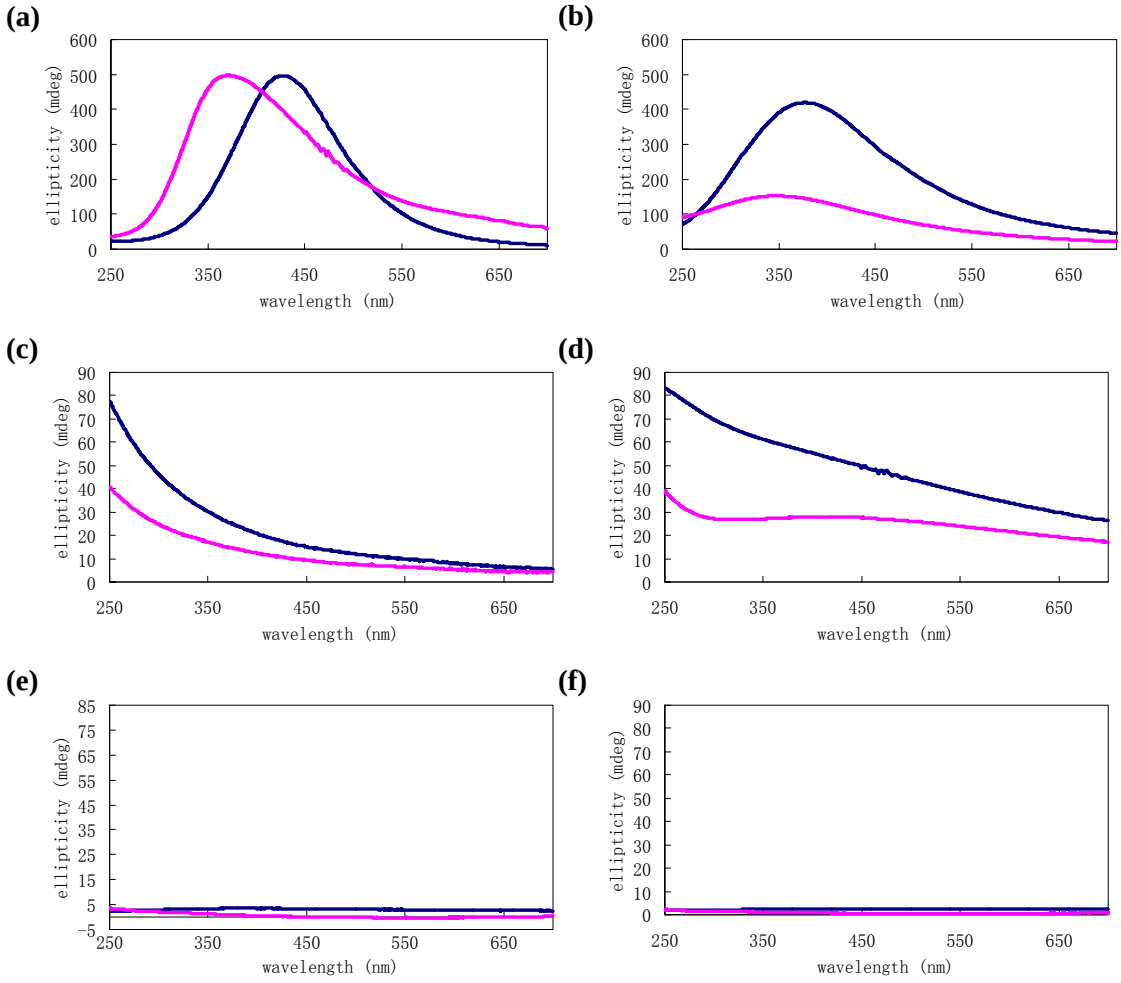

to most spectropolarimeters. In this case, instead of trying to directly measure the CD spectra of these cellulose crystallites in the far UV range, a CD signal may be induced by the association between a CD inactive chromophore and the chiral cellulose structure. The ICD response may arise due to a covalent link between the cellulose backbone and the chromophore or alternatively, via a strong specific physical interaction between the chromophore and the polymer chain. To determine the handedness of the chiral nematic

structures from ICD spectroscopy, the ratio of λ_0, the wavelength of the chiral nematic reflection band, to λ_{ab}, the wavelength of dye absorption, must be known. For $\lambda_0/\lambda_{ab} < 1$, a negative ICD spectrum indicates a left-handed arrangement and a positive ICD spectrum, a right-handed arrangement. The opposite is true for $\lambda_0/\lambda_{ab} > 1$[246]. This relation between the sign of the ICD signal and the position of the chiral nematic reflection band is supported by experimental measurements[246, 256] and theoretical calculations[257]. In addition, previous studies have shown that the ICD intensity depends on the chiral nematic pitch, temperature, and texture[246].

Since there was no apparent peak shown in the CD spectra of the films prepared from the H1, H2, L1, and L2 samples, the chiral nematic properties of these films were studied by ICD spectroscopy. The suspensions of H1, H2, L1, and L2 samples were doped with 100 μL of 1 mM Trypan blue, which is an optically inactive dye with an absorption at 590 nm. The films were prepared by drying the cellulose suspension in or out of the 9.7 T magnetic field, under the same conditions as above. Only the films prepared from L1 and L2 suspensions yielded large ICD signals (Figure 4.10.a and 4.10.b). The ICD peak occurred at the maximum absorbance wavelength of Trypan blue, suggesting that the dye molecules were in a chiral environment. This chirality could be achieved if the dye molecules have aligned their long axes parallel to the long axes of the cellulose crystallites, thereby also forming a supermolecular helical (chiral) array. The detection of an ICD peak confirmed that the chiral nematic structure was formed in the solid films. Since the chiral nematic reflection band was at a smaller wavelength than the

Figure 4.10 ICD spectra of cellulose films produced from 1.0 w% NCC suspensions doped with 9.6 × 10^{-5} g Trypan blue. (a) and (b), films produced from L1 and L2 suspensions without salt added, respectively. (c), (d), (e), and (f), films produced from H1, H2, S2, and S3 suspensions with an appropriate amount of salt, respectively. The CD spectra of the cellulose films produced in or out of the magnetic field are represented in dark blue or pink, respectively.

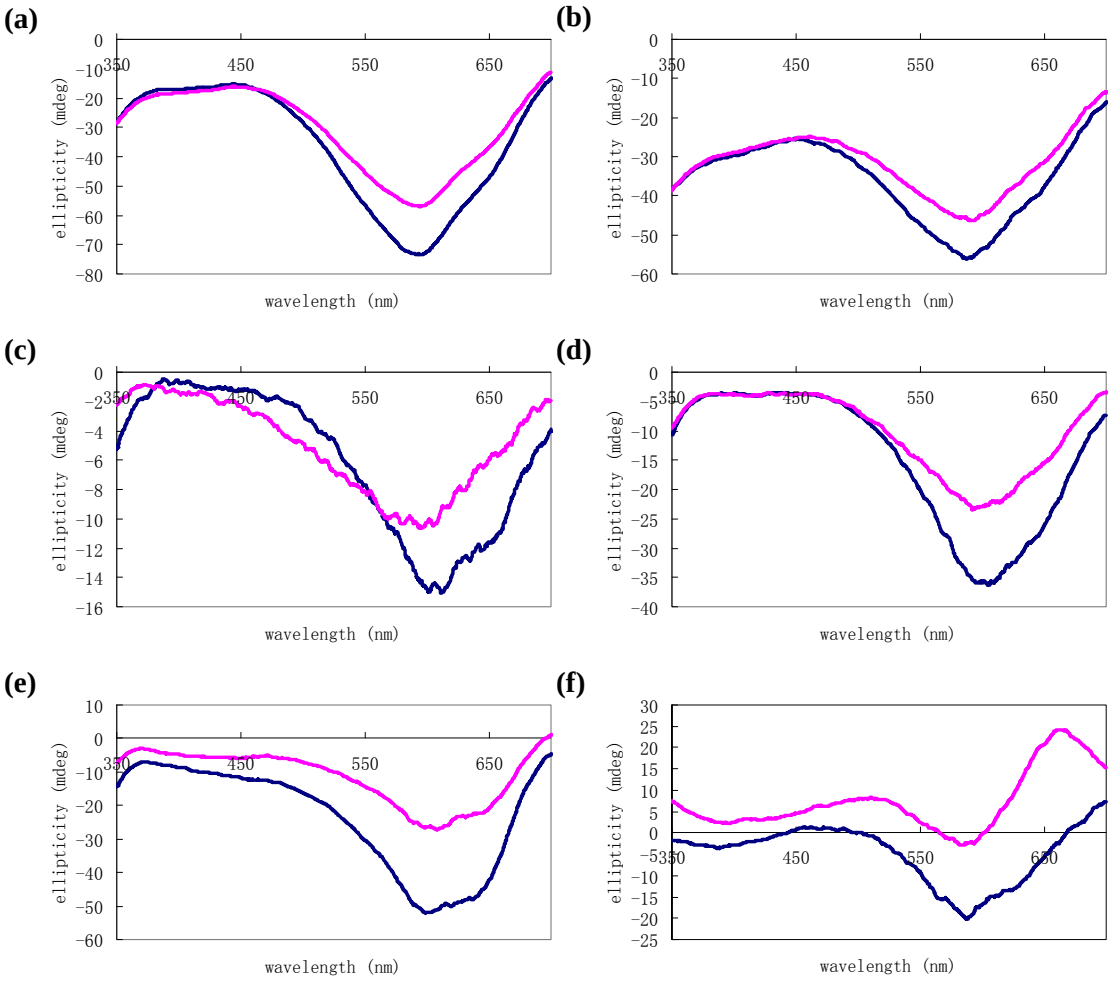

dye absorption band, $\lambda_0/\lambda_{ab} < 1$, the observed negative ICD peak indicated a left-handed chiral nematic structure for L1 and L2 films. On the other hand, the films prepared from H1 and H2 suspensions did not yield a strong ICD signal (data not shown). There were two distinct optical effects occurring in these doped films: the reflection of CPL due to

chiral nematic structure and the absorption of CPL due to the presence of dye molecules in a chiral environment. Because of the imperfect orientation of the chiral nematic phase[258] in the films of the H1 and H2 cellulose samples, the films had wide reflection band peaks as shown in Figure 4.9.c and 4.9.d, respectively. Thus, the reflection band of the films in the visible region overlapped with the absorption peak of the dye. To circumvent this problem, an appropriate amount of NaCl was added to the samples to partially destroy the chiral nematic structure. The resulting ICD signals of the H1 and H2 films (Figure 4.10.c and 4.10.d) were obtained by adding 40 μL 0.01 M NaCl and 12 μL 0.1 M NaCl in the H1 and H2 cellulose suspensions, respectively. There was a negative peak at the absorption wavelength of the dye, indicating that these films had left-handed chiral nematic structure. ICD spectra of the films prepared from S2 and S3 samples (Figure 4.10.e and 4.10.f) were also obtained by adding 15 μL and 13 μL 0.1 M NaCl in the S2 and S3 cellulose suspensions, respectively. The negative peak shown in the ICD spectra indicated that the handedness of the films prepared from the S2 and S3 samples was left-handed, consistent with the results from CD spectroscopy. Overall, the ICD spectra obtained for the films prepared in the magnetic field showed more negative ellipticities. Measurements performed using a UV-visible spectrometer showed that the total absorbance at 590 nm was very similar for all of the films prepared. Therefore, the increase in ICD peak intensity can indeed be attributed to an increase of the chiral nematic pitch due to the magnetic alignment of the cellulose particles, a finding which is consistent with the results discussed earlier.

4.2.2.3 Polarized microscopy

Polarized microscopy can provide direct evidence of the chiral nematic structure of NCC films. The polarized light microscope is designed to observe and photograph specimens that are visible primarily due to their optically anisotropic character. If the specimens have chiral nematic structure, a fingerprint texture and iridescence will be observed. The fingerprint texture corresponds to the birefringent multidomains with superimposed extinction contours seen in the optical micrographs, whereas iridescence manifests itself as a color change. The spacing between the periodic lines in the fingerprint texture corresponds to half of the cholesteric pitch (*P*).

Figures 4.11 and 4.12 show optical micrographs of the films made from the suspension S1 dried at 70 and 4 ℃, respectively. The fingerprint texture confirmed the presence of chiral nematic structure, and the longer distance between the periodic lines in the film prepared at lower temperature indicated that the pitch of the film is longer. The micrographs of the films prepared from the suspension S1 dried in the magnetic field for 0.5 and 8 hr (Figures 4.13 and 4.14), indicated that the increase of exposure time in the magnetic field resulted in a film with longer distance between the periodic lines. These results were consistent with the CD experiments. However, for the S2 films prepared in or out of the magnetic field (Figures 4.15 and 4.16), the difference was less obvious. The reason might be that the change in chiral nematic pitch of S2 films due to the magnetic alignment of the cellulose crystallites was only 38 nm (determined by CD spectroscopy),

Figure 4.11 Optical micrograph of a film prepared from NCC suspension S1 at 70 °C. The magnification was 40X.

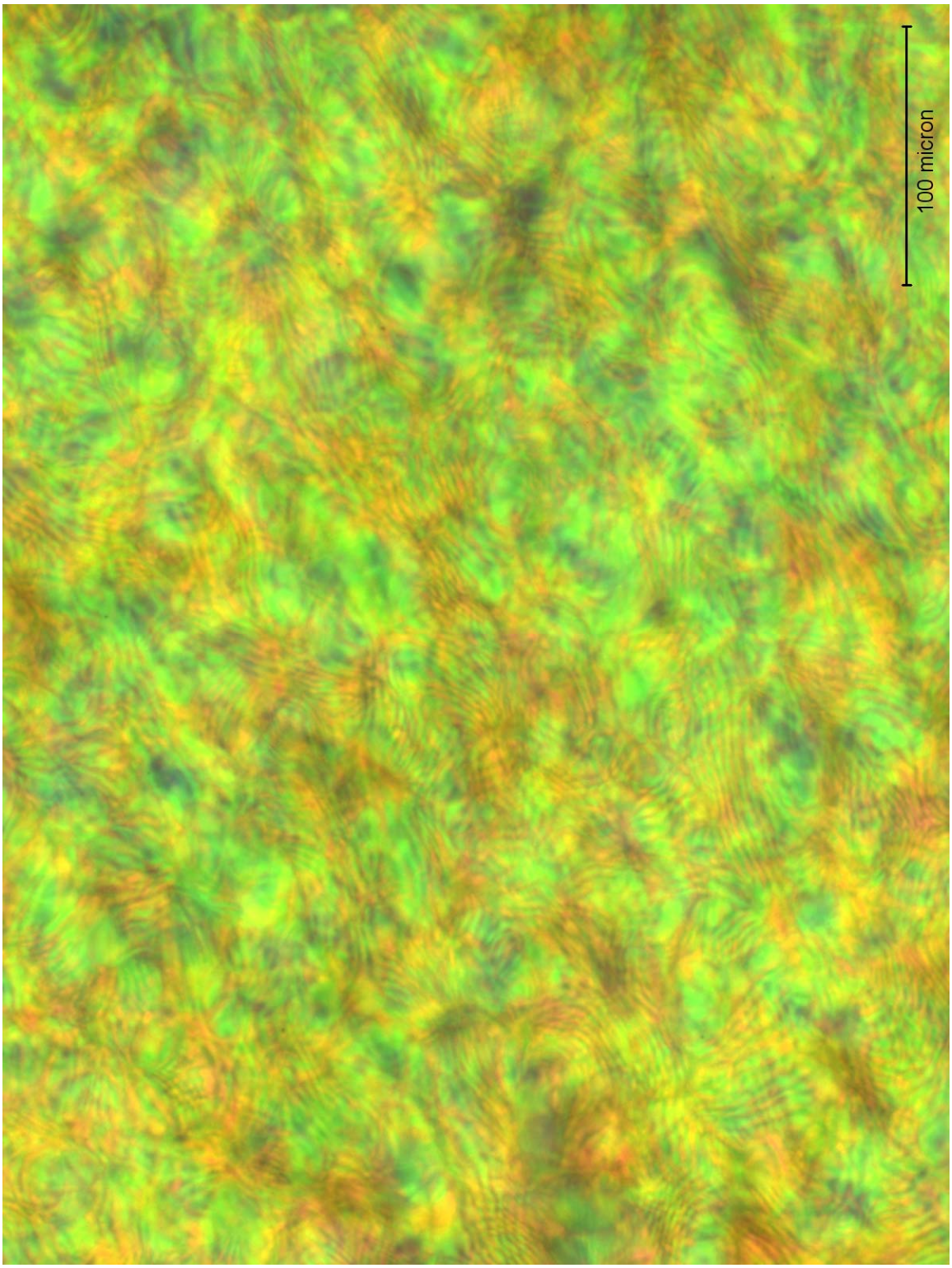

Figure 4.12 Optical micrograph of a film prepared from NCC suspension S1 at 4 °C. The magnification was 40X.

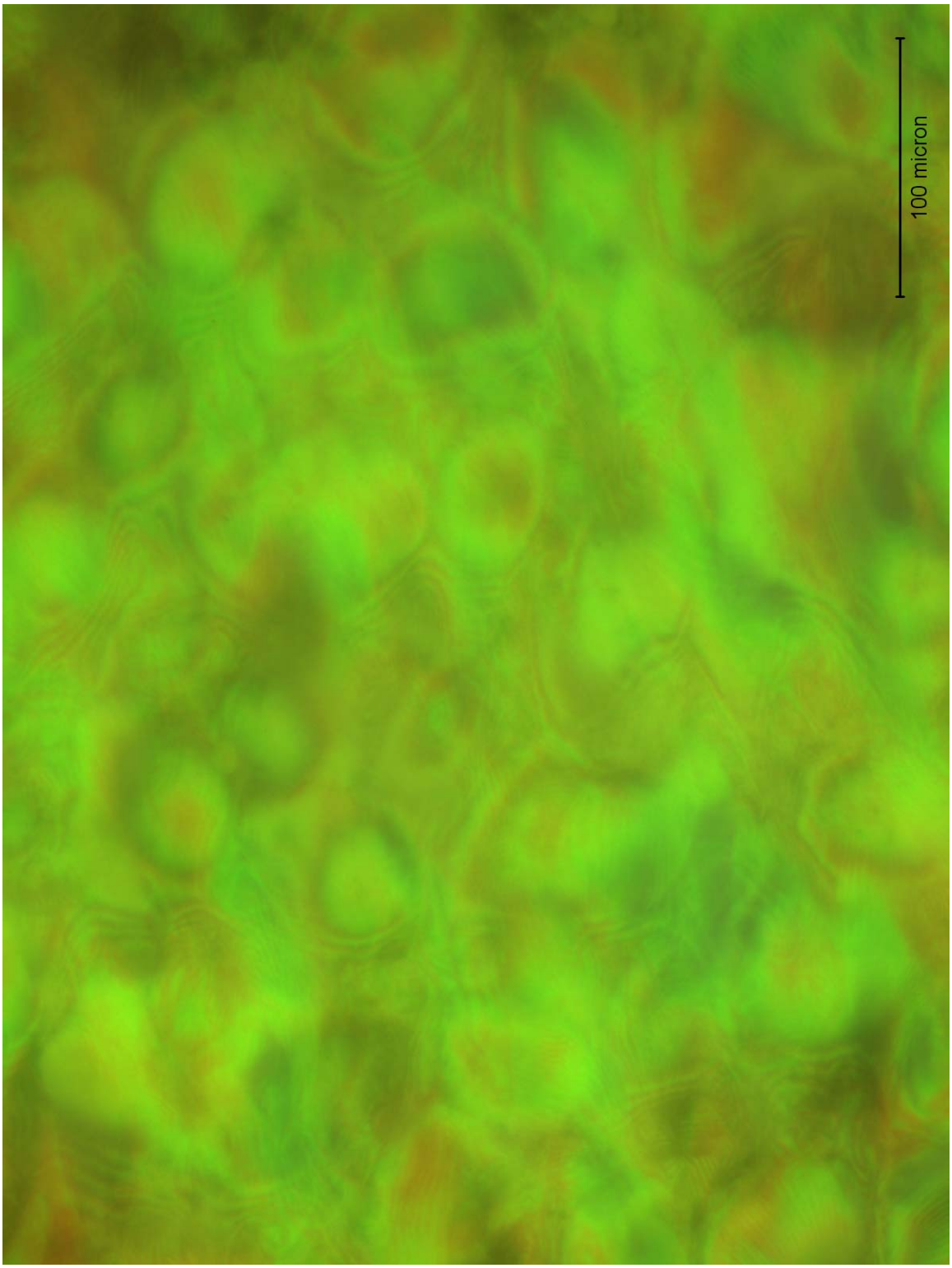

Figure 4.13 Optical micrograph of a film prepared from NCC suspension S1 dried in a 9.7 T magnetic field for 0.5 hr. The magnification was 40X.

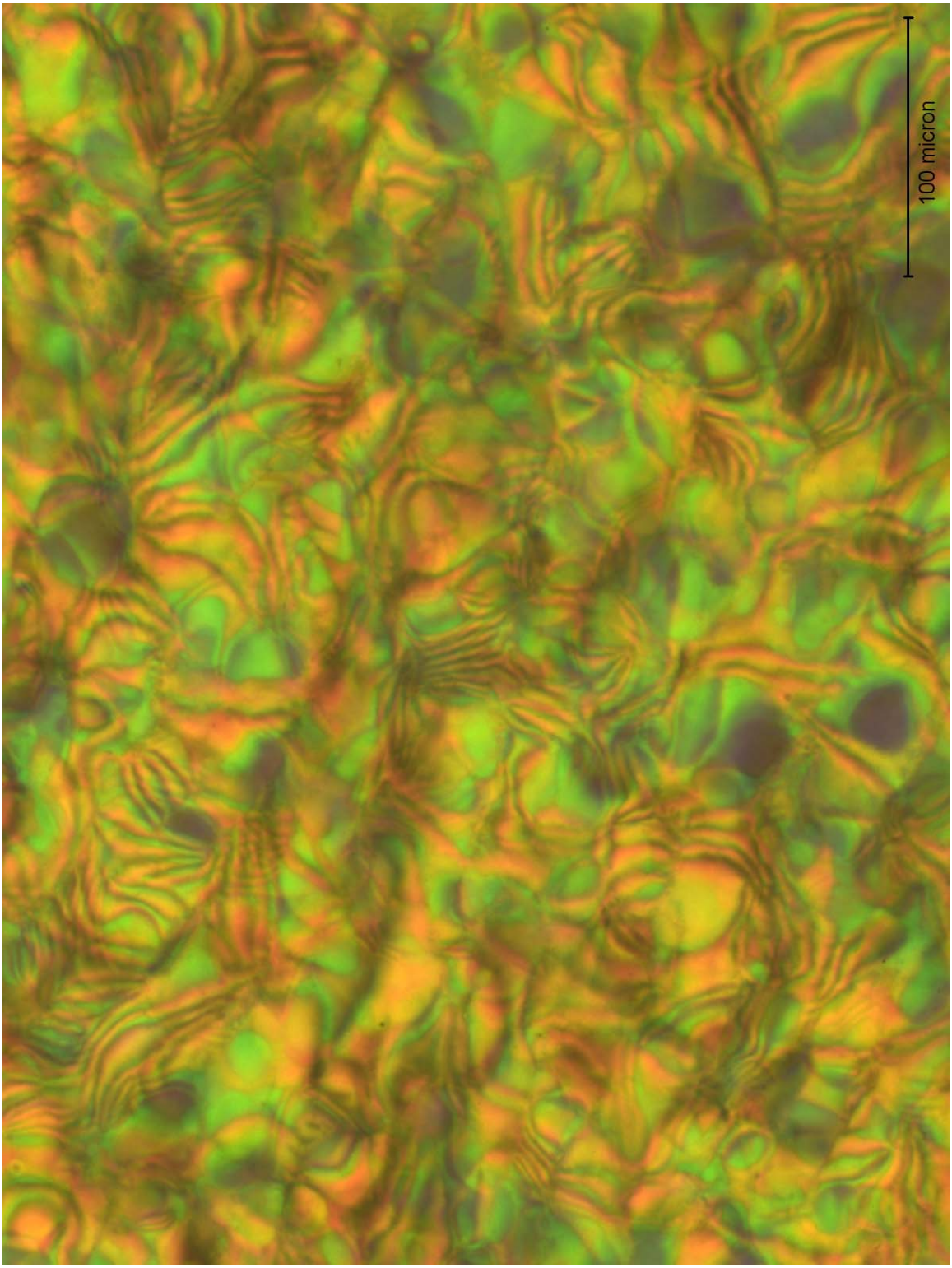

Figure 4.14 Optical micrograph of a film prepared from NCC suspension S1 dried in a 9.7 T magnetic field for 8 hr. The magnification was 40X.

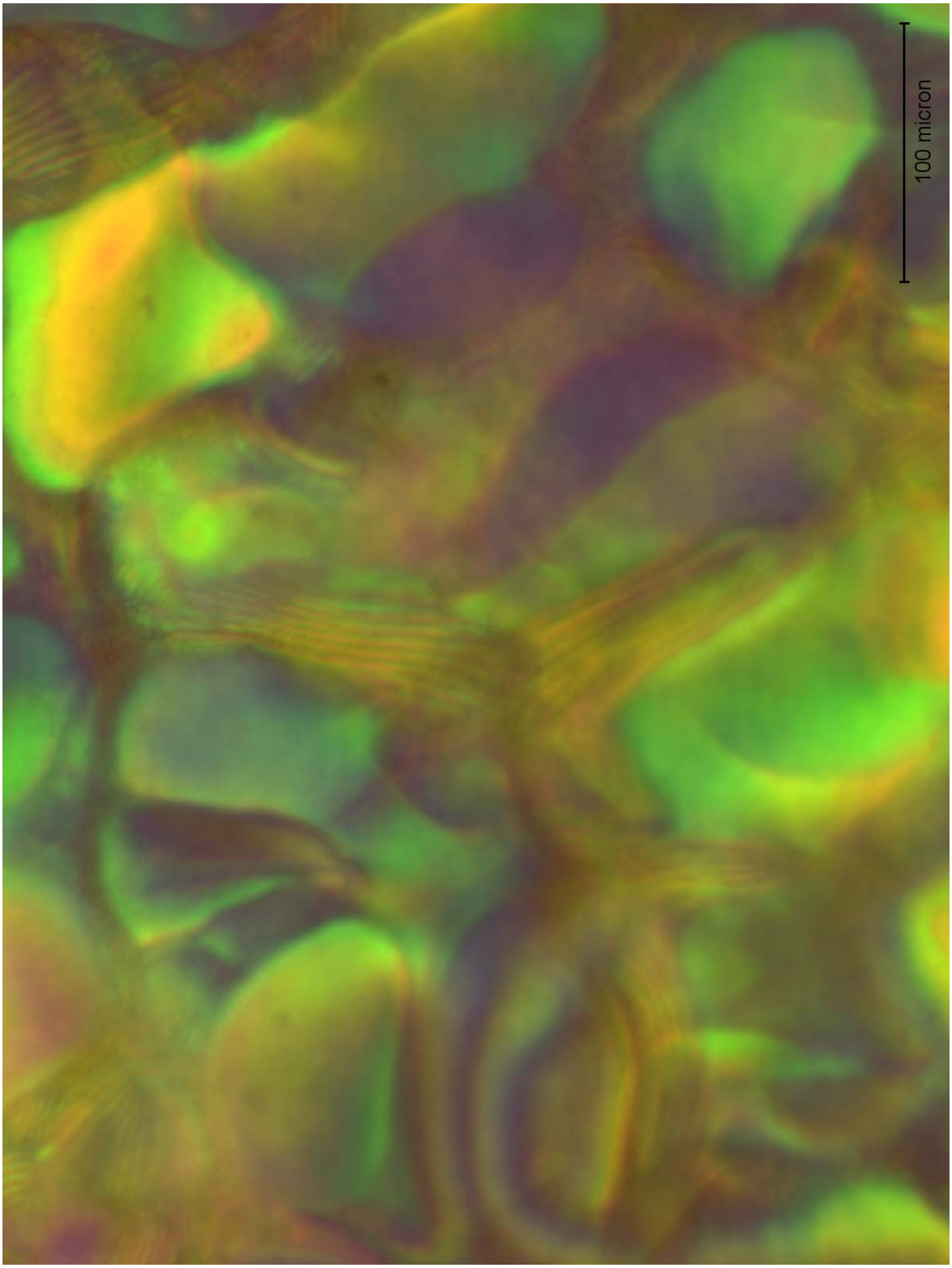

Figure 4.15 Optical micrograph of a film prepared from NCC suspension S2 dried out of a 9.7 T magnetic field. The magnification was 40X.

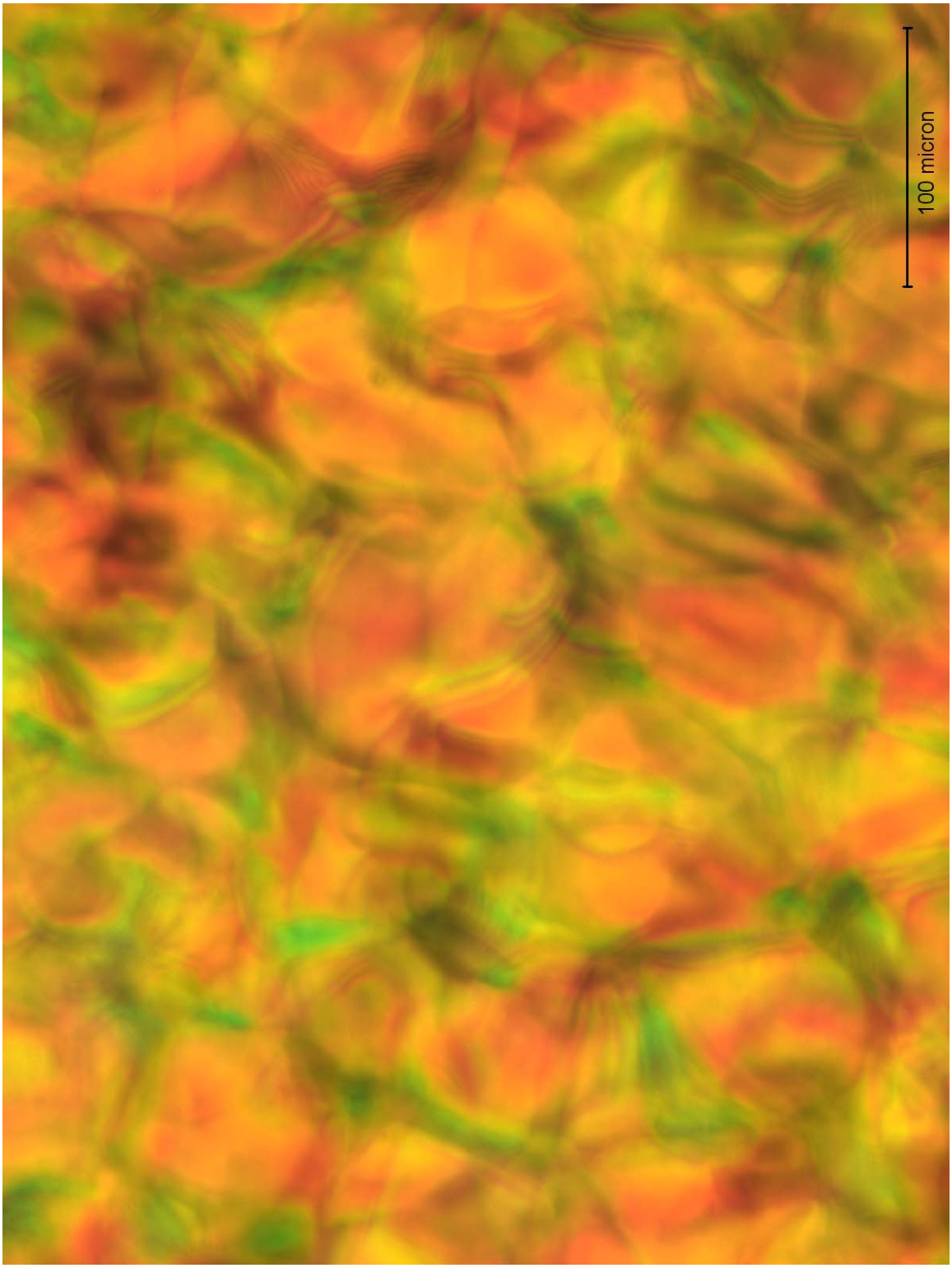

Figure 4.16 Optical micrograph of a film prepared from NCC suspension S2 dried in a 9.7 T magnetic field. The magnification was 40X.

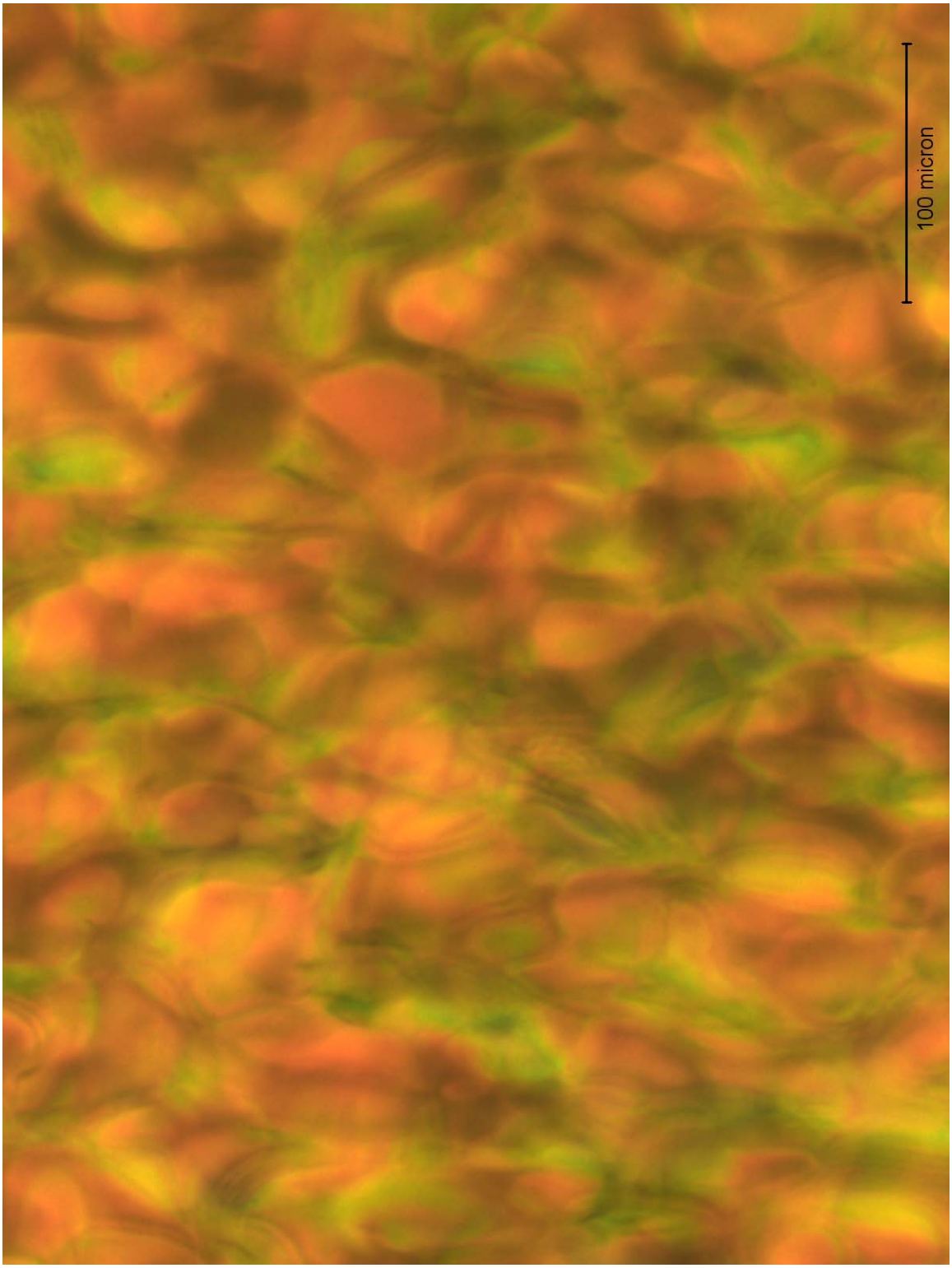

Figure 4.17 Optical micrograph of a film prepared from NCC suspension S2 with 7.0 mM NaCl dried in a 9.7 T magnetic field. The magnification was 40X.

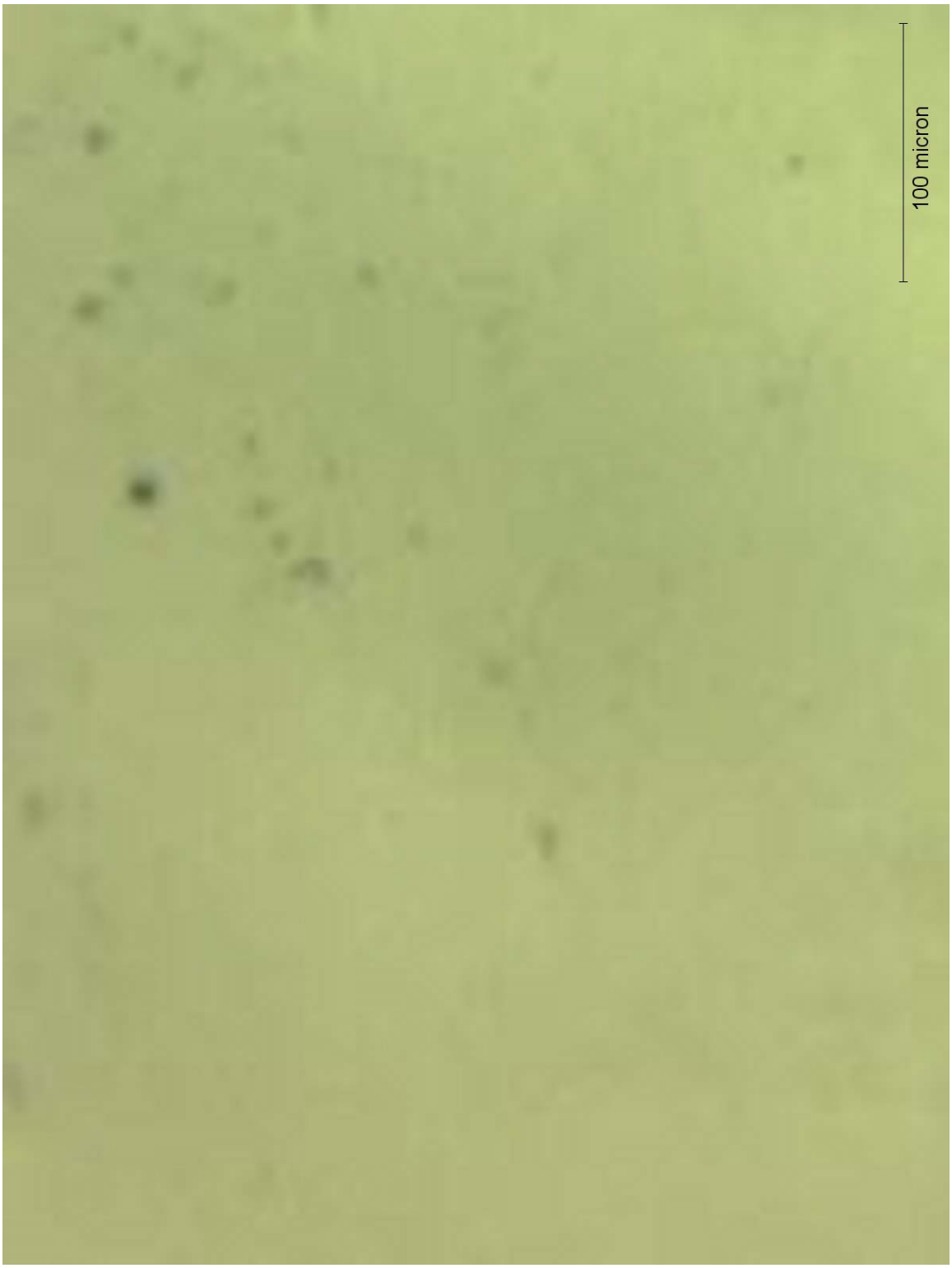

Figure 4.18 Optical micrograph of a film prepared from NCC suspension L1 dried out of a 9.7 T magnetic field. The magnification was 40X.

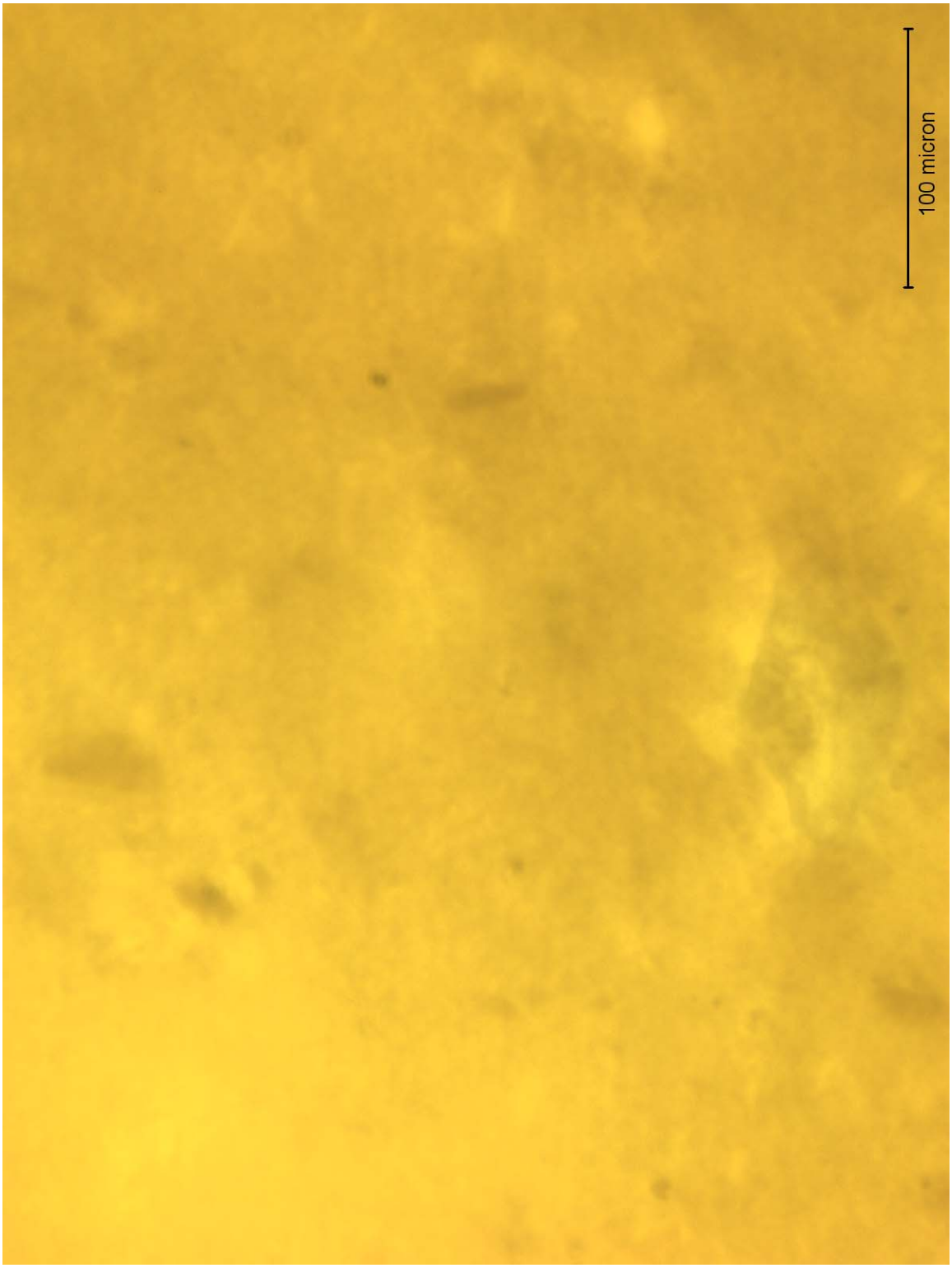

Figure 4.19 Optical micrograph of a film prepared from NCC suspension L1 dried in a 9.7 T magnetic field. The magnification was 40X.

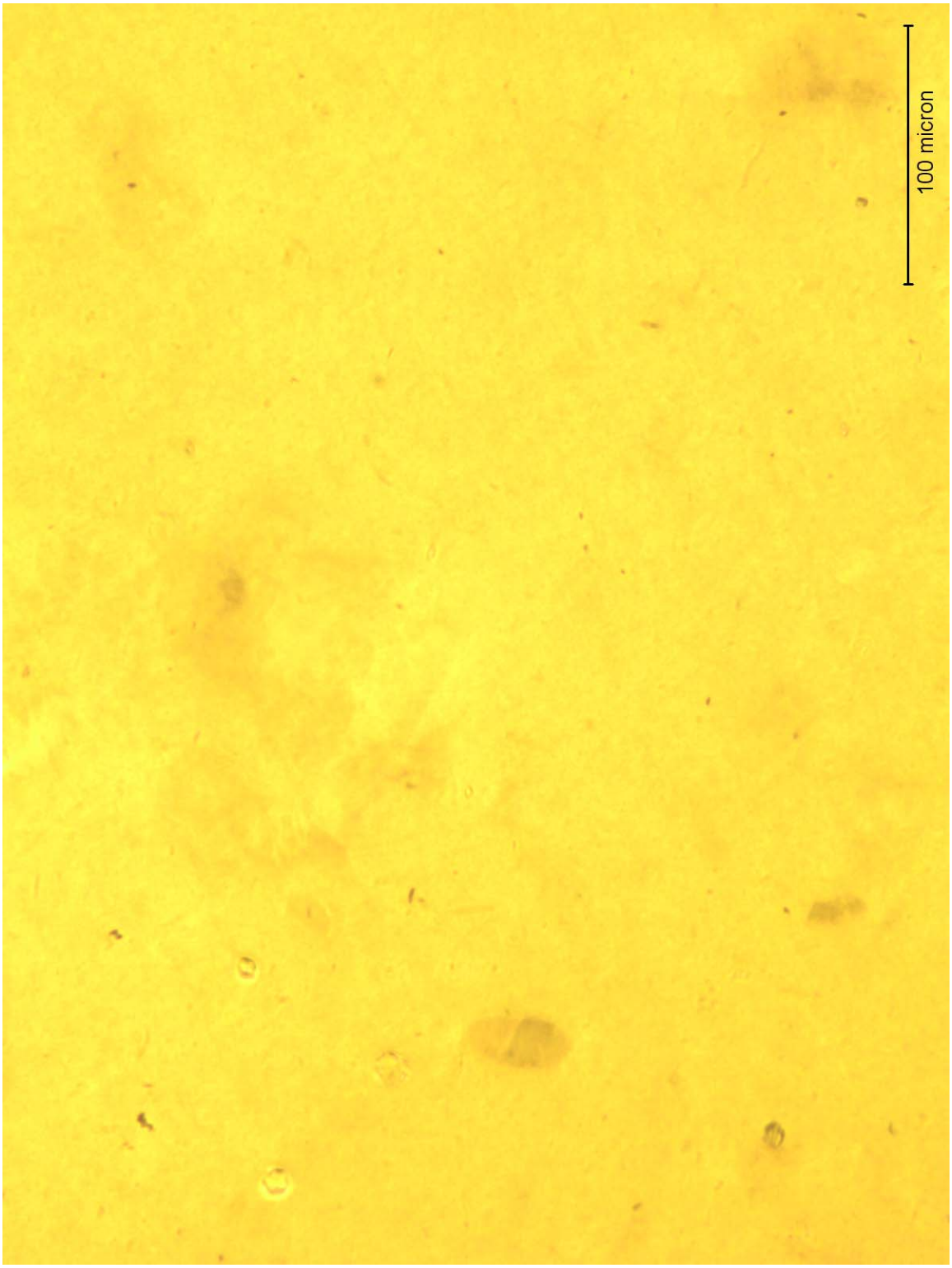

much smaller than the effect of lower temperature and longer exposure time in the magnetic field. The pitch changes in sample S1 films by those two factors were 135 and 107 nm, respectively. When an appropriate amount of NaCl was added in the S2 suspension to obtain ICD signals, the film prepared did not show the fingerprint texture or iridescence (Figure 4.17), indicating that the chiral nematic structure in the film was not strong enough to be observed by polarized microscopy. The weak reflection of the visible light also made the film possibly obtain the ICD signals. Similar results were obtained for the L1 films (Figures 4.18 and 4.19), which were not iridescent, but displayed some chiral nematic structure as determined by ICD spectroscopy (see Section 4.2.2.2).

4.2.2.3 Possible model of chiral nematic structure formation in the magnetic field

The model of the formation of chiral nematic structure (Figure 4.20) in a magnetic field which emerges from the data presented above is the following: initially, the solvent of the isotropic NCC suspension evaporates, and the concentration of the suspension increases. When the concentration reaches the critical concentration, the anisotropic phase starts to form spontaneously. During the drying process in the presence of an external magnetic field, the cellulose crystallites align causing the tilt angle between the orientations of directors of adjacent pseudo-layers to decrease, resulting in an increase in

the chiral nematic pitch.

Figure 4.20 Schematic representation of the chiral nematic structure formation in the magnetic field during the drying process.

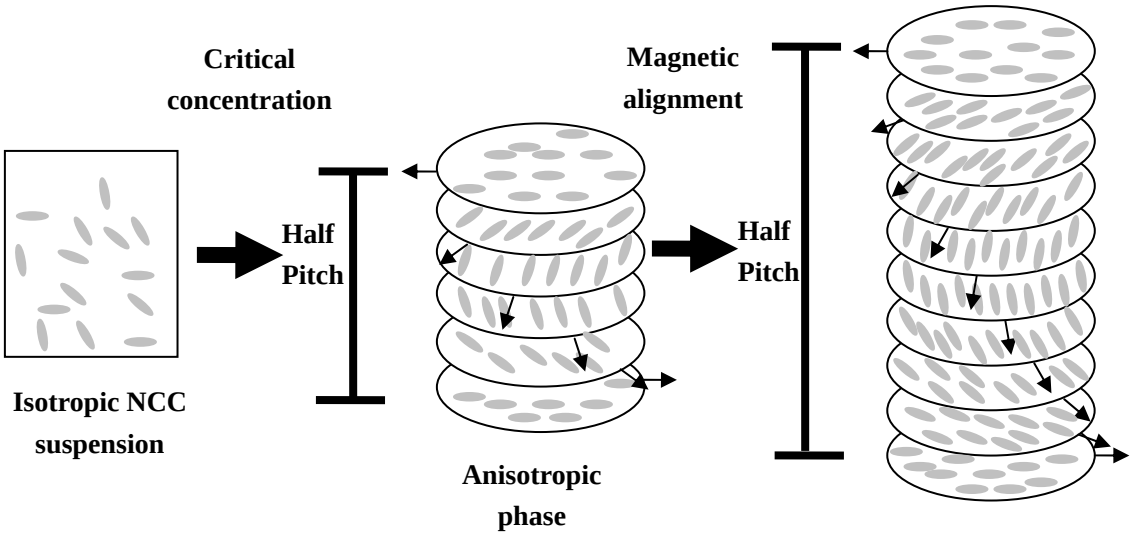

4.2.3 Crystallinity

Up to this point, we have characterized the effect of a number of parameters on the macroscopic morphology of NCC. In order to see whether these parameters also affect the crystallinity of NCC, we characterized the crystallinity of the NCC samples prepared above. The method we chose to do this is ^{13}C CP/MAS solid-state NMR.

4.2.3.1 ^{13}C CP/MAS solid-state NMR spectroscopy

The measurement of cellulose crystallinity can either be obtained by powder X-ray

diffraction methods[259, 260] or by the use of ^{13}C CP/MAS NMR spectroscopy[261, 262]. In the X-ray based methods, the area of the crystalline diffraction is taken relative to the total area of the diffractogram in order to measure the crystallinity. In the latter method, the degree of order of solid cellulose samples can also be obtained by using the peak areas of the C-(4) atoms of crystalline and amorphous cellulose fractions[263] (as labeled in Figure 4.21). Both NMR spectroscopy[263] and the X-ray diffraction method developed by Fink et al.[259] yield the same values for crystallinity of cellulose and are therefore complementary.

In our studies, the ^{13}C CP/MAS NMR spectra were assigned according to the previous assignments[264-268]. The peak areas were determined by deconvolution of the spectra using the DMFIT program[269]. Crystallinity was initially calculated by determining the fraction of the amorphous component, $X_{amorphous}$, of the C-(4) atoms in the sample and using the relationship:

$$X_c = 100\% - X_{amorphous} \quad (4.7)$$

where $X_{amorphous}$ is calculated as the ratio of the peak area of the C-(4) atoms located in amorphous domains (Figure 4.21) and the overall area of the C-(4) atoms. For a consistency check, a similar ratio was calculated using the peaks corresponding to C-(6) atoms, which also display crystalline and amorphous components in the spectra (Figure 4.21).

The $X_{amorphous}$ of the C-(6) or C-(4) atoms for the films prepared from S1, S2, and S3, H1 and H2, and L1 and L2 cellulose suspensions are summarized in Table 4.2 and 4.3, respectively. The corresponding crystallinity fractions X_c are illustrated in Figure 4.22. As

Figure 4.21 **^{13}C CP/MAS NMR spectrum of a film dried from sample S2 in the magnetic field. The experimental spectrum and the fitted spectrum are colored in blue and red respectively and overlap well. The individual lines used in the fit are shown as well.**

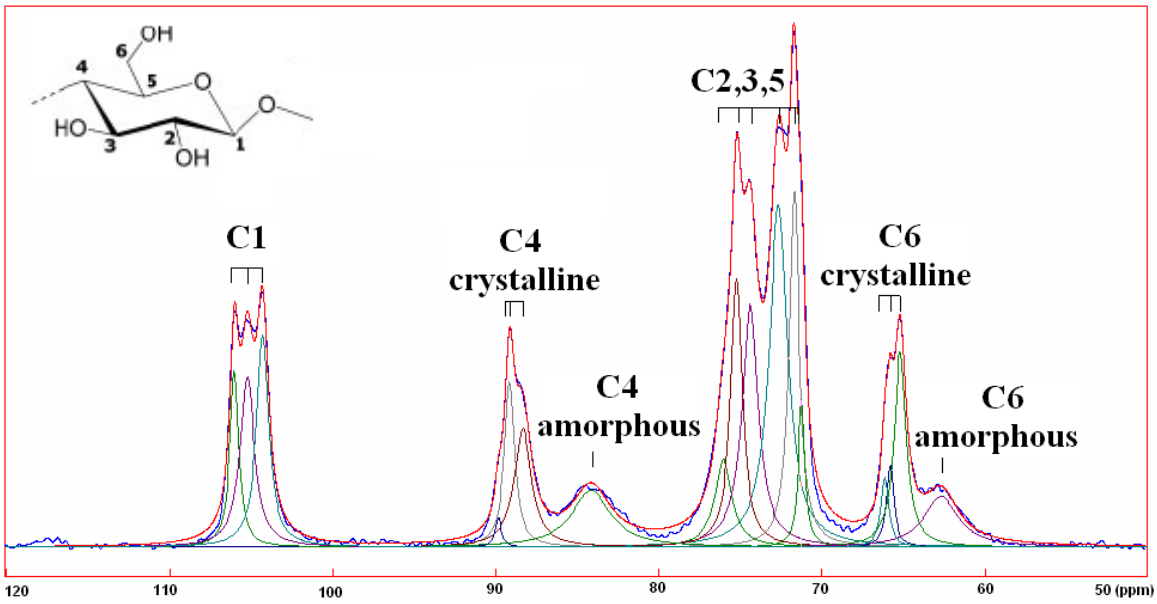

can be seen in Table 4.2 and 4.3, the crystallinity calculated from the two types of C atoms was slightly different. This is most likely due to the error associated with deconvoluting overlapped signals. For the S1 sample, the crystallinity of the film significantly increased with a change in the drying temperature. This suggests that the shorter pitch in the chiral nematic phase observed at 70°C may favor the formation of more crystalline domains in NCC, relative to the lower temperature case. For the other cellulose samples, the salt-free films prepared in the magnetic field had higher crystallinity than those prepared out of the magnetic field, probably because the magnetic field promotes the alignment of cellulose crystallites. These data were consistent with the previous observations that the magnetic alignment of cellulose crystallites can increase

Table 4.2 Fraction of the amorphous and other components based on the integration of the C-(6) peaks for the S1 films prepared at 4 °C and 70 °C, and the S2, S3, H1, H2, L1, and L2 films prepared in and out of a 9.7 T magnetic field. MA represented the films prepared in the magnetic field. NM represented the films prepared out the magnetic field. For S2, S3 and H1, the results for the salted films used in the ICD experiments are reported. The standard deviation (sdev) is obtained from three independent measurements on the same sample (performed for multiple samples). The assignments listed at the top of the table are the same as those reported by Hesse et al[265].

sample	C-(6)			
	amorphous	Cellulose I		
	62.7 ppm	65.3 ppm	65.9 ppm	66.2 ppm
S1_4°C	48.36	34.29	10.66	6.69
S1_70°C	38.51	42.44	11.47	7.59
S2_MA	34.81	42.03	14.58	8.58
S2_NM	35.39	41.92	14.17	8.52
S2_salt	38.43	41.1	12.72	7.75
S3_MA	36.89	41.09	14.24	7.78
S3_NM	37.23	40.98	14.39	7.4
S3_salt	38.2	41.62	11.7	8.48
H1_MA	37.1	41.75	14.05	7.09
H1_NM	38.44	42.01	12.01	7.54
H1_salt	39.15	42.84	10.34	7.68
H2_MA	39.29	42.39	10.6	7.71
H2_NM	40.09	40.74	10.2	8.97
L2_MA	41.58	39.82	11.52	7.08
L2_NM	42.34	40.44	10.11	7.11
L1_MA	45.51	38.05	9.8	6.64
L1_NM	46.41	38.19	9.83	5.57
sdev	(0.56)	(0.47)	(0.53)	(0.29)

Table 4.3 Fraction of the amorphous and other components based on the integration of the C-(4) peaks for the S1 films prepared at 4 °C and 70 °C, and the S2, S3, H1, H2, L1, and L2 films prepared in and out of a 9.7 T magnetic field. MA represented the films prepared in the magnetic field. NM represented the films prepared out the magnetic field. For S2, S3 and H1, the results for the salted films used in the ICD experiments are reported. The standard deviation (sdev) is obtained from three independent measurements on the same sample (performed for multiple samples). The assignments listed at the top of the table are the same as those reported by Hesse et al[265].

sample	C-(4)			
	amorphous	Iβ	Iα, Iβ	Iα
	84.1 ppm	88.4 ppm	89.3 ppm	90.0 ppm
S1_4°C	45.99	27.26	24.71	2.04
S1_70°C	35.88	34.04	28.31	1.77
S2_MA	36.25	31.75	30.44	1.56
S2_NM	37.59	31.36	29.43	1.62
S2_salt	41.39	29.59	27.27	1.76
S3_MA	37.54	30.67	29.86	1.93
S3_NM	38.68	29.93	29.56	1.83
S3_salt	41.03	29.4	27.8	1.77
H1_MA	38.8	29.85	28.9	2.44
H1_NM	40.11	29.08	28.68	2.13
H1_salt	41.42	28.88	27.26	2.43
H2_MA	40.7	29.49	27.22	2.59
H2_NM	41.77	28.54	27.34	2.34
L2_MA	43.73	28.1	24.57	3.59
L2_NM	44.52	27.64	24.43	3.4
L1_MA	47.15	25.53	24.25	3.07
L1_NM	48.07	25.36	23.78	2.79
(sdev)	(0.21)	(0.38)	(0.28)	(0.12)

Figure 4.22 Histogram showing the calculated crystallinity from the signal intensity of (a) C-(6) atoms and (b) C-(4) atoms for the films of S1, S2, S3, H1, H2, L1, and L2 cellulose samples. The crystallinity of films prepared at 4 °C and 70 °C, and prepared in and out of the magnetic field is shown in blue, pink, red, and dark red, respectively. The crystallinity of salted films used in the ICD experiments is shown in violet. The error bars represent the standard deviation reported in Table 4.2 and 4.3.

(a)

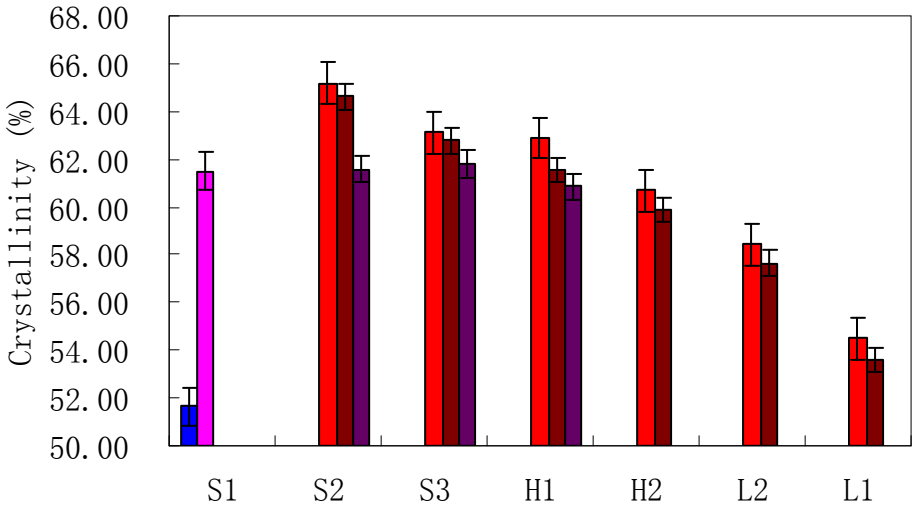

(b)

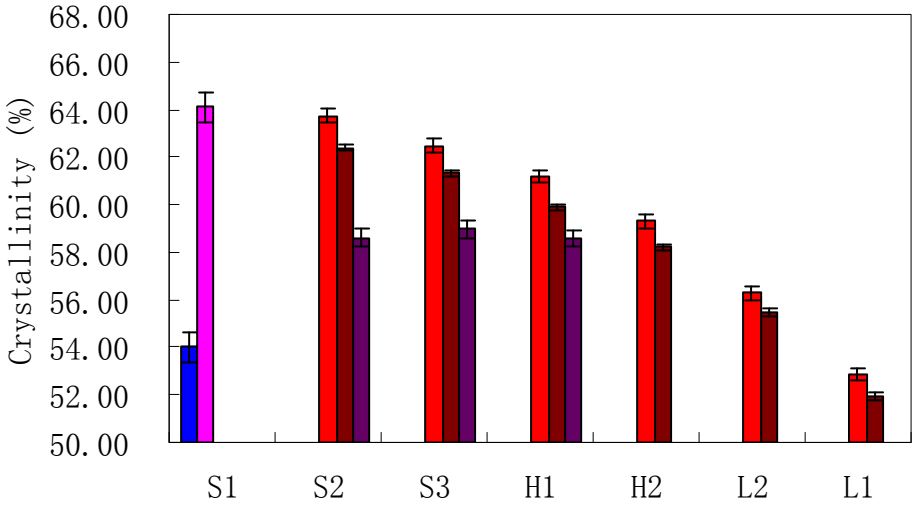

the crystallinity of the samples[270]. However, the reason for this is still not clear. In addition, the crystallinity of the salted films used in the ICD studies was smaller than that of salt-free films. It is important to note that the changes in crystallinity observed are in many cases quite small. In other words, effects such as the presence of a magnetic field or the ionic strength have a more dramatic impact on the chiral nematic structure than on the crystallinity of NCC. Nonetheless, a similar trend is observed for all samples. Correlating the crystallinity results with the pitch of the chiral nematic phase shows that there is no simple relationship between cholesteric phase and extent of crystallinity in NCC. Indeed, the NCC films had a shorter chiral nematic pitch and higher crystallinity at higher temperature than at lower temperature, whereas the magnetic alignment and lower ionic strength resulted in longer chiral nematic pitch and slightly higher crystallinity for the NCC films. Given that dependence of the pitch on the parameters studied here is complex, it is perhaps not surprising that there is no simple relationship between pitch and crystallinity. In any case, these studies show that one can promote the formation of chiral nematic phase and crystalline domains in NCC under certain conditions.

4.3 Summary and conclusions

This chapter presented the physical characterization of the morphology of NCC films. The chiral nematic properties and crystallinity of the films, prepared using various procedures, were determined.

Dried from isotropic NCC suspensions, the S1, S2, and S3 samples can form films with apparent chiral nematic structure. In contrast, the chiral nematic characters of the films prepared from the H1, H2, L1 and L2 samples were very weak. The effects of ionic strength, suspension concentration, drying temperature, and magnetic field on the chiral nematic structure of prepared films have been taken into consideration. The chiral nematic pitch decreased with increasing concentration of NaCl. When the concentration of added salt in the suspension S1 was above 0.5 mM, the films were no longer iridescent in the visible light range. When the concentration of the NCC suspension S1 was above 0.5 w%, the chiral nematic structure was observed and the pitch increased with the increase in the concentration. Higher temperature resulted in shorter chiral nematic pitch, suggesting that the evaporation rate and the diffusion rate of the cellulose crystallites may have an impact on the structures they can adopt in the films. In addition, the chiral nematic pitch became longer as the drying period in the magnetic field increased. This observation might be due to the magnetic alignment of cellulose, which would lead to a decrease in the angles between the directors of the adjacent pseudo-layers, and thus to an increase in the pitch of chiral nematic structure. According to these results, a possible model of the chiral nematic structure formation during the drying process in the magnetic field has been provided: when the isotropic cellulose suspension evaporates to reach the critical concentration, the anisotropic phase starts spontaneously forming in the suspension. During the continuous drying in the magnetic field, the chiral nematic pitch increases as a result of the alignment of cellulose crystallites.

The studies on the crystallinity of films indicated that higher temperature can significantly increase the degree of crystallinity in the NCC films, whereas the effects of magnetic field and electrolyte on the crystallinity were small. Based on our findings, we can conclude that crystallinity has no simple correlation with chiral nematic structure.

4.4 Experimental

4.4.1 Materials

All NCC suspensions used for making films were obtained from FP Innovations, Paprican. The Trypan blue used for ICD spectroscopy and sodium chloride were purchased from Sigma-Aldrich.

4.4.2 Film preparation

Solid cellulose films were made by the slow evaporation of the colloidal suspension under ambient conditions, on 1.0 cm × 3.5 cm glass slides. The doped films for the ICD experiments were prepared by adding 100 μL 1 mM Trypan blue to the colloidal suspension and mixing until a homogeneous solution was obtained. The water was allowed to evaporate, leaving approximately 9.6×10^{-4} g of dye per cellulose film. To produce films that used for ICD spectroscopy, an appropriate amount of the stock NaCl

solution was added prior to evaporation in order to decrease the pitch of the films[235]. Magnetically aligned films were prepared by drying the cellulose suspension in a 9.7 T magnetic field. The surface of the slide was perpendicular to the direction of the magnetic field. Due to the negative diamagnetic susceptibility of cellulose, this alignment should promote the formation of a planar texture, as the cellulose crystallites tend to orient with their long axes perpendicular to the magnetic field[253, 254].

4.4.3 CD spectroscopy

CD spectra were measured using a Jasco J-810 Spectropolarimer. Samples were set perpendicular to the incident cross-polarized light, and scanned at 100 nm/min with a step resolution of 0.2 nm and 1 nm bandwidth. For ICD spectra, baseline corrections were made by subtracting the spectrum of an equivalent film containing no dye.

4.4.4 Polarized microscopy

Photomicrographs were taken by using a Nikon Microphot-FXA optical microscope equipped with a camera and crossed-polarizers. The magnification of the micrographs was about 40X.

4.4.5 ^{13}C CP/MAS solid-state NMR spectroscopy

^{13}C CP/MAS NMR measurements were carried out with a 4 mm triple-resonance MAS probe at Bruker 500 spectrometer operating at 125.768 MHz for ^{13}C. The samples were ground using a mortar and pestle prior to being packed into 4 mm ZrO_2 rotors. 2048 scans were accumulated. The spinning speed was set to 6.5 kHz, and a contact time of 1 ms[225-227] for the cross-polarization. Decoupling was achieved using SPINAL-64 using a field strength of 90.9 kHz. The spectra were referenced to external adamantane, δ_{CH} = 29.50 ppm and δ_{CH_2} = 38.56 ppm relative to TMS[228].

Chapter 5: Summary, conclusions, and future work

5.0 Thesis summary

This thesis presented my work on the structural studies of TBEV FP and NCC films. Chapter 1 introduced some techniques which are usually used to determine the structures of the protein and cellulose. It also presented the basics of the FP and membrane fusion induced by TBEV E protein, and described the relationship between the structure and functional properties. Depending on the position of the FP in the fusion protein, FP can be classified into two categories: Class I, N-terminal FPs, and Class II, internal FPs. The roles of Class I FPs played in the membrane fusion, and their conformational changes during the fusion process have been well studied. However, the structures of Class II FPs in the native state and the conformational changes at different fusion stages are not clear. In addition, Chapter 1 introduced the basics of cellulose structure. The structural investigation on the NCC films will open an opportunity to optimize the production process in order to obtain polymer films with particular physical and chemical properties.

One of the topics which have been discussed in this thesis is the structural and functional studies of Class II FP. One main obstacle encountered in the studies is the lack of pure FPs with native-like structure and activity. In Chapter 2 the design, synthesis and characterization of a synthetic TBEV FP and two mutants was presented, as well as

activity and structural data showing that the synthesized wild-type peptide can serve as a model fusion system in itself.

In Chapter 3, I investigated the structures and activities of modified TBEV FPs, which were developed to form a disulfide bond or a trimer. The presence of disulfide bond can stabilize the folded structure of the peptide. The timer peptide was designed to mimic the oligomerization of this segment in the intact protein during membrane fusion. The influence of an additional soluble peptide segment was also studied.

Lastly, Chapter 4 focused on the determination of the chiral nematic structure and crystallinity of NCC films prepared through various processes. The effects of ionic strength in the NCC suspension, the suspension concentration, the drying temperature and the presence of an external magnetic field on the chiral nematic structure and the degree of crystallinity of the NCC films have been investigated.

5.1 Experimental conclusions

TBEV FP is a hydrophobic and glycine rich sequence, which is almost fully conserved in all flaviviruses[106]. The crystal structure shows that this segment is located in the middle of two β-strands, which are stabilized by a disulfide bond between them[106]. At neutral pH, the TBEV FP is buried in the interior of the E protein dimer[106]. The conformational change of the protein triggered by the acidic pH of the endosomes exposes the FP at one end of the protein trimer[107]. Evidence has shown that the TBEV FP

is important for the fusogenic activity of the virus[168]. It is believed to insert into the target membrane during the fusion process. Mutations of the sequence strongly affect the fusion induced by the intact protein[108]

Our studies on the TBEV FP first involved the design, synthesis and characterization of the native-like peptide. We chose the peptide sequence representing residues 93-113 in the E protein as the wild-type target peptide, WT. This segment contains the sequence found to be critical to fusion activity[106], namely residue 100-113. The peptide was synthesized by SPPS. The initial synthesis was not successful because of the difficulty in the coupling of the Lys 93 and Arg 94 residues. Double coupling of these two amino acids in the synthesis procedure has provided the target synthetic peptide with both high yield and purity. In order to investigate the effect of the mutation at Leu 107 position on the structure and activity of the FP, two mutants L107F and L107T have also been synthesized. The L107F mutation represents a common mutation found in some of the other flaviviruses[169-171]. The L107T mutation is rare in nature, but allows us to test the effects of substituting a hydrophobic amino acid to a polar one. The CD spectra have shown that the presence of cholesterol in the associated liposomes help the WT peptide to fold. The importance of cholesterol in the binding membrane has also been observed for HIV FP[16, 98]. The mutation of Phe at the 107 position was found not to have an effect on secondary structure, whereas the mutant L107T adopted a smaller fraction of β-strand conformation than both WT and L107F peptides. Tryptophan fluorescence spectroscopy experiments have been applied to assess the insertion ability of the peptides into the

target membrane. Similar results were obtained for WT and L107F. The emission intensity of the Trp 101 residue in these two peptides increased when the peptides were associated with lipids, indicating that the Trp 101 residue in these two peptides was in a less hydrophilic environment and the peptides inserted into the hydrophobic core of the bilayers. No increase of the emission intensity was observed when L107T bound to the lipid vesicles, indicating that the polar group in Thr makes the insertion of the peptide much less favorable. Fusogenic activity of the synthesized peptides was determined by FRET assay and photon correlation spectroscopy. The fusion induced by the three synthetic FPs was pH dependent. At neutral pH, no fusion reaction occurred, whereas acidic pH triggered membrane fusion. The fusion induced by WT or L107F peptides was relatively fast and strong. The mutant of L107T induced fusion with a smaller extent, indicating that the polar substitution of Leu 107 residue impaired the fusogenic activity of TBEV FP. Furthermore, a relatively high pH threshold, compared to that of fusion induced by alphaviruses[134, 202], was observed for the pH dependent fusion induced by the synthetic peptides. This observation has also been reported for other flaviviruses[201], indicating that flaviviruses may fuse from within early endosomes[206]. The presence of cholesterol in the target membrane was found, although not absolutely essential, to facilitate the fusion induced by WT. The decrease in TBEV FP fusion seen with Chol-free liposomes may be due to a lower extent of peptide-liposome binding. These results were similar to the studies on HIV FP[133, 134], but different from SFV and SIN, which absolutely require the presence of cholesterol for the membrane fusion[129, 131-134]. The investigation

on the fusogenic activity of synthetic peptides has provided results which are consistent with the previous studies on the intact E protein[108, 110], indicating that the synthetic FPs can serve as a model fusion system.

Further studies of TBEV FP were carried to examine the importance of the disulfide bond and of oligomerization in the structure and activity. We synthesized a longer peptide such that a disulfide bond could form between the Cys 92 and Cys 116 residues, as in the intact E protein[106]. In order to avoid the formation of disulfide bond at the Cys 105 residue, this amino acid was mutated to Ala. CD spectra of TFPSS demonstrated that the disulfide bond stabilized the folded structure, allowing a larger fraction of β-strand conformation to form. However, the peptide penetration and fusogenic activity did not change in the presence of disulfide bond. This suggests that the segment of the more structured TFPSS which interacts with the membrane is the same as the segment in the WT FP. Furthermore, the effect of temperature on the fusion induced by TFPSS suggested that the conformational change in TBEV FP during membrane fusion might be a facile process with a low activation energy.

The trimer of the TBEV FP was achieved by synthesizing the peptide strands on a prepared lysine side-chain scaffold[105]. CD spectroscopy indicated that the close position of the monomer strands in the peptide trimer did not affect the conformation of the FP trimer, as compared to the isolated monomers. The functional studies demonstrated that trimeric oligomerization can enhance the fusogenic activity of the TBEV FP, but not change its ability to insert into membranes. Perhaps, the increase of the FP local

concentration may provide a reason for the greater fusogenic activity of TFPtr. A comparison of the structures and activities of WT FP, TFPSS and TFPtr has yielded the following mechanistic insight: the lipid-binding portion in the three peptides adopts similar structure and has similar insertion ability. About 7 residues in the non-binding segment of WT FP and each branch of TFPtr form β-strand conformation, while about 13 residues in this region of TFPSS adopt this secondary structure. The close proximity of three FP segments in TFPtr causes stronger fusogenic activity than WT FP and TFPSS because in this case the trimer is already preformed.

Finally, we investigated the effect of water solubility on the structure and activity of the TBEV FP. A six-lysine segment was added at the C-terminus of the synthetic peptides, as was done in previous studies on other FPs[60, 105]. TFPtrK and TFPmnK did not fold well when bound to liposomes, because they did not insert into the target membrane as deeply as TFPtr and TFPmn did. This indicates that they preferred to partition into the aqueous solution. Surprisingly, both TFPtrK and TFPmnK can promote the fusion of PC/PE/Chol LUVs, even at neutral pH. The increased positive charge from the lysine side-chains may facilitate the aggregation of the vesicles containing PE lipid, similar to what was shown for other cations[221, 222]. Furthermore, the higher local concentration of lysine side-chains in TFPtrK induced stronger aggregation of PC/PE/Chol LUVs at pH 7.5 than TFPmnK. However, the fusogenic activities of the FP segment in TFPtrK and TFPmnK were weaker than TFPtr and TFPmn, respectively, because of the shallow insertion and insufficient folding of this portion, due to the presence of the soluble

segments.

The other project in this thesis was the structural studies on the NCC films. The effects of ionic strength in NCC suspension, the suspension concentration, drying temperature, and the applied magnetic field on the chiral nematic structure and crystallinity have been investigated. The added salt in the NCC suspension decreased the pitch and destroyed the chiral nematic structure, because the presence of the salt effectively decreased the chiral nematic pitch in the anisotropic phase, and increased the critical concentration required to form the anisotropic phase in the suspension, making the formation of the chiral nematic structure more difficult. With the increase of NCC suspension concentration, the chiral nematic properties of the films became more pronounced. The chiral nematic pitch increased as a function of suspension concentration, because at lower concentration the anisotropic phase may form more slowly and therefore the chiral nematic structure as well. The dependence of the chiral nematic pitch of the films on temperature suggested that the temperature might effect the pitch of anisotropic phase in the suspension[248], and the rate of diffusion of the cellulose crystallites in the suspension and the evaporation rate of the solvent is directly related to the formation of chiral nematic structure in the films. The cellulose crystallites can align in the magnetic field[253], which might be the cause of the chiral nematic pitch of NCC films increasing in the magnet. A possible model of the chiral nematic structure formation in the magnetic field has been provided: initially, the solvent of isotropic NCC suspension evaporates. When the concentration of the suspension reaches the critical

concentration, the anisotropic phase starts to form spontaneously. During the drying process, the magnetic alignment of the cellulose crystallites decreases the tilt angle between the directors of the adjacent pseudo-layers, causing an increase of the chiral nematic pitch. Finally, the studies on the crystallinity have shown that higher temperature can significantly increase the crystallinity of the NCC film. But the effects of ionic strength in the suspension and applied magnetic field on the crystallinity were not obvious. These results suggest that the sample conditions listed above affect the chiral nematic structure and the crystallinity of NCC films differently, a finding which will be important in new material research.

5.2 Future work

Structural and functional studies on the TBEV FP have already helped unravel some of the questions underlying the membrane fusion induced by TBEV. The ability to design, synthesize and characterize native-like synthetic FPs facilitates the understanding of the relationship between the structure of TBEV FP and its fusogenic activity. The mechanism by which the TBEV FPs interact with lipids and with each other is beginning to be understand, but much remains to be studied.

The CD spectroscopy that has been described in this thesis has provided experimental support for the structures of the TBEV FP in the various environments, however, only the secondary structure content can be estimated using this technique.

Detailed information about the secondary structure and the tertiary conformational changes during the fusion process cannot be obtained by this technique. Therefore, solid-state NMR would inevitably be useful to elucidate the arrangement of the TBEV FP in a membrane environment.

Solid-state NMR, with its advantages of providing high-resolution structure information on membrane proteins in the presence of lipids[17, 271-274], is a powerful protocol to determine the conformation of the proteins in the native state. We tried to use ^{13}C CP/MAS to assign the synthetic TFPtr labeled at Phe 108 by ^{13}CO. But because of the overlap of the large natural abundance signal from the lipid carbonyls and the low signal-to-noise ratio in the carbonyl region, the signals from labeled peptide were not distinguishable. The signals were difficult to obtain even when the temperature was lowered to -40 ℃. The reason might be that (1) the peptide was too mobile at this temperature, so that the magnetization cannot be perfectly transferred between the spins; (2) when the peptide-to-lipid ratios were higher than 1:150, TFPtr only bound weakly on the lipid vesicles, which made the amount of peptide in the NMR sample small. Changing the temperature to lower than -40 ℃ can reduce the mobility of the FP and therefore enhance the resolution of the signals[224]. The application of ether linked lipids can remove the natural abundance signal from the lipid carbonyls and leave the labeled carbonyl signal in the spectrum. The problem of signal overlap can also be resolved by applying rotational-echo double-resonance (REDOR) filter pulse after the CP pulse[182, 275]. When applied the synthetic peptide with specific labeled at Phe 108 by ^{13}CO and Gly 109

by ^{15}N, the REDOR pulse can be used to filter out natural abundance ^{13}C signals from the lipids and the FP and the resulting spectra are dominated by the signal from the ^{13}CO label, directly bonded to the ^{15}N amide label. Once the peptide is fully assigned, the conformation of each residue can be predicted, because there are well-known correlations between ^{13}CO chemical shifts and local conformation[10]. REDOR is a powerful tool to determine the heteronuclear distance as well[275]. By appropriately choosing labeled sites, such as ^{13}CO in Trp 101 and ^{15}N in Ala 105, distances between labels can be measured. In this way, a three-dimensional model of the TBEV FP will be built, and the conformational changes during the membrane fusion can be determined, which will help us to understand the mechanism of fusion induced by TBEV. It is also important to know how deeply the TBEV FP inserts into the lipid bilayers. By measuring the distances between the labeled residues and lipid head groups, not only the depth of FP insertion but also the orientation of FP in the membranes can be determined. Furthermore, the crystal structure of E protein suggests that in the trimeric structure, the side-chains of Trp 101, Leu 107, and Phe 108 residues are fully exposed on the molecular surface and they form a bowl-like cavity at the trimer tip as the hydrophobic anchor[77]. It would be interesting to determine the conformation of these side-chains by using ^{19}F centerband-only detection of exchange (CODEX) experiments[276-278] with the peptide whose Trp or Phe residue in labeled by ^{19}F. Note that synthesizing these labeled peptides does not require new protocols to be developed. Those found in the Materials and Methods sections still apply.

The other project in this thesis was focused on the studies on NCC films. We have

found that the S samples, H samples, and L samples are different for their ability to form chiral nematic structure, even extracted from the same pulp fibers. The films made using the S samples can form strong chiral nematic structure, whereas the films made from the H samples and L samples do not appear iridescence in the visible light range. Further studies will be carried on the mixture of these three kinds of NCC samples: the effect of their volume fraction on the formation of chiral nematic and crystalline structure, and the effect of ionic strength in the suspension, suspension concentration, drying temperature, and applied magnetic field on the chiral nematic pitch and crystallinity of the films with the certain fractions of S sample, H sample, and L sample. Besides the chiral nematic structure and crystallinity, the mechanical property is another important property of NCC films which needs to be considered. Previous studies indicate that NCC has a very high tensile strength (between 130 and 150 GPa), which provides NCC with a great potential for the reinforcement of polymer matrices[279, 280]. Several studies have shown that NCC serves as a reinforcing filler to dramatically increase the strength of reinforced thermoset and thermoplastic materials[281-284]. This effect was attributed to the formation of a crystallite network linked by hydrogen bonds between the cellulose crystallites[279]. My studies on the crystallinity of NCC films have shown that the sampling conditions, such as ionic strength, dying temperature and magnetic field, can affect the formation of intermolecular hydrogen bonds. Therefore, it would be interesting to study the effects of these factors on the tensile strength of NCC films. This investigation will open the door to produce the new materials with specific physical and chemical properties.

References

1. Durell, S.R.; Martin, I.; Ruysschaert, J.M.; Shai, Y.; Blumenthal, R. *Mol. Membr. Biol.* **1997**, *14*, 97-112.

2. Voet, D.; Voet, J.G.; Pratt, C.W. *Fundamentals of Biochemistry*, John Wiley and Sons, Inc.: 2002.

3. Taken from http://upload.wikimedia.org/wikipedia/commons/1/19/Dengue_virus_-_envelope_protein.jpg (accessed 14/07/2009)

4. Taken from http://commons.wikimedia.org/w/thumb.php?f=Plant%20cell%20wall%20diagram.svg&width=500px (accessed 14/07/2009)

5. Nieva, J.L.; Agirre, A. *Biochim. Biophys. Acta.* **2003**, *1614*, 104-115.

6. Revol, J.F.; Bradford, H.; Giasson, J.; Marchessault, R.H.; Gray, D.G. *Int. J. Biol. Macromolecules* **1992**, *14*, 170-172.

7. Revol, J.F.; Godbout, L.; Gray, D.G. *J. Pulp Pap. Sci.* **1998**, *24*, 146.

8. deVries, H.I. *Acta Crystallogr.* **1951**, *4*, 219-226.

9. Revol, J.F.; Godbout, L.; Gray, D.G. *Chem. Abstr.* **1997**, *123*, 343525 f.

10. Zhang, H.; Neal, S.; Wishart, D.S. *J. Biomol. NMR* **2003**, *25*, 173-195.

11. Sharpe, S.; Yau, W.M.; Tycko, R. *Protein Expr. Purif.* **2005**, *42*, 200-210.

12. Curtis-Fisk, J.; Preston, C.; Zheng, Z.; Worden, R.M.; Weliky, D.P. *J. Am. Chem. Soc.* **2007**, *129*, 11320-11321.

13. Hu, J.; Qin, H.; Li, C.; Sharma, M.; Cross, T.A.; Gao, F.P. *Protein Sci.* **2007**, *16*, 2153-2165.

14. Scheidt, H.A.; Vogel, A.; Eckhoff, A.; Koenig, B.W.; Huster, D. *Eur. Biophys. J.* **2007**, *36*, 393-404.

15. Zheng, Z.; Yang, R.; Bodner, M.L.; Weliky, D.P. *Biochemistry* **2006**, *45*,

12960-12975.

16. Qiang, W.; Bodner, M.L.; Weliky, D.P. *J. Am. Chem. Soc.* **2008**, *130*, 5459-5471.

17. Watts, A.; Straus, S.K.; Grage, S.L.; Kamihira, M.; Lam, Y.H.; Zhao, X. *Methods Mol. Biol.* **2004**, *278*, 403-473.

18. Pines, A.; Gibby, M.G.; Waugh, J.S. *J. Chem. Phys.* **1973**, *59*, 569-590.

19. Hartmann, S.; Hahn, E.L. *Phys. Rev.* **1962**, *128*, 2042-2053.

20. Johnson, W.C.J. *Proteins* **1990**, *7*, 205-214.

21. Woody, R.W. *Methods Enzymol.* **1995**, *246*, 34-70.

22. Fasman, G.D. *Circular Dichroism and the Conformational Analysis of Biomolecules*, Plenum Press: New York, 1996.

23. Gottarelli, G.; Spada, G.P. In *Circular Dichroism Principles and Applications - Application of CD to the study of some cholesteric mesophases*. Nakanishi, K.; Berova, N.; Woody, R.W.; VCH Puclishers: New York, 1994; pp 105-119.

24. Taken from http://www.proteinchemist.com/cd/cd7.gif (accessed 15/09/2008)

25. Jahn, R.; Lang, T.; Südhof, T.C. *Cell* **2003**, *112*, 519-533.

26. Jardetzky, T.S.; Lamb, R.A. *Nature* **2004**, *427*, 307-308.

27. Kielian, M.; Rey, F.A. *Nat. Rev. Microbiol.* **2006**, *4*, 67-76.

28. Taken from http://www.erin.utoronto.ca/~w3bio315/picts/lectures/lecture14/ViralEndocytosis1.jpg (accessed 02/03/2009)

29. Gallaher, W.R. *Cell* **1987**, *50*, 327-328.

30. White, J. *Science* **1992**, *258*, 917-923.

31. Hernandez, L.D.; Hoffman, L.R.; Wolfsberg, T.G.; White, J.M. *Annu. Rev. Cell. Dev. Biol.* **1996**, *12*, 627-661.

32. Nir, S.; Nieva, J.L. *Prog. Lipid Res.* **2000**, *39*, 181-206.

33. Tamm, L.K.; Han, X. *Biosci. Rep.* **2000**, *20*, 501-518.

34. Mandl, C.W.; Heinz, F.X.; Kunz, C. *Virology* **1988**, *166*, 197-205.

35. Sumiyoshi, H.; Mori, C.; Fuke, I.; Morita, K.; Kuhara, S.; Kondou, J.; Kikuchi, Y.; Nagamatu, H.; Igarashi, A. *Virology* **1987**, *161*, 497-510.

36. Rice, C.M.; Lenches, E.M.; Eddy, S.R.; Shin, S.J.; Sheets, R.L.; Strauss, J.H. *Science* **1985**, *229*, 726-733.

37. Lewis, J.A.; Chang, G.J.; Lanciotti, R.S.; Kinney, R.M.; Mayer, L.W.; Trent, D.W. *Virology* **1993**, *197*, 216-224.

38. Chan, D.C.; Kim, P.S. *Cell* **1998**, *93*, 681-684.

39. Doms, R.W.; Moore, J.P. *J. Cell Biol.* **2000**, *151*, F9-F13.

40. Skehel, J.J.; Wiley, D.C. *Annu. Rev. Biochem.* **2000**, *69*, 531-569.

41. Eckert, D.M.; Kim, P.S. *Annu. Rev. Biochem.* **2001**, *70*, 777-810.

42. Stiasny, K.; Brandler, S.; Kössl, C.; Heinz, F.X. *J. Virol.* **2007**, *81*, 11526-11531.

43. Baker, K.A.; Dutch, R.E.; Lamb, R.A.; Jardetzky, T.S. *Mol. Cell* **1999**, *3*, 309-319.

44. Melikyan, G.B.; Markosyan, R.M.; Hemmati, H.; Delmedico, M.K.; Lambert, D.; Cohen, F.S. *J. Cell Biol.* **2000**, *151*, 413-423.

45. Russel, C.J.; Jardetzky, T.S.; Lamb, R.A. *EMBO J.* **2001**, *20*, 4024-4034.

46. Gruenke, J.A.; Armstrong, R.T.; Newcomb, W.W.; Brown, J.C.; White, J.M. *J. Virol.* **2002**, *76*, 4456-4466.

47. Weissenhorn, W.; Dessen, A.; Harrison, S.C.; Skehel, J.J.; Wiley, D.C. *Nature* **1997**, *387*, 426-428.

48. Gething, M.J.; Doms, R.W.; York, D.; White, J. *J. Cell. Biol.* **1986**, *102*, 11-23.

49. Schoch, C.; Blumenthal, R. *J. Biol. Chem.* **1993**, *268*, 9267-9274.

50. Qiao, H.; Armstrong, R.T.; Melikyan, G.B.; Cohen, F.S.; White, J.M. *Mol. Biol. Cell* **1999**, *10*, 2759-2769.

51. Steinhauer, D.A.; Wharton, S.A.; Skehel, J.J.; Wiley, D.C. *J. Virol.* **1995**, *69*, 6643-6651.

52. Han, X.; Steinhauer, D.A.; Wharton, S.A.; Tamm, L.K. *Biochemistry* **1999**, *38*, 15052-15059.

53. Cross, K.J.; Wharton, S.A.; Skehel, J.J.; Wiley, D.C.; Steinhauer, D.A. *EMBO J.* **2001**, *20*, 4432-4442.

54. Brunner, J. *FEBS Lett.* **1989**, *257*, 369-372.

55. Macosko, J.C.; Kim, C.H.; Shin, Y.K. *J. Mol. Biol.* **1997**, *267*, 1139-1148.

56. Han, X.; Bushweller, J.H.; Cafiso, D.S.; Tamm, L.K. *Nat. Struct. Biol.* **2001**, *8*, 715-720.

57. Wimley, W.C.; White, S.H. *Nat. Struct. Biol.* **1996**, *3*, 842-848.

58. Pereira, F.B.; Goñi, F.M.; Muga, A.; Nieva, J.L. *Biophys. J.* **1997**, *73*, 1977-1986.

59. Ruiz-Argüello, M.B.; Goñi, F.M.; Pereira, F.B.; Nieva, J.L. *J. Virol.* **1998**, *72*, 1775-1781.

60. Han, X.; Tamm, L.K. *Proc. Natl. Acad. Sci. U.S.A.* **2000**, *97*, 13097-13102.

61. Han, X.; Tamm, L.K. *J. Mol. Biol.* **2000**, *304*, 953-965.

62. Epand, R.M. *Biochim. Biophys. Acta.* **1998**, *1376*, 353-368.

63. Chernomordik, L. *Chem. Phys. Lipids.* **1996**, *81*, 203-213.

64. Siegel, D.P. *Biophys. J.* **1999**, *76*, 291-313.

65. Epand, R.M.; Epand, R.F. *Biochem. Biophys. Res. Commun.* **1994**, *202*, 1420-1425.

66. Epand, R.M.; Epand, R.F.; Martin, I.; Ruysschaert, J.M. *Biochemistry* **2001**, *40*,

8800-8807.

67. Colotto, A.; Martin, I.; Ruysschaert, J.M.; Sen, A.; Hui, S.W.; Epand, R.M. *Biochemistry* **1996**, *35*, 980-989.

68. Epand, R.F.; Martin, I.; Ruysschaert, J.M.E., R.M. *Biochem. Biophys. Res. Commun.* **1994**, *205*, 1938-1943.

69. Longo, M.L.; Waring, A.J.; Hammer, D.A. *Biophys. J.* **1997**, *73*, 1430-1439.

70. Epand, R.M.; Cheetham, J.J.; Epand, R.F.; Yeagle, P.L.; Richardson, C.D.; Rockwell, A.; Degrado, W.F. *Biopolymers* **1992**, *32*, 309-314.

71. Markovic, I.; Leikina, E.; Zhukovsky, M.; Zimmerberg, J.; Chernomordik, L.V. *J. Cell Biol.* **2001**, *155*, 833-844.

72. Schroth-Diez, B.; Ludwig, K.; Baljinnyam, B.; Kozerski, C.; Huang, Q.; Herrmann, A. *Biosci. Rep.* **2000**, *20*, 571-595.

73. Peisajovich, S.G.; Epand, R.F.; Pritsker, M.; Shai, Y.; Epand, R.M. *Biochemistry* **2000**, *39*, 1826-1833.

74. Yang, J.; Gabrys, C.M.; Weliky, D.P. *Biochemistry* **2001**, *40*, 8126-8137.

75. Shokralla, S.; Chernish, R.; Ghosh, H.P. *Virology* **1999**, *256*, 119-129.

76. Delos, S.E.; White, J.M. *J. Virol.* **2000**, *74*, 9738-9741.

77. Modis, Y., Ogata, S., Clements, D., and Harrison, S. C. *Nature* **2004**, *427*, 313-319.

78. Wilson, I.A.; Skehel, J.J.; Wiley, D.C. *Nature* **1981**, *289*, 366-373.

79. Chen, J.; Skehel, J.J.; Wiley, D.C. *Proc. Natl Acad. Sci. U.S.A.* **1999**, *96*, 8967-8972.

80. Fleury, D.; Wharton, S.A.; Skehel, J.J.; Knossow, M.; Bizebard, T. *Nat. Struct. Biol.* **1998**, *5*, 119-123.

81. Murata, M.; Sugahara, Y.; Takahashi, S.; Ohnishi, S. *J. Biochem.* **1987**, *102*, 957-962.

82. Lear, J.D.; DeGrado, W.F. *J. Biol. Chem.* **1987**, *262*, 6500-6505.

83. Wharton, S.A.; Martin, S.R.; Ruigrok, R.W.; Skehel, J.J.; Wiley, D.C. *J. Gen. Virol.* **1988**, *69*, 1847-1857.

84. Gray, C.; Tatulian, S.A.; Wharton, S.A.; Tamm, L.K. *Biophys. J.* **1996**, *70*, 2275-2286.

85. Killian, J.A. *Biochim. Biophys. Acta.* **1992**, *1113*, 391-425.

86. Li, Y.; Han, X.; Lai, A.L.; Bushweller, J.H.; Cafiso, D.S.; Tamm, L.K. *J. Virol.* **2005**, *79*, 12065-12076.

87. Lai, A.L.; Park, H.; White, J.M.; Tamm, L.K. *J. Biol. Chem.* **2006**, *281*, 5760-5770.

88. Lai, A.L.; Tamm, L.K. *J. Biol. Chem.* **2007**, *282*, 23946-23956.

89. Bodner, M.L.; Gabrys, C.M.; Struppe, J.O.; Weliky, D.P. *J. Chem. Phys.* **2008**, *128*, 052319.

90. Freed, E.O.; Martin, M.A. *J. Biol. Chem.* **1995**, *270*, 23883-23886.

91. Wilkinson, D. *Curr. Biol.* **1996**, *6*, 1051-1053.

92. Tan, K.; Liu, J.; Wang, J.; Shen, S.; Lu, M. *Proc. Natl. Acad. Sci. U.S.A.* **1997**, *94*, 12303-12308.

93. Caffrey, M.; Cai, M.; Kaufman, J.; Stahl, S.J.; Wingfield, P.T.; Covell, D.G.; Gronenborn, A.M.; Clore, G.M. *EMBO J.* **1998**, *17*, 4572-4584.

94. Chang, D.K.; Cheng, S.F.; Chien, W.J. *J. Virol.* **1997**, *71*, 6593-6602.

95. Morris, K.F.; Gao, X.; Wong, T.C. *Biochim. Biophys. Acta.* **2004**, *1667*, 67-81.

96. Li, Y.; Tamm, L.K. *Biophys. J.* **2007**, *93*, 876-885.

97. Jaroniec, C.P.; Kaufman, J.D.; Stahl, S.J.; Viard, M.; Blumenthal, R.; Wingfield, P.T.; Bax, A. *Biochemistry* **2004**, *44*, 16167-16180.

98. Rafalski, M.; Lear, J.D.; DeGrado, W.F. *Biochemistry* **1990**, *29*, 7917-7922.

99. Nieva, J.L.; Nir, S.; Muga, A.; Goni, F.M.; Wilschut, J. *Biochemistry* **1994**, *33*, 3201-3209.

100. Jaroniec, C.P.; Kaufman, J.D.; Stahl, S.J.; Viard, M.; Blumenthal, R.; Wingfield, P.T.; Bax, A. *Biochemistry* **2005**, *44*, 16167-16180.

101. Aloia, R.C.; Tian, H.; Jensen, F.C. *Proc. Natl. Acad. Sci. U.S.A.* **1993**, *90*, 5181-5185.

102. Wasniewski, C.M.; Parkanzky, P.D.; Bodner, M.L.; Weliky, D.P. *Chem. Phys. Lipids* **2004**, *132*, 89-100.

103. Brügger, B.; Glass, B.; Haberkant, P.; Leibrecht, I.; Wieland, F.T.; Kräusslich, H.G. *Proc. Natl. Acad. Sci. U.S.A.* **2006**, *103*, 2641-2646.

104. Yang, R.; Yang, J.; Weliky, D.P. *Biochemistry* **2003**, *42*, 3537-3535.

105. Yang, R., Prorok, M., Castellino, F. J., and Weliky, D. P. *J. Am. Chem. Soc.* **2004**, *126*, 14722-14723.

106. Rey, F.A.; Heinz, F.X.; Mandl, C.; Kunz, C.; C., H.S. *Nature* **1995**, *375*, 291-298.

107. Bressanelli, S.; Stiasny, K.; Allison, S.L.; Stura, E.A.; Duquerroy, S.; Lescar, J.; Heinz, F.X.; Rey, F.A. *EMBO J.* **2004**, *23*, 728-738.

108. Allison, S.L.; Schalich, J.; Stiasny, K.; Mandl, C.W.; Heinz, F.X. *J. Virol.* **2001**, *75*, 4268-4275.

109. Guirakhoo, F.; Heinz, F.X.; Mandl, C.W.; Holzmann, H.; Kunz, C. *J. Gen. Virol.* **1991**, *72*, 1323-1329.

110. Corver, J.; Ortiz, A.; Allison, S.L.; Schalich, J.; Heinz, F.X.; Wilschut, J. *Virology* **2000**, *269*, 37-46.

111. Stiasny, K., Koessl, C., and Heinz, F. X. *J. Virol.* **2003**, *77*, 7856-7862.

112. Allison, S.L.; Schalich, J.; Stiasny, K.; Mandl, C.W.; Kunz, C.; Heinz, F.X. *J. Virol* **1995**, *69*, 695-700.

113. Stiasny, K.; Allison, S.L.; Mandl, C.W.; Heinz, F.X. *J. Virol.* **2001**, *75*,

7392-7398.

114. Stiasny, K.; Allison, S.L.; Schalich, J.; Heinz, F.X. *J. Virol.* **2002**, *76*, 3784-3790.

115. Stiasny, K.; Kössl, C.; Lepault, J.; Rey, F.A.; Heinz, F.X. *PLoS Pathog.* **2007**, *3*, e20.

116. Chernomordik, L.V.; Kozlov, M.M. *Cell* **2005**, *123*, 375-382.

117. Lescar, J.; Roussel, A.; Wien, M.W.; Navaza, J.; Fuller, S.D.; Wengler, G.; Rey, F.A. *Cell* **2001**, *105*, 137-48.

118. Modis, Y.; Ogata, S.; Clements, D.; Harrison, S.D. *Proc. Natl Acad. Sci. U.S.A.* **2003**, *100*, 6986-6991.

119. Modis, Y.; Ogata, S.; Clements, D.; Harrison, S.C. *J. Virol.* **2005**, *79*, 1223-1231.

120. Zhang, Y.; Zhang, W.; Ogata, S.; Clements, D.; Strauss, J.H.; Baker, T.S.; Kuhn, R.J.; Rossmann, M.G. *Structure* **2004**, *12*, 1607-1618.

121. Roussel, A.; Lescar, J.; Vaney, M.C.; Wengler, G.; Wengler, G.; Rey, F.A. *Structure* **2006**, *14*, 75-86.

122. Gibbons, D.L.; Vaney, M.C.; Roussel, A.; Vigouroux, A.; Reilly, B.; Lepault, J.; Kielian, M.; Rey, F.A. *Nature* **2004**, *427*, 320-325.

123. Klimjack, M.R.; Jeffrey, S.; Kielian, M. *J. Virol.* **1994**, *68*, 6940-4946.

124. Stiasny, K.; Bressanelli, S.; Lepault, J.; Rey, F.A.; Heinz, F.X. *J. Virol.* **2004**, *78*, 3178-3183.

125. Gibbons, D.L.; Reilly, B.; Ahn, A.; Vaney, M.C.; Vigouroux, A.; Rey, F.A.; Kielian, M. *J. Virol.* **2004**, *78*, 3514-3523.

126. Zhang, W.; Mukhopadhyay, S.; Pletnev, S.V.; Baker, T.S.; Kuhn, R.J.; Rossmann, M.G. *J. Virol.* **2002**, *76*, 11645-11658.

127. Mukhopadhyay, S.; Zhang, W.; Gabler, S.; Chipman, P.R.; Strauss, E.G.; Strauss, J.H.; Baker, T.S.; Kuhn, R.J.; Rossmann, M.G. *Structure* **2006**, *14*, 63-73.

128. Heinz, F.X.; Allison, S.L. *Adv. Virus Res.* **2000**, *55*, 231-269.

129. Phalen, T.; Kielian, M. *J. Cell Biol.* **1991**, *112*, 615-623.

130. Wahlberg, J.M.; Bron, R.; Wilschut, J.; Garoff, H. *J. Virol.* **1992**, *66*, 7309-7318.

131. White, J.; Helenius, A. *Proc. Natl. Acad. Sci. U.S.A.* **1980**, *77*, 3273-3277.

132. Kielian, M.C.; Helenius, A. *J. Virol.* **1984**, *52*, 281-283.

133. Corver, J.; Moesby, L.; Erukulla, R.K.; Reddy, K.C.; Bittman, R.; Wilschut, J. *J. Virol.* **1995**, *69*, 3220-3223.

134. Smit, J.M.; Bittman, R.; Wilschut, J. *J. Virol.* **1999**, *73*, 8476-8484.

135. Earp, L.J.; Delos, S.E.; Park, H.E.; White, J.M. *Curr. Top Microbiol. Immunol.* **2005**, *285*, 25-66.

136. Carr, C.M.; Chaudhry, C.; Kim, P.S. *Proc. Natl. Acad. Sci. U.S.A.* **1997**, *94*, 14306-14313.

137. Paterson, R.G.; Russell, C.J.; Lamb, R.A. *Virology* **2000**, *270*, 17-30.

138. Wharton, S.A.; Skehel, J.J.; Wiley, D.C. *Virology* **2000**, *271*, 71-78.

139. Wallin, M.; Ekström, M.; Garoff, H. *J. Virol.* **2005**, *79*, 1678-1685.

140. Gibbons, D.L.; Ahn, A.; Chatterjee, P.K.; Kielian, M. *J. Virol.* **2000**, *74*, 7772-7780.

141. Huang, Q.; Opitz, R.; Knapp, E.W.; Herrmann, A. *Biophys. J.* **2002**, *82*, 1050-1058.

142. Crawford, R.L. *Lignin biodegradation and transformation*, John Wiley and Sons: New York, 1981.

143. Updegraff, D.M. *Anal. Biochem.* **1969**, *32*, 420-424.

144. Tarchevsky, I.A.; Marchenko, G.N. *Cellulose: Biosynthesis and structure*, Springer-Verlag: Berlin Heidelberg, 1991.

145. Fetzer, W.R.; Grosby, E.K.; Endel, C.E.; Kierst, L.C. *Industr. and Eng. Chem.* **1953**, *45*, 1075.

146. Klemm, D.; Heublein, B.; Fink, H.P.; Bohn, A. *Angew. Chem. Int. Ed. Engl.* **2005**, *44*, 3358-3393.

147. Eliel, E. *Stereochemistry of carbon compounds*, Mir: Moscow, 1965.

148. Segal, L. *Chemical reactions of polymers*, Mir: Moscow, 1967.

149. Panov, V.P.; Zhbankov, R.G. *Conformations of carbohydrates* Nauka i Tekhnika: Minsk, 1975.

150. Zhbankov, R.G.; Marupov, R.M.; Ivanova, N.Y.; Shishko, A.M. *Spectroskopy of cotton*, Nauka: Moscow, 1976.

151. Zhbankov, R.G. *Infrared spectra of cellulose and its derivatives*, Nauka i Tekhnika: Minsk, 1964.

152. Barker, S.A.; Bourne, E.G.; Staceg, M.; Whiffen, D.N. *J. Chem. Soc.* **1954**, *6*, 171.

153. Hardy, B.J.; Sarko, A. *Polymer* **1996**, *37*, 1833-1839.

154. Atalla, R.H.; Vanderhart, D.L. *Science* **1984**, *223*, 283-285.

155. Atalla, R.H. In *Cellulose - Patterns of aggregation in native celluloses: implication of recent sepctrscopic studies*. Kenndeys, J.F.; Phillips, G.O.; Williams, P.A.; Ellis Horwood: Chichester, 1989; pp 61-73.

156. Davidson, T.C.; Newman, R.H.; Ryan, M.J. *Carbohydr. Res.* **2004**, *339*, 2889-2893.

157. Jarvis, M. *Nature* **2003**, *426*, 611-612.

158. Nishiyama, Y.; Langan, P.; Chanzy, H. *J. Am. Chem. Soc.* **2002**, *124*, 9074-9082.

159. Nishiyama, Y.; Sugiyama, J.; Chanzy, H.; Langan, P. *J. Am. Chem. Soc.* **2003**, *125*, 14300-14306.

160. Jarvis, M.C. *Carbohydr. Res.* **2000**, *325*, 150-154.

161. Kono, H.; Numata, Y. *Polymer* **2004**, *45*, 4541-4547.

162. Wada, M.; Chanzy, H.; Nishiyama, Y.; Langan, P. *Macromolecules* **2004**, *37*, 8548 -8555.

163. Levy-Mintz, P.; Kielian, M. *J. Virol.* **1991**, *65*, 4292-4300.

164. Ahn, A.; Gibbons, D.L.; Kielian, M. *J. Virol* **2002**, *76*, 3267-3275.

165. Goto, N.K.; Kay, L.E. *Curr. Opin. Struct. Biol.* **2000**, *10*, 585-592.

166. Hong, M. *J. Magn. Reson.* **1999**, *139*, 389-401.

167. Hong, M.; Jakes, K. *J. Biomol. NMR.* **1999**, *14*, 71-74.

168. Roehrig, J.T.; Hunt, A.R.; Johnson, A.J.; Hawkes, R.A. *Virology.* **1989**, *171*, 49-60.

169. Mandl, C.W.; Holzmann, H.; Kunz, C.; Heinz, F.X. *Virology* **1993**, *194*, 173-184.

170. Nitayaphan, S.; Grant, J.A.; Chang, G.J.; Trent, D.W. *Virology* **1990**, *177*, 541-552.

171. Blok, J.; Samuel, S.; Gibbs, A.J.; Vitarana, U.T. *Arch. Virol.* **1989**, *105*, 39-53.

172. Carpino, L.A. *J. Am. Chem. Soc.* **1957**, *79*, 4686.

173. Roepstorrf, P.; Fohlmann, J. *Biomed. Mass Spectrom.* **1984**, *11*, 601.

174. Johnson, R.S.; Biemann, K. *Biomed. Environ. Mass Spectrom.* **1989**, *18*, 945.

175. Sreerama, N.; Woody, R.W. *Anal. Biochem.* **2000**, *287*, 252-260.

176. Smaby, J.M.; Momsen, M.M.; Brockman, H.L.; Brown, R.E. *Biophys. J.* **1997**, *73*, 1492-1505.

177. Bloom, M.; Evans, E.; Mouritsen, O.G. *Q. Rev. Biophys.* **1991**, *24*, 293-397.

178. Li, X.M.; Momsen, M.M.; Smaby, J.M.; Brockman, H.L.; Brown, R.E. *Biochemistry* **2001**, *40*, 5954-5963.

179. Silvius, J.R. *Biochim. Biophys. Acta.* **2003**, *1610*, 174-183.

180. Binder, W.H.; Barragan, V.; Menger, F.M. *Angew. Chem. Int. Ed. Engl.* **2003**, *42*, 5802-5827.

181. Simons, K.; Vaz, W.L. *Annu. Rev. Biophys. Biomol. Struct.* **2004**, *33*, 269-295.

182. Yang, J.; Parkanzky, P.D.; Bodner, M.L.; Duskin, C.A.; Weliky, D.P. *J. Magn. Reson.* **2002**, *159*, 101-110.

183. Stryer, L.; Haugland, R.P. *Proc. Natl. Acad. Sci. U.S.A.* **1967**, *58*, 719-726.

184. Kawski, A. *Photochem. Photobiol.* **1983**, *38*, 487-487.

185. dos Remedios, C.G.; Miki, M.; Barden, J.A. *J. Muscle Res. Cell Motil.* **1987**, *8*, 97-117.

186. Fairclough, R.H.; Cantor, C.R. *Methods Enzymol.* **1978**, *48*, 347-379.

187. Wu, P.; Brand, L. *Anal. Biochem.* **1994**, *218*, 11-13.

188. Selvin, P.R. *Methods Enzymol.* **1995**, *246*, 300-334.

189. Boyde, A.; Wolfe, L.A.; Maly, M.; Jones, S.J. *Scanning* **1995**, *17*, 72-85.

190. dos Remedios, C.G.; Moens, P.D. *J. Struct. Biol.* **1995**, *1995*, 175-185.

191. Berney, C.; Danuser, G. *Biophys. J.* **2003**, *84*, 3992-4010.

192. Struck, D.K.; Hoekstra, D.; Pagano, R.E. *Biochemistry* **1981**, *20*, 4093-4099.

193. Taken from http://www-cellbio.med.unc.edu/images/fretspectra.jpg (accessed 14/05/2009)

194. Uster, P.S. *Methods Enzymol.* **1993**, *221*, 239-246.

195. Volkova, T.D.; Vorovitch, M.F.; Ivanov, V.T.; Timofeev, A.V.; Volpina, O.M. *Arch. Virol.* **1999**, *144*, 1035-1039.

196. Roehrig, J.T.; Johnson, A.J.; Hunt, A.R.; Bolin, R.A.; Chu, M.C. *Virology* **1990**, *177*, 668-675.

197. Trivedi, V.D.; Yu, C.; Veeramuthu, B.; Francis, S.; Chang, D.K. *Chem. Phys.*

Lipids **2000**, *107*, 99-106.

198. Lentz, B.R.; Carpenter, T.J.; Alford, D.R. *Biochemistry* **1987**, *26*, 5389-5397.

199. Meyuhas, D.; Nir, S.; Lichtenberg, D. *Biophys. J.* **1996**, *71*, 2602-2612.

200. Parsegian, V.A.; Rand, P.R. In - *Membrane Fusion.* Wilschut, J.; Hoekstra, D.; Marcel Dekker: New York, 1991; pp 65.

201. Gollins, S.W.; Porterfield, J.S. *J. Gen. Virol.* **1986**, *67*, 157-166.

202. Bron, R.; Wahlberg, J.M.; Garoff, H.; Wilschut, J. *EMBO J.* **1993**, *12*, 693-701.

203. Stegmann, T.; Hoekstra, D.; Scherphof, G.; Wilschut, J. *J. Biol. Chem.* **1986**, *261*, 10966-10969.

204. Stegmann, T.; Booy, F.P.; Wilschut, J. *J. Biol. Chem.* **1987**, *262*, 17744-17749.

205. Stegmann, T.; White, J.M.; Helenius, A. *EMBO J.* **1990**, *9*, 4231-4241.

206. Heinz, F.X.; Stiasny, K.; Puschner, A.G.; Holzmann, H.; Allison, S.L.; Mandl, C.W.; Kunz, C. *Virology* **1994**, *198*, 109-117.

207. Bewley, T.A.; Li, C.H. *Int. J. Protein Res.* **1969**, *1*, 117-124.

208. Thornton, J.M. *J. Mol. Biol.* **1981**, *151*, 261-287.

209. Abkevich, V.I.; Shakhnovich, E.I. *J. Mol. Biol.* **2000**, *300*, 975-985.

210. White, J.M.; Delos, S.E.; Brecher, M.; Schornberg, K. *Crit. Rev. Biochem. Mol. Biol.* **2008**, *43*, 189-219.

211. Ellman, G.L. *Arch. Biochem. Biophys.* **1958**, *74*, 443-450.

212. Riddles, P.W.; Blakeley, R.L.; Zerner, B. *Methods Enzymol.* **1983**, *91*, 49-60.

213. Black, S.D.; Coon, M.J. *Biochem. Biophys. Res. Commun.* **1985**, *128*, 82-89.

214. Flory, P. *Principles of Polymer Chemistry.*, Cornell Univ. Press: Ithaca, 1953.

215. Pace, C.N.; Grimsley, G.R.; Thomson, J.A.; Barnett, B.J. *J. Biol. Chem.* **1988**,

263, 11820-11825.

216. Nieva, J.L.; Bron, R.; Corver, J.; Wilschut, J. *EMBO J.* **1994**, *13*, 2797-2804.

217. Moesby, L.; Corver, J.; Erukulla, R.K.; Bittman, R.; Wilschut, J. *Biochemistry* **1995**, *34*, 10319-10324.

218. Calculated by *PEPscreen Calculator* from http://www.sigmaaldrich.com/life-science/custom-oligos/custom-peptides/learning-center/pepscreen-calculator/pepscreen-calculator-inst.html

219. Aletras, A.; Barlos, K.; Gatos, D.; Koutsogianni, S.; Mamos, P. *Int. J. Pept. Protein Res.* **1995**, *45*, 488-496.

220. Qiang, W.; Weliky, D.P. *Biochemistry* **2009**, *48*, 289-301.

221. Kolber, M.A.; Haynes, D.H. *J. Membr. Biol.* **1979**, *48*, 95-114.

222. Pryor, C.; Bridge, M.; Loew, L.M. *Biochemistry* **1985**, *24*, 2203-2209.

223. Epand, R.M.; Bain, A.D.; Sayer, B.G.; Bach, D.; Wachtel, E. *Biophys. J.* **2002**, *83*, 2053-2063.

224. Bodner, M.L.; Gabrys, C.M.; Parkanzky, P.D.; Yang, J.; Duskin, C.A.; Weliky, D.P. *Magn. Reson. Chem.* **2004**, *24*, 187-194.

225. Hediger, S.; Meier, B.H.; Ernst, R.R. *Chem. Phys. Lett.* **1995**, *240*, 449-456.

226. Hediger, S.; Meier, B.H.; Kurur, N.D.; Bodenhausen, G.; Ernst, R.R. *Chemical Physics Letters* **1994**, *223*, 283-288.

227. Metz, G.; Wu, X.L.; Smith, S.O. *Journal of Magnetic Resonance Series A* **1994**, *110*, 219-227.

228. Earl, W.L.; Vanderhart, D.L. *Journal of Magnetic Resonance* **1982**, *48*, 35-54.

229. Hamad, W. *Can. J. Chem. Eng.* **1996**, *84*, 513-519.

230. Fleming, K.; Gray, D.G.; Matthews, S. *Chem. Eur. J.* **2001**, *7*, 1831-1835.

231. Fraden, S.; Maret, G.; Caspar, D.L.D.; Meyer, R.B. *Phy. Revi. Letters* **1989**, *63*,

2068-2071.

232. Folda, T.; Hoffman, H.; Chanzy, H.; Smith, P. *Nature* **1988**, *333*, 55-56.

233. Buining, P.A.; Lekkerkerker, H.N.W. *Journal of Physical Chem.* **1993**, *97*, 11510-11516.

234. Clore, G.M.; Starich, M.R.; Gronenborn, A.M. *J. Am. Chem. Soc.* **1998**, *120*, 10571-10572.

235. Dong, X.M.; Kimura, T.; Revol, J.F.; Gray, D.G. *Langmuir* **1996**, *12*, 2076-2082.

236. Zhao, H.; Holladay, J.E.; Kwak, J.H.; Zhang, Z.C. *J. Phys. Chem. B* **2007**, *111*, 5295-5300.

237. Ward, K. *Textile Research Journal* **1950**, *20*, 363-372.

238. Dong, X.M.; Revol, J.F.; Gray, D.G. *Cellulose* **1998**, *5*, 19-32.

239. Rodger, A.; Norden, B. *Circular Dichroism and Linear Dichroism*, Oxford University Press: Oxford, 1997.

240. Hatano, M. In *Induced Circular Dichroism in Biopolymer-Dye Systems. - Induced circular dichroism in liquid crystalline phases.* Okamura, S.; Springer-Verlag: Berlin, 1986; pp 94-102.

241. Onsager, L. *Ann. N. Y. Acad. Sci.* **1949**, *51*, 627.

242. Stroobants, A.; Lekkerkerker, H.N.W.; Odijk, T. *Macromolecules* **1986**, *19*, 2232.

243. Sato, T.; Teramoto, A. *Physca. A* **1991**, *176*, 72-86.

244. Semenov, A.N.; Kokhlov, A.R. *Sov. Phys. Usp.* **1988**, *31*, 988.

245. Lee, S.D. *J. Chem. Phys.* **1987**, *87*, 4972.

246. Saeva, F.D.; Sharpe, P.E.; Olin, G.R. *J. Am. Chem. Soc.* **1973**, *95*, 7656-7659.

247. Uematsu, Y.; Uematsu, I. *ACS Symposium Series*, Blumstein, A., **1978**, *74*, 136-156.

248. Kimura, H.; Hosino, M.; Nakano, H. *J. Phys. Soc. Jpn.* **1982**, *51*, 1584-1590.

249. Shimamoto, S.; Gray, D.G. *Cellulose* **1999**, *6*, 15-22.

250. Ritcay, A.M.; Gray, D.G. *Macromolecules* **1988**, *21*, 1251-1255.

251. Guo, J.X.; Gray, D.G. *Macromolecules* **1989**, *22*, 2086-2090.

252. Kimura, T. *Polym. J.* **2003**, *35*, 823.

253. Sugiyama, J.; Chanzy, H.; Maret, G. *Macromolecules* **1992**, *25*,

254. Revol, J.F.; Godbout, L.; Dong, X.M.; Gray, D.G.; Chanzy, H.; Maret, G. *Liq. Cryst.* **1994**, *16*, 127.

255. Dong, X.M.; Gray, D.G. *Langmuir* **1997**, *13*, 3029.

256. Saeva, F.D.; Wysocki, J.J. *J. Am. Chem. Soc.* **1971**, *93*, 5928-5929.

257. Holzwarth, G.; Holzwarth, N.A.W. *J. Optical Soc. America* **1973**, *63*, 324-331.

258. Edgar, C.D.; Gray, D.G. *Cellulose* **2001**, *8*, 5-12.

259. Fink, H.P.; Fanter, D.; Phillip, B. *Acta. Polym.* **1985**, *36*, 1-8.

260. Polizzi, S.; Fagherazzi, G.; Benedetti, A.; Battagliarin, M.; Asano, T. *J. Appl. Crystallogr.* **1990**, *23*, 359-365.

261. Horii, F.; Hirai, A.; Kitamaru, R. *ACS Symp. Ser.* **1987**, *340*, 119-134.

262. Newman, R.H.; Hemmingson, J.A. *Holzforschung* **1990**, *44*, 351-355.

263. Kunze, J.; Fink, H.P. *Das Papier* **1999**, *12*, 753-764.

264. Vanderhart, D.L.; Atalla, R.H. *The structures of Celluloses. ACS Symp. Ser. 340.*, Atalla, R.H., **1987**, 88-118.

265. Hesse, S.; Ja¨ger, C. *Cellulose* **2005**, *12*, 5-14.

266. Erata, T.; Shikono, T.; Yunoki, S.; Takai, M. *Cellulose Commun.* **1997**, *4*, 128-131.

267. Kono, H.; Yunoki, S.; Shikono, T.; Fujiwara, M.; Erata, T.; Erata, M. *J. Am. Chem. Soc.* **2002**, *124*, 7506-7511.

268. Lesage, A.; Bardet, M.; Emsley, L. *J. Am. Chem. Soc.* **1999**, *121*, 10987-10993.

269. Massiot, D.; Fayon, F.; Capron, M.; King, I.; Le Calve´, S.; Alonso, B.; Durand, J.O.; Bujoli, B.; Gan, Z.; Hoatson, G. *Magnet. Res. Chem.* **2002**, *40*, 70-76.

270. Kim, J.; Chen, Y.; Kang, K.S.; Park, Y.B.; Schwartz, M. *J. Appl. Phys.* **2008**, *104*, 096104.

271. Opella, S.J.; Marassi, F.M.; Gesell, J.J.; Valente, A.P.; Kim, Y.; Oblatt-Montal, M.; Montal, M. *Nat. Struct. Biol.* **1999**, *6*, 374-379.

272. Park, S.H.; Mrse, A.A.; Nevzorov, A.A.; Mesleh, M.F.; Oblatt-Montal, M.; Montal, M.; Opella, S.J. *J. Mol. Biol.* **2003**, *333*, 409-424.

273. Marassi, F.M.; Opella, S.J. *Protein Sci.* **2003**, *12*, 403-411.

274. Zeri, A.C.; Mesleh, M.F.; Nevzorov, A.A.; Opella, S.J. *Proc. Natl. Acad. Sci. U.S.A.* **2003**, *100*, 6458-6463.

275. Gullion, T.; Schaefer, J. *J. Magn. Reson.* **1989**, *81*, 196-200.

276. Schmidt-Rohr, K.; deAzevedo, E.R.; Bonagamba, T.J. In *Encyclopedia of NMR - Centerband-only detection of exchang (CODEX): efficient NMR analysis of slow motions in solids*. Grant, D.M.; Harris, R.K.; John Wiley & Sons: Chichester, UK, 2002; pp

277. deAzevedo, E.R.; Bonagamba, T.J.; Hu, W.; Schmidt-Rohr, K. *J. Am. Chem. Soc.* **1999**, *121*, 8411.

278. deAzevedo, E.R.; Bonagamba, T.J.; Hu, W.; Schmidt-Rohr, K. *J. Chem. Phys.* **2000**, *112*, 8988.

279. Ruiz, M.M.; Cavaille, J.Y.; Dufresne, A.; Gerard, J.F.; Graillat, C. *Compos. Interfaces* **2000**, *7*, 117-131.

280. Samir, M.; Alloin, F.; Dufresne, A. *Biomacromolecules* **2005**, *6*, 612-626.

281. Helbert, W.; Cavaille, J.Y.; Dufresne, A. *Polym. Compos.* **1996**, *17*, 604-611.

282. Grunert, M.; Winter, W.T. *Polym. Mater. Sci. Eng.* **2000**, *82*, 232.

283. Winter, W.T.; Bhattacharya, D. *225th ACS National Meeting* New Orleans, March 23-27, 2003

284. Roman, M.; Winter, W.T. *ACS Symposium Series 938*, **2006**, 99-113.